

## On Stability Enhancement in AC/DC Power Systems through Multi-terminal HVDC Controllers

Kotb, O.

**DOI**

[10.4233/uuid:cb24d1b1-0b9f-4966-8cf4-8a9a5ee70146](https://doi.org/10.4233/uuid:cb24d1b1-0b9f-4966-8cf4-8a9a5ee70146)

**Publication date**

2018

**Document Version**

Final published version

**Citation (APA)**

Kotb, O. (2018). *On Stability Enhancement in AC/DC Power Systems through Multi-terminal HVDC Controllers*. [Dissertation (TU Delft), Delft University of Technology, Universidad Pontificia Comillas, KTH Royal Institute of Technology]. <https://doi.org/10.4233/uuid:cb24d1b1-0b9f-4966-8cf4-8a9a5ee70146>

**Important note**

To cite this publication, please use the final published version (if applicable). Please check the document version above.

**Copyright**

Other than for strictly personal use, it is not permitted to download, forward or distribute the text or part of it, without the consent of the author(s) and/or copyright holder(s), unless the work is under an open content license such as Creative Commons.

**Takedown policy**

Please contact us and provide details if you believe this document breaches copyrights. We will remove access to the work immediately and investigate your claim.

DOCTORAL THESIS

STOCKHOLM, SWEDEN 2018

# On Stability Enhancement in AC/DC Power Systems through Multi-terminal HVDC Controllers

Omar Kotb



# **On Stability Enhancement in AC/DC Power Systems through Multi-terminal HVDC Controllers**

Omar Kotb

**Thesis supervisors:**

Prof. Mehrdad Ghandhari	KTH Royal Institute of Technology
Dr. Robert Eriksson	Svenska Kraftnät (Swedish National Grid)

**Members of the Examination Committee:**

Prof. Pablo García González	Comillas Pontifical University, Spain
Prof. Lina Bertling Tjernberg	KTH Royal Institute of Technology, Sweden
Associate Prof. Marjan Popov	Technische Universiteit Delft, the Netherlands
Prof. Torbjörn Thiringer	Chalmers University of Technology, Sweden
Dr. Jonas Persson	Vattenfall, Sweden

**TRITA-EECS-AVL-2018:25**

**ISBN 978-91-7729-726-0**

© Omar Kotb, 2018

Printed by: US-AB

# On Stability Enhancement in AC/DC Power Systems through Multi-terminal HVDC Controllers

Dissertation

for the purpose of obtaining the degree of doctor  
at Delft University of Technology  
by the authority of the Rector Magnificus prof.dr.ir. T.H.J.J. van der Hagen  
Chair of the Board for Doctorates  
to be defended publicly on  
Tuesday 12 June 2018 at 10:00 o'clock

by

Omar KOTB  
Electrical Power Engineer

M.A.Sc in Electrical and Computer Engineering  
University of Ontario Institute of Technology (UOIT), Canada  
born in Cairo, Egypt

This dissertation has been approved by the promotor.

Composition of the doctoral committee:

Chairman	KTH Royal Institute of Technology, Sweden
Prof. dr. ir. P. M. Herder	Technische Universiteit Delft, the Netherlands, promotor

Independent members:

Prof. Pablo García González	Comillas Pontifical University, Spain
Prof. Lina Bertling Tjernberg	KTH Royal Institute of Technology, Sweden
Associate Prof. Marjan Popov	Technische Universiteit Delft, the Netherlands
Prof. Torbjörn Thiringer	Chalmers University of Technology, Sweden
Dr. Jonas Persson	Vattenfall, Sweden
Dr. Bertil Berggren	ABB Corporate Research, Sweden, reserve member

The doctoral research has been carried out in the context of an agreement on joint doctoral supervision between Comillas Pontifical University, Madrid, Spain, KTH Royal Institute of Technology, Stockholm, Sweden and Delft University of Technology, the Netherlands.

Keywords: AC/DC power system, hybrid MTDC, multi-terminal HVDC, small signal stability, VSC-MTDC

ISBN 978-91-7729-726-0

Copyright © 2018 O. Kotb. All rights reserved. No part of the material protected by this copyright notice may be reproduced or utilized in any form or by any means, electronic or mechanical, including photocopying, recording or by any information storage and retrieval system, without written permission from the author.

Printed by: US-AB

## SETS Joint Doctorate

The Erasmus Mundus Joint Doctorate in *Sustainable Energy Technologies and Strategies*, SETS Joint Doctorate, is an international programme run by six institutions in cooperation:

- Comillas Pontifical University, Madrid, Spain
- Delft University of Technology, Delft, the Netherlands
- KTH Royal Institute of Technology, Stockholm, Sweden
- Florence School of Regulation, Florence, Italy
- Johns Hopkins University, Baltimore, USA
- University Paris-Sud 11, Paris, France

The Doctoral Degrees issued upon completion of the programme are issued by Comillas Pontifical University, Delft University of Technology, and KTH Royal Institute of Technology.

The Degree Certificates are giving reference to the joint programme. The doctoral candidates are jointly supervised, and must pass a joint examination procedure set up by the three institutions issuing the degrees.

This thesis is a part of the examination for the doctoral degree. The invested degrees are official in Spain, the Netherlands and Sweden respectively.

SETS Joint Doctorate was awarded the Erasmus Mundus **excellence label** by the European Commission in year 2010, and the European Commission's **Education, Audiovisual and Culture Executive Agency**, EACEA, has supported the funding of this programme.

The EACEA is not to be held responsible for contents of the thesis.



## **Abstract in English Language**

Author: Omar Kotb

Department of Electric Power and Energy Systems (EPE)

Affiliation: KTH Royal Institute of Technology

Title: On Stability Enhancement of AC/DC Power Systems through Multi-terminal HVDC Controllers

Language: English

Keywords: AC/DC power system, hybrid MTDC, multi-terminal HVDC, small signal stability, VSC-MTDC

Due to the increasing share of renewable energy sources in modern power systems and electricity market deregulation, heavy inter-regional and cross-border power flows are becoming a commonplace in system operation. Moreover, large-scale integration of renewable energy sources is expected to pace up, therefore new solutions have to be developed to integrate these intermittent sources, which are also characterized by being distributed over large geographical areas, such as offshore wind farms. Multi-Terminal High Voltage Direct Current (MTDC) networks are expected to form a solution for the integration of renewable energy sources to the existing interconnected AC grid. The type of converters used in the MTDC networks is however a subject of debate, as both Line Commutated Converters (LCCs) and Voltage Source Converters (VSCs) can be used. Moreover, the coordinated control of the MTDC networks with the AC system poses a challenge to the system operators, as it requires the consideration of both AC and DC system dynamics.

In response to these challenges, this thesis aims to discuss the following aspects of the MTDC networks: control of a hybrid MTDC with both LCCs and VSCs, as well as the utilization of an embedded VSC-MTDC for stability enhancement. The thesis also investigates the supply of passive AC systems using a hybrid MTDC network.

In the investigation of an AC/DC power system with a hybrid MTDC network, first, the combined AC/DC system is modeled. Next, a Small Signal Stability Analysis (SSSA) of the system is conducted, based on which the Power Oscillation Damping (POD) controllers were designed to enhance stability in the connected AC systems.

In the utilization of an embedded VSC-MTDC network for stability enhancement in the AC/DC system, the operating point adjustment strategy is investigated, which is implemented through the adjustment of setpoints for the active and reactive power controllers in the network converters. Finally, the design and placement of

a Multi-Input Single Output (MISO) controller is investigated, where the control strategy is based on Modal Linear Quadratic Gaussian (MLQG) control using Wide Area Measurement Systems (WAMS) signals.

## Sammanfattning (Summary in Swedish)

Författare: Omar Kotb

Anslutning: Kungliga Tekniska Högskolan

Titel: Styrning av HVDC-nät med flera terminaler för att förbättra stabiliteten i kombinerade AC och DC System.

Språk: Engelska

Nyckelord: AC/DC elkraftsystem, hybrid MTDC, fler-terminal HVDC, små signalstabilitet, VSC-MTDC

På grund av den ökande andelen förnybara energikällor i moderna elektriska energisystem och avregleringen av elmarknaden blir stora effektflöden via vissa snitt i elsystemet en vanlig driftsituation. Dessutom förväntas storskalig integrering av förnybara energikällor att öka, varför nya lösningar måste utvecklas för att integrera dessa intermittenta energi källor som distribueras över stora geografiska områden. Multiterminal Högspänd Likström (MTDC) förväntas vara en lösning för integration av förnybara energikällor till det nuvarande sammankopplade elnätssystemet. Den typ av omriktare som används i MTDC systemet är emellertid föremål för diskussion, eftersom både strömstyva omriktare (LCC) och spänningstyva omriktare (VSC) kan användas. Dessutom innebär den samordnade kontrollen av MTDC systemet med växelström systemet en utmaning för systemoperatörerna, eftersom det kräver att beakta dynamiska förlopp i både AC- och MTDC system.

Som svar på dessa utmaningar syftar denna avhandling att diskutera följande aspekter av MTDC system: kontroll av ett hybrid MTDC system med både LCC och VSC omriktare, samt utnyttjandet av en inbyggd VSC-MTDC system för stabilitetsförbättring. Avhandlingen undersöker också elförsörjningen av ett passivt AC system (med noll svängmassa) med hjälp av ett hybrid MTDC-nätverk.

Vid undersökning av ett kombinerat AC- och hybrid MTDC system behövs först en matematisk modell baserad på vilken en småsignal analys genomförs. Denna analys är grunden till utformandet av styralgoritmerna med ett hybrid MTDC-nätverk, först, behöver det kombinerade AC / DC-systemet modelleras. Därefter genomförs en små signal studie för systemet vilken ligger till grund för utformandet av styralgoritmerna för att förbättra effektpendlingsdämpning i det anslutna AC systemen.

Vid användning av ett inbyggt VSC-MTDC system för stabilitetsförbättring undersöks driftspunktsstrategin, vilken genomförs genom justering av börvärden för de aktiva och reaktiva effektregulatorerna i omriktarna. Slutligen undersöks designen och placeringen av en MISO-regulator (Multi-Input Single Output), där

iv

kontrollstrategin är baserad på den så kallas "Modal Linear Quadratic Gaussian (MLQG)" med WAMS-signaler (Wide Area Measurement Systems).

## Abstract in Dutch Language

Auteur: Omar Kotb

Instituut: KTH Royal Institute of Technology

Titel: On Stability Enhancement of AC/DC Power Systems through Multi-terminal HVDC Controllers

Taal: Engels

Trefwoorden: AC/DC power system, hybrid MTDC, multi-terminal HVDC, small signal stability, VSC-MTDC

Vanwege het toenemende aandeel van hernieuwbare energiebronnen in moderne energiesystemen en de deregulering van de elektriciteitsmarkt, worden zware interregionale en grensoverschrijdende stroomstromen een frequent voorkomend fenomeen in de functioneren van het systeem. Bovendien is het aannemelijk dat een grootschalige integratie van hernieuwbare energiebronnen zal plaatsvinden in de nabije toekomst, wat inhoudt dat er nieuwe oplossingen ontwikkeld moeten worden om deze intermitterende bronnen te integreren. Deze hernieuwbare energiebronnen worden bovendien ook gekenmerkt door een grote geografische spreiding, zoals bijvoorbeeld het geval is voor offshore windparken. Naar verwachting zullen Multi-Terminal High Voltage Direct Current (MTDC)-netwerken een oplossing vormen voor de integratie van hernieuwbare energiebronnen binnen het bestaande AC-netwerk. Het type converter dat gebruikt wordt in de MTDC-netwerken blijft echter een onderwerp van discussie, omdat zowel Line Commutated Converter (LCCs) en Voltage Source Converters (VSCs) kunnen worden gebruikt. Bovendien vormt de gecombineerde besturing van de MTDC-netwerken met het huidige AC netwerk een uitdaging voor de systeembeheerders, omdat het zowel de AC als DC systeemdynamiek in overweging moet nemen.

Deze thesis probeert een antwoord te bieden voor al deze uitdagingen door de volgende aspecten van de MTDC-netwerken te bespreken: controle van een hybride MTDC met zowel LCCs als VSCs, evenals het gebruik van een ingebedde VSC-MTDC voor stabiliteitsverbetering. Deze thesis onderzoekt ook de stroomvoorziening in passieve AC-systemen met behulp van hybride MTDC-netwerken.

Bij het onderzoek van een AC/DC-voedingssysteem met een hybride MTDC-netwerk, wordt eerst het gecombineerde AC / DC-systeem gemodelleerd. Vervolgens wordt een Small Signal Stability Analysis (SSSA) van het systeem uitgevoerd, op basis waarvan de Power Oscillation Damping (POD)-controllers zijn ontworpen om de stabiliteit in de aangesloten AC-systemen te verbeteren.

Bij het gebruik van een ingebed VSC-MTDC-netwerk voor stabiliteitsverbe-

tering in het AC/DC-systeem, wordt de werkpuntaanpassingsstrategie onderzocht. Deze wordt geïmplementeerd door het aanpassen van setpoints voor de actieve en reactieve vermogensregelaars in de netwerkomzetters. Tenslotte wordt het ontwerp en de plaatsing van een Multi-Input Single Output (MISO)-controller onderzocht, waarbij de besturingsstrategie gebaseerd is op de Modal Linear Quadratic Gaussian (MLQG)-regeling met behulp van Wide Area Measurement Systems (WAMS)-signalen.

# Acknowledgment

This project was carried out within the Erasmus Mundus Joint Doctorate in Sustainable Energy Technologies and Strategies (SETS Joint Doctorate) and was funded mainly by the European Commission Erasmus Mundus Doctoral Fellowship and partially by KTH Royal Institute of Technology. I would like to express my gratitude towards all partner institutions within the program as well as the European Commission for their support.

I would like to thank Mehrdad Ghandhari, my supervisor, for providing me with the opportunity to work on this project and for his guidance through it. Special thanks to Robert Eriksson, my co-supervisor, for his continuous support, insightful feedback and discussions. I would like to thank Luis Rouco, my supervisor at the Institute of Research in Technology (IIT), for hosting me during my research stay at Comillas. I would also like to thank Lars Nordström, head of the Electric Power and Energy (EPE) department at KTH, for providing us with an open and friendly work environment at the department. I would also like to thank Vijay Sood, my former M.Sc supervisor at UOIT, for the fruitful cooperation and support that continues to this day. Also thanks to Rujiroj Leelaruji for his support on DIgSILENT. Special thanks to Sara Tamarit, SETS program coordinator at Comillas, for her continuous support on the administrative works throughout the program. My heartfelt love and appreciation goes to my friends at the PSOC research group: Dimitris, Taha, Marina, Harold, Shahab, Kaveh, and Danilo, you guys have kept me happy and inspired during this journey. Also thanks to all my friends at EPE and ETK: Ilias, Elena, Stefan, Lars, Elis, Ekaterina, Dina, Meng, Farhan, Viktor, Francisco, Mahir, Anna, Wei Li, Almas, Martin, Zhao, and Poria. I would also like to thank all colleagues and staff at the EPE department for the interesting discussions and fun moments that we shared together. Also thanks to my friends at IIT in Madrid: Ibtihal, Luis, Javier, William, Alvaro, and Adrian. Last but not least, I would like to express my love and gratitude towards my parents and my sister, Yosra, for their unconditional love that has constantly been a source of warmth and support throughout this journey.



# Contents

<b>Abstract in English Language</b>	<b>i</b>
<b>Abstract in Swedish Language</b>	<b>iii</b>
<b>Abstract in Dutch Language</b>	<b>v</b>
<b>Contents</b>	<b>ix</b>
<b>List of Figures</b>	<b>xiii</b>
<b>List of Tables</b>	<b>xv</b>
<b>1 Introduction</b>	<b>1</b>
1.1 Background . . . . .	1
1.2 Challenges in future power systems . . . . .	4
1.3 Research motivation and objectives . . . . .	7
1.4 Control objective categorization . . . . .	10
1.5 Contributions . . . . .	11
1.6 Thesis outline . . . . .	13
<b>2 AC/DC Power System Modeling</b>	<b>15</b>
2.1 Foreword . . . . .	15
2.2 Synchronous generator model . . . . .	16
2.3 LCC model . . . . .	19
2.4 VSC model . . . . .	21
2.5 DC line model . . . . .	25
2.6 Static load model . . . . .	26
2.7 Algebraic mismatch equations . . . . .	26

2.8	Combined AC/DC DAE power system model . . . . .	28
<b>3</b>	<b>POD Control through a Hybrid MTDC Network</b>	<b>31</b>
3.1	Foreword . . . . .	31
3.2	Small signal analysis of power system model . . . . .	32
3.3	Hybrid MTDC network control . . . . .	40
3.4	Test power system . . . . .	41
3.5	SSSA results . . . . .	43
3.6	Time-domain simulation results . . . . .	48
<b>4</b>	<b>Operating Point Adjustment Control through a VSC-MTDC Network</b>	<b>51</b>
4.1	Foreword . . . . .	51
4.2	Calculation of sensitivity to HB . . . . .	52
4.3	Setpoint adjustment in case of load changes . . . . .	55
4.4	Setpoint adjustment in case of faults . . . . .	57
4.5	Test power system . . . . .	59
4.6	Time-domain simulation results . . . . .	61
<b>5</b>	<b>Design of a MISO POD Controller in a VSC-MTDC Network</b>	<b>65</b>
5.1	Foreword . . . . .	65
5.2	Derivation of eigenvalue sensitivity . . . . .	67
5.3	MLQG control design . . . . .	69
5.4	Test power system . . . . .	73
5.5	Results . . . . .	74
<b>6</b>	<b>Supply of a Zero-inertia System through Hybrid MTDC Network</b>	<b>81</b>
6.1	Foreword . . . . .	81
6.2	Converter models in EMTP-RV . . . . .	82
6.3	Test system . . . . .	83
6.4	Hybrid MTDC network control system . . . . .	83
6.5	Converter tripping contingency control schemes . . . . .	86
6.6	Results . . . . .	89
<b>7</b>	<b>Conclusion and Future Work</b>	<b>93</b>
7.1	Conclusion . . . . .	93
7.2	Future Work . . . . .	94
	<b>Bibliography</b>	<b>97</b>

# List of Acronyms

---

AC	Alternating Current
AGC	Automatic Generation Control
AVR	Automatic Voltage Regulator
CCT	Critical Clearing Time
COI	Center Of Inertia
CSC	Current Source Converter
DAE	Differential Algebraic Equation
DC	Direct Current
EHV	Extra High Voltage
EAC	Equal Area Criterion
FCR	Frequency Containment Reserves
FRR	Frequency Restoration Reserves
FRT	Fault Ride Through
HB	Hopf Bifurcation
HV	High Voltage
HVDC	High-Voltage Direct-Current
LCC	Line Commutated Converter
LQR	Linear Quadratic Regulator
MANGO	Modal Analysis for Grid Operations
MISO	Multiple Input Single Output
MLQG	Modal Linear Quadratic Gaussian
MTDC	Multi-Terminal HVDC
PLL	Phase Locked Loop
PMU	Phasor Measurement Unit
POD	Power Oscillation Damping
PTDF	Power Transfer Distribution Factor
PV	Photovoltaic
RES	Renewable Energy Sources

RMS	Root Mean Squared
SIME	Single Machine Equivalent
SISO	Single Input Single Output
SSSA	Small Signal Stability Analysis
TEF	Transient Energy Function
TSO	Transmission System Operator
VSC	Voltage Source Converter
WAMS	Wide Area Measurement Systems

# List of Figures

1.1	HVDC links in Europe. . . . .	8
2.1	Generalized AC/DC power system. . . . .	16
2.2	Static exciter with AVR. . . . .	17
2.3	PSS controller structure. . . . .	18
2.4	PSS controller equivalent model. . . . .	19
2.5	LCC converter . . . . .	20
2.6	DC current control at the LCC . . . . .	21
2.7	VSC converter represented by average model . . . . .	22
2.8	DC voltage droop control. . . . .	23
2.9	Reactive power/AC voltage controller. . . . .	24
2.10	DC line model . . . . .	25
3.1	Locations of stable modes in complex plane. . . . .	35
3.2	Open loop system for the residue of the mode $\lambda_i$ . . . . .	39
3.3	Closed loop system for the residue of the mode $\lambda_i$ . . . . .	39
3.4	Controller configuration for $H(s, K)$ . . . . .	39
3.5	Displacement of mode using the feedback controller $H(s, K)$ . . . . .	40
3.6	AC/DC power system with hybrid MTDC network . . . . .	41
3.7	Effect of changing $K_{p-critical}^{Eq2}$ on the damping of mode $\lambda_{8,9}$ . . . . .	46
3.8	Effect of PSS gain variation on $K_{p-critical}^{Eq2}$ . . . . .	46
3.9	Effect of changing $K_p^{Eq2}$ . . . . .	48
3.10	Power on L12 following fault clearing. . . . .	49
4.1	HB occurrence as shown in complex plane. . . . .	54
4.2	Flow chart for the calculation of optimized controller setpoints. . . . .	56
4.3	Inter-area AC and DC interconnections. . . . .	58
4.4	Test system with embedded VSC-MTDC. . . . .	60

4.5	Variation of power flow over the tie line following a 25% load power increase at bus 23 applied for 0.1 s. . . . .	61
4.6	$\delta_{SIME}-\omega_{SIME}$ phase portrait without operating point adjustment. . . . .	62
4.7	$\delta_{SIME}-\omega_{SIME}$ phase portrait with operating point adjustment. . . . .	62
4.8	POD control as compared to operating point adjustment. . . . .	63
4.9	Power flow over the tie line following short circuit at bus 7. . . . .	63
5.1	General structure of WAMS control. . . . .	66
5.2	State space block diagram of linearized power system model. . . . .	67
5.3	MLQG controller structure. . . . .	71
5.4	Time delay representation. . . . .	72
5.5	Incorporation of conventional POD controller. . . . .	73
5.6	Incorporation of MLQG-based POD controller. . . . .	73
5.7	Three-area test power system. . . . .	74
5.8	Mode shape of $\lambda_{4,5}$ . . . . .	75
5.9	Variation of inter-area modes due to POD controller placement. . . . .	76
5.10	Power flow over $L_{9-17}$ following temporary load increase at bus 9. . . . .	77
5.11	Variation in output power at VSC1 due to POD control. . . . .	78
5.12	Power flow over $L_{10-11}$ following three-phase fault at bus 10. . . . .	79
6.1	LCC representation in EMTP-RV. . . . .	82
6.2	VSC representation in EMTP-RV. . . . .	82
6.3	Test power system with hybrid MTDC network. . . . .	83
6.4	DC voltage control at LCC. . . . .	83
6.5	Active power control at LCC. . . . .	84
6.6	Direct control strategy at the VSC. . . . .	84
6.7	Vector control strategy at the VSC. . . . .	85
6.8	Flow chart for control scheme handling the tripping of LCC1. . . . .	87
6.9	LCC1 tripping scheme operation. . . . .	87
6.10	Flow chart for control scheme handling the tripping of VSC1. . . . .	88
6.11	Operation of control scheme handling the tripping of VSC1. . . . .	88
6.12	DC voltage at LCC2 upon the tripping of LCC1. . . . .	89
6.13	LCCs' active power outputs upon LCC1 tripping contingency. . . . .	89
6.14	Load power upon LCC1 tripping contingency. . . . .	90
6.15	Load power upon VSC1 tripping contingency. . . . .	90
6.16	System frequency upon VSC1 tripping contingency. . . . .	91
6.17	DC voltage upon DC fault clearing. . . . .	91

# List of Tables

1.1	List of point-to-point HVDC links in Europe. . . . .	9
3.1	Primary control modes for LCCs and VSCs in a hybrid MTDC network. . . . .	41
3.2	Oscillatory modes in the combined AC/DC system. . . . .	44
3.3	Participation factors of the system states in $\lambda_{1,2}$ . . . . .	45
3.4	Variation of $\lambda_{8,9}$ . . . . .	45
3.5	Participation factors of controller states in $\lambda_{8,9}$ . . . . .	47
3.6	Variation of $\lambda_{1,2}$ with POD controller. . . . .	47
3.7	Modal controllability and observability of $\lambda_{1,2}$ at LCC and VSC1. . . . .	47
4.1	VSC control modes in the MTDC network. . . . .	60
5.1	Inter-area modes in the test power system. . . . .	74
5.2	Inter-area mode sensitivities corresponding to potential controller locations. . . . .	75
5.3	Inter-area modes' observability factors for controller input signals. . . . .	77
5.4	Settling times for power flow over $L_{9-17}$ . . . . .	77
6.1	Possible VSC control modes. . . . .	85
6.2	Control scenarios A and B for LCCs and VSCs. . . . .	86



# Chapter 1

## Introduction

### 1.1 Background

Electric power systems have greatly evolved over more than a century. From the earlier systems that consisted of small, isolated generators supplying specific loads, the power grid was formed through the interconnection of multiple generators of different power capacities. The interconnection of generating units and loads into a unified grid was beneficial from both technical and economic points of view, as it provided the flexibility of generating bulk amounts of electric power from different sources, such as hydro and nuclear, and then transmitting this power over long distances to the load centers. The variation of system voltage through transformers allowed to use High Voltage (HV) and Extra High Voltage (EHV) levels in power transmission, thereby reducing losses in the power delivered to the load centers. This in turn allowed the electricity prices to get lower, as consumers were able to buy low-cost power from utilities, the matter which fostered a rapid growth in the spreading of electric power systems and their becoming a vital backbone of modern society. As a result of population growth and consequently, a growth in electric power demand and consumption, inter-regional and cross-border interconnections took their place into modern power system due to economic considerations related to electricity prices and cost-efficient operation of the system [1]- [3], [10, 11].

Despite obvious advantages to the economic operation and reliability of the system, the interconnection of multiple power systems has brought multiple technical challenges that face the system operators and can affect the stability of the power system [19, 20]. As different power systems are connected through AC tie lines with heavy inter-area power flows, low-frequency inter-area power oscillations could be

generated into the interconnected system [16], [81]- [84]. The oscillations are due to groups of generators in both areas oscillating against each other. In the absence of sufficient damping, inter-area oscillations can cause a cascaded blackout into the system, as a result of frequency deviations that trigger under-frequency protection devices of the generators [16, 79], leading up to cascaded loss of generation. As the power industry moves towards more deregulation, inter-area incidents have become a commonplace in system operation, therefore system operators moved towards installing and utilizing supplementary damping controllers to enhance the stability of the interconnected power system. Traditionally, inter-area oscillations have been handled using Power System Stabilizers (PSSs) installed at generators, which are designed to introduce an appropriate phase compensation to increase the damping of a specific oscillatory mode [16, 79, 83]. PSSs typically receive a local input signal, such as generator speed or power, and introduce the damping through a contribution to the Automatic Voltage Regulator (AVR) control circuit. Nevertheless, PSSs' damping performance is not satisfactory in dealing with large power systems with multiple inter-area modes, as the ability of a local signal to capture the presence of an inter-area mode is limited, and the controller structure allows a parameter tuning based on one mode only, and hence it can adversely affect the damping of other well damped modes in the system as well [74]- [76]. The advent in power semiconductor devices, such as thyristor and Insulated Gate Bipolar Transistor (IGBT), made it possible to use Flexible AC Transmission Systems (FACTS), which are power-electronics based controllers for voltage and power control, which are capable of effectively damping the inter-area modes [79, 85]. However due to their high cost, the location of installing FACTS devices needs to be carefully considered [85].

Despite the flexibility offered by AC transmission in power systems, there has been certain transmission scenarios that made it mandatory to utilize DC transmission, such as in case of interconnecting two asynchronous AC systems [7, 11, 65], as well as in case of long-distance and subsea power transmission through cables, in which cases the cost for AC interconnections becomes prohibitively high, in addition to the technical challenges of reactive power compensation over the transmission lines or cables [11, 65]. Thus High Voltage Direct Current (HVDC) transmission became the option of choice in the aforementioned transmission scenarios. The first subsea HVDC link through cables was commissioned in 1954 between the island of Gotland and the Swedish mainland [5], while the Sakuma back-to-back HVDC link was used in 1965 to link the power systems in the east and west of Japan, due to different nominal frequencies in both systems [65]. The early HVDC projects used mercury-arc rectifiers as power devices [7, 65], however with the advent of solid state power devices, solid-state thyristors replaced mercury arc rectifiers. Despite

its multiple advantages, such as low switching losses and high reliability, however thyristor-based Line Commutated Converter (LCC)-based HVDC links suffered from the following disadvantages [5]- [7], [11], [65]:

- There is a need for a strong AC grid to enable LCCs' operation, as the thyristors' commutation is completely dependent on the connected AC grid.
- As a result of AC grid-dependent switching of converter switches, a high amount of harmonics is generated in the AC line, therefore significant harmonic filtering is required on the AC side of the converters.
- The operation of a Multi-Terminal HVDC (MTDC) network suffers from an operational difficulty, as the reversal of power flow through a converter requires the reconnection of its terminals and consequently, the reversal of DC voltage polarity across the converter. Hence, LCC-based MTDC network was operated with up to three-terminals only, as in the SACOI DC tie between Italy, Corsica, and Sardinia, as well as the Quebec-New England DC tie between the province of Quebec and the US state of New Hampshire.

With the advent of fully controlled semiconductor power devices, namely the IGBT, Voltage Source Converter (VSC)-HVDC links found their way into application, with the first VSC-HVDC link commissioned in 1997 [5]- [7]. The major advantage of a VSC is that it behaves as a voltage source on the DC side, and therefore the reversal of power flow through the converter does not require the reconnection of converter terminals [9, 65]. As the VSC's power devices are fully controlled ones, the converter can be controlled to achieve an independent control of active and reactive powers [9, 12], as well as to connect to weak or passive AC networks [12]- [14]. Moreover, as the dominant harmonics resulting from the VSC switching are of high frequencies that are close to the switching frequency, the size and rating of the required harmonic filters are significantly lower than those needed for the LCC operation [9, 13, 65]. Despite these advantages, VSC-HVDC links are characterized by high switching losses as a result of high switching frequency of the converters' power devices [9, 12, 65]. As a result of the VSC's fixed DC voltage polarity and its ability to independently control its active and reactive power outputs, there has been a high interest in investigating the multi-terminal operation of multiple VSCs. As the converter commutation in a VSC is independent of the connected AC grid, a VSC-MTDC can be capable of interconnecting various segments of the power system of different strengths [9, 11]. Moreover, as the converters in a VSC-MTDC network are capable of quickly adjusting their active and reactive

power outputs, they are capable of contributing to the stability enhancement in the connected AC grids, provided that appropriate control strategies are used towards that goal [10]. In this vein, the power system stability can be loosely defined as the ability to restore a system's normal operation after being subjected to a disturbance. The power system stability can be categorized as follows [16, 22]:

- **Rotor angle stability:** which refers to the ability of an interconnected power system to remain in synchronism after being subjected to a disturbance. Instability that may result occurs in the form of increasing angular swings of some generators leading to their loss of synchronism with other generators. The rotor angle stability may be further categorized into the following [22]:
  - **Small-signal stability:** which is concerned with the ability of the system to maintain synchronism under small disturbances.
  - **Transient stability:** which is concerned with the ability of the system to maintain synchronism when subjected to a large disturbance, such as a short circuit on a transmission line.
- **Voltage stability:** which refers to the ability of the system to maintain a steady voltage after being subjected to a disturbance from a given initial operating point. Instability that may result occurs in the form of a progressive fall or rise of voltages of some buses.
- **Frequency stability:** refers to the ability of a power system to maintain steady frequency following a severe system upset resulting in a significant imbalance between generation and load. Instability that may result occurs in the form of sustained frequency swings leading to tripping of generators and/or loads.

This thesis is focused on the utilization of MTDC network controls for the purpose of enhancing the rotor angle stability in the interconnected AC/DC power system.

## 1.2 Challenges in future power systems

Nowadays, the futuristic scenarios for European power systems bring a multitude of challenges to system operators, primarily due to the increasing share of renewable energy sources in the system, such as wind and solar power. As the distributed energy sources are both scattered and intermittent, large-scale integration of these

sources is bringing heavy long-distance power flows in power system operation [1]-[3]. Given the current state of system operation that brings the transmission system close to its stability limits, there is a growing need to implement grid expansion in a way that strengthens the power system and maintains the stability and security of supply [3,4,17]. In this vein, grid expansion shall consider a number of technical, economic, and environmental aspects related to the new investments in the grid. In recent times, grid expansion in the form of investments in new AC transmission lines can be prohibitively costly and time-consuming. The technical constraints typically relate to the difficulties encountered in case of very long transmission distances, as the control of reactive power and voltages at the line ends becomes problematic. The critical distance at which these problems are encountered is even shorter for AC cables, as it becomes necessary to reduce the power flow through the cable as a result of the capacitive charging current. The critical length refers to the length at which the cable's capacitive charging current becomes equal to the its rated current. The critical length generally decreases as the transmission voltage level increases, therefore limiting the use of HV and EHV cables for long distances [9, 11, 13]. On the other hand, the economic constraints relate to the high investment cost in AC grid expansion, particularly as the transmission distance increases. The additional costs come as a result of the need to install reactive power compensation devices to regulate the voltage over the lines [5]. Environmental and social constraints also impede transmission expansion using overhead AC lines, as the public is usually opposed to the construction of new lines due to the potential health effects of the electromagnetic fields induced by the lines, as well as the visual impact of the overhead lines from an urban planning point of view [17, 19, 20].

As the future power grid is anticipated to integrate a large number of renewable energy sources, there is a growing need to boost the inter-regional transmission capacity over existing tie lines, as well as to invest in new interconnections. The investment in inter-regional power system interconnections aims to enable the flow of power generated by various renewable energy resources that are sparsely distributed across distant geographical areas [8, 10, 17]. For instance, the hydro power in Scandinavia can be traded and balanced against the offshore wind power in the north sea. On the other hand, the Photo Voltaic (PV)-generated power from North Africa can be transmitted to southern Europe [19, 20]. In order to obtain such power flow corridors with heavy power flows over long distances, the AC option seems less attractive and more challenging as compared to the DC option, due to the aforementioned techno-economic constraints. Thus, power transmission through HVDC networks is envisioned to play an increasingly important role in the future power system in Europe, as well as worldwide [10]. The futuristic scenario

envisions the establishment of an overlay MTDC network that is embedded within the interconnected AC power systems, in such a way that facilitates the integration of sparsely located distributed energy sources [10].

The new investment in an overlay grid that supports the current interconnected European power system is referred to as a supergrid [10]. Although both AC and DC options were considered for the new grid, the DC option proves more feasible for multiple reasons, including [10, 38]:

- Lower losses for long distances, as the skin effect does not take place in case of DC power transmission.
- Suitability for cable transmission, as the DC cables do not suffer from the limitations caused by the flow of charging current. This gives an edge for the DC option when considering the integration of remotely located renewable energy sources, such as offshore wind farms.
- Capability of power control, as the MTDC converters are inherently capable of controlling the amount of active power through the DC lines.

Nevertheless, multiple challenges are still to be met by the power system operators before the futuristic vision of a DC supergrid can be achieved. The following are some of the provisioned challenges that face the operation of a MTDC grid [10, 65]:

- DC voltage control: the DC voltage reflects the power balance in a MTDC grid, which is analogous to frequency in the AC grid [10, 45]. Therefore DC voltage control is critical to the stability of the MTDC grid. The DC voltage control strategies in MTDC networks can be classified into master-slave control, droop control, and voltage margin control [45]. The DC voltage control function should be secure and dependable so as to avoid a collapse of the MTDC network operation in case of losing the voltage controlling station.
- AC/DC control coordination: as the MTDC network controls interact with the connected AC systems, there needs to be coordinated control strategy of the combined AC/DC system to ensure the system's stable and secure operation [10, 72].
- Lack of dependable DC circuit breaker: as the DC current does not have a natural zero-crossing, the interruption of DC currents is more difficult as compared to AC currents. This has led to operational problems related to the DC circuit breakers [86]. Although multiple manufacturers have produced

prototypes of high-power circuit breakers, power utilities are still reluctant to utilize DC circuit breakers as the technology has not matured yet.

- Converter types: both LCC and VSC have been considered for the MTDC grid. However as the LCC requires the reconnection of its terminals for the reversal of power flow, the VSC seems more attractive for the MTDC operation. Nevertheless, a hybrid MTDC grid that combines both LCC and VSC converters has been proposed in literature [10, 15]. In a hybrid configuration, the LCC can be used for a single operating mode (i.e. either as a rectifier, or as an inverter), while the VSC can vary its operating mode.
- MTDC grid protection: as a result of the DC dynamics being much faster than AC dynamics, the protection system of a MTDC poses a technical challenge to system operators. The DC fault detection and clearing have to be faster than the AC faults, and hence the AC protection strategies are not readily applicable [86].

### 1.3 Research motivation and objectives

As a result of an increasing share of renewable energy sources replacing conventional generation, MTDC networks are a prospected solution for the integration of these renewable sources, which are distributed over large geographical areas, such as offshore wind farms, and solar power generation. Due to various technical and economic factors, the integration of these sources using AC transmission is both difficult and prohibitively costly, and hence the envisioned solution for the renewables' integration is through MTDC networks. The rationale behind adopting the MTDC network solution is that they are capable of spanning over long distances and receiving the power from renewable sources, as well as delivering this power to various connected AC grids [10, 86]. From the power system stability point of view, the interest in MTDC networks emanates from the converters' ability to control the power flow in DC lines, as well as to quickly adjust their output powers [6, 10, 16]. Unlike generators, the power electronic converters' operation is static and does not involve rotating masses, the control is rather implemented by the variation of switching pulses delivered to the converter power devices, and therefore the converter control is a fast one [16, 65]. Thus the converters are considered as fast-acting elements that can impact the power system stability. The interest in investigating appropriate control strategies for MTDC networks emanates from the multiple benefits that can be achieved for the power grid through the converters.

On one hand, the independent control of active and reactive power output of a VSC makes it capable of operating as a synchronous machine without inertia, and therefore it represents a versatile asset during system operation [9, 11]. On the other hand, the supplementary control through auxiliary controllers makes it possible to modulate the active and reactive power outputs of the VSC for the purpose of stability enhancement and/or frequency support [26, 27]. In this vein, the objectives of the research work in this thesis were set to the utilization of both primary and supplementary controls for the enhancement of the power system stability.

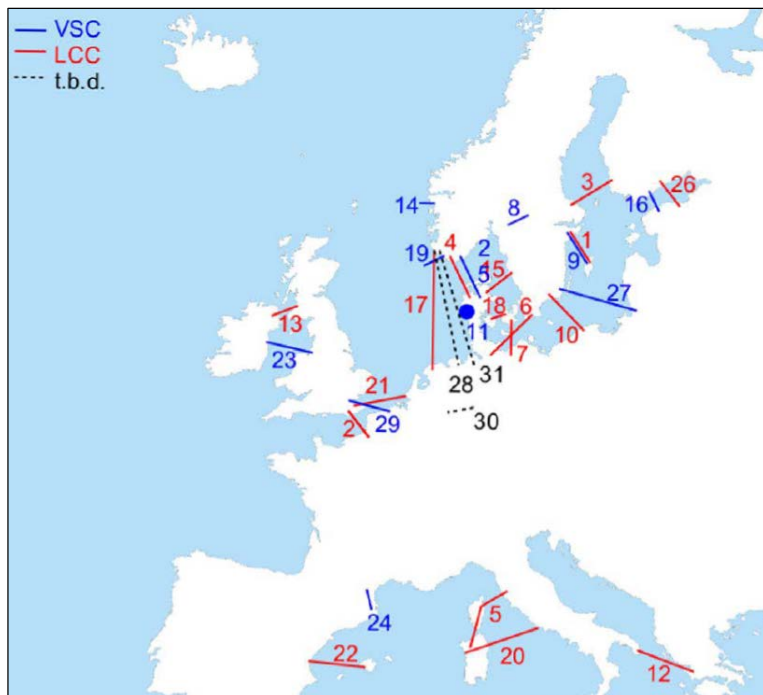


Figure 1.1: HVDC links in Europe.

As the MTDC network controls interact with the connected AC systems, both AC and DC system controls have to be coordinated in order to ensure a secure and stable operation of the combined AC/DC power system. Although multiple investigations on the coordinated control of the AC/DC system were presented in the literature, fewer studies dealt with the stability analysis of the combined AC/DC system as a whole, as opposed to the analysis of DC voltage control in the MTDC network. An interest in hybrid MTDC comes from the fact that there are multiple

Table 1.1: List of point-to-point HVDC links in Europe.

ID	Project	Location	DC voltage (kV)	Rating(MW)	Type
1	Gotland	Sweden	$\pm 100$	20	LCC
2	Cross Channel BP	France-UK	$\pm 270$	2000	LCC
3	Fenno-Skan	Finland-Sweden	400	500	LCC
4	Skagerrak 3	Norway-Denmark	$\pm 350$	500	LCC
5	Sacoi	Italy-Corsica-Sardinia	$\pm 200$	300	LCC
6	Baltic cable	Sweden-Germany	450	600	LCC
7	Kontek	Denmark-Germany	400	600	LCC
8	Hellsjön	Sweden	$\pm 10$	3	VSC
9	Gotland HVDC Light	Sweden	$\pm 60$	50	VSC
10	SwePol link	Sweden-Poland	$\pm 450$	600	LCC
11	Tjaereborg	Denmark	9	7	VSC
12	Grita	Greece-Italy	400	500	LCC
13	Moyle interconnector	Ireland-Scotland	250	$2 \times 250$	LCC
14	Troll A	Norway	$\pm 60$	$2 \times 40$	VSC
15	Konti-Skan 1	Denmark-Sweden	$\pm 250$	250	LCC
16	Estlink	Estonia-Finland	$\pm 150$	350	VSC
17	NorNed	Norway-Netherlands	$\pm 450$	700	LCC
18	Sorebaelt	Denmark	400	600	LCC
19	Valhall	Norway	150	78	VSC
20	Sapei	Italy-Sardinia	$\pm 500$	1000	LCC
21	BritNed	UK-Netherlands	$\pm 450$	1000	LCC
22	Romulo	Spain-Mallorca	$\pm 250$	$2 \times 200$	LCC
23	East-West interconnector	Ireland-UK	$\pm 200$	500	VSC
24	INEFLE	France-Spain	$\pm 320$	2000	VSC
25	Skagerrak 4	Norway-Denmark	500	700	VSC
26	Estlink 2	Estonia-Finland	$\pm 450$	670	LCC
27	NordBalt	Sweden-Lithuania	$\pm 300$	700	VSC
28	NorGer	Norway-Germany	$\pm 450-500$	1400	LCC
29	Nemo	UK-Belgium	320-500	1000	VSC
30	Alegro	Belgium-Germany	$\pm 320$	500-1000	VSC
31	Nordlink	Norway-Germany	$\pm 525$	1400	VSC

point to point LCC-HVDC and VSC-HVDC links that are already into operation, as shown in Fig. 1.1. A list of these projects is shown in Table. 1.1. The connection of some of these links would certainly be of interest to create an overlay grid within the interconnected AC grids [14, 31]. To the best of the author's knowledge, there has been no studies in the existing literature on the topic of small signal analysis of an AC/DC system with a hybrid MTDC network, as well as on the topic of stability enhancement through operating point adjustment of an embedded VSC-MTDC network.

The thesis aims to investigate the stability enhancement of the combined AC/DC power system through the use of primary and secondary MTDC network controls.

The MTDC networks considered include both hybrid MTDC networks, as well as VSC-MTDC networks. In order to achieve this aim, this research has the following objectives:

- To develop a mathematical model for an AC/DC power system that includes a hybrid MTDC network.
- To investigate the Power Oscillation Damping (POD) in the AC system through supplementary controllers used at the hybrid MTDC network converters.
- To investigate the stability enhancement of an AC/DC power system through operating point adjustment strategy, applied through setpoint adjustment in an embedded VSC-MTDC network.
- To investigate the design and optimal placement of a Multi-Input Single Output (MISO) controller in an embedded VSC-MTDC network.
- To investigate the control scheme and performance of a hybrid MTDC system that is supplying a zero-inertia network.

## 1.4 Control objective categorization

In the context of this thesis, the control objectives for MTDC network converters can be classified into the following categories [10, 43, 50]:

- Primary control: which refers to the regulation of DC voltage in the MTDC network, as well as to the regulation of active power outputs of the converters that are exchanged with the AC system.
- Supplementary control: which refers to the additional control functions that can be conducted by means of auxiliary controllers at the converters, such as Power Oscillation Damping (POD) and frequency support.

The above categories refer to the objectives of converter controllers. Therefore for MTDC network converters, the primary controllers are the DC voltage and active power power controllers. On the other hand, the supplementary controllers are the POD controllers. The thesis tackles the utilization of both primary and supplementary controllers in MTDC networks for the purpose of dynamic and transient stability enhancement.

The main objective of this thesis is to utilize the MTDC network controls toward the goals of enhancing the power system stability, as well as increasing the inter-regional power transfer. The research conducted in the thesis focuses on the strategies used at both primary and secondary converter controls in order to enhance the power system's dynamic and transient stability. The research aims at identifying the challenges posed by the existing interconnections in the power system, as well as utilizing the MTDC network controls to respond to these challenges. The thesis also tackles the challenge of coordinating multiple damping controllers to avoid adverse control interactions that could negatively impact the overall damping in the system.

## 1.5 Contributions

The contributions of this thesis are summarized as follows:

- To derive a mathematical model for power systems with a hybrid MTDC network. The model combines the average model of the VSC together with the response model of the LCC, and acts as a unified platform for both time-domain simulation and small signal analysis [Paper J1].
- To implement the control coordination between LCC and VSC controllers, as well as the control coordination between POD and PSS controllers [Paper J1].
- To present an application of dynamic stability enhancement through operating point adjustment using VSC-MTDC network controls. The adjustment is based on the system stability margin's sensitivity to Hopf Bifurcation (HB) [Paper J2].
- To propose a method for transient stability enhancement through operating point adjustment using VSC-MTDC network controls. The adjustment is based on optimized Power Transfer Distribution Factors (PTDFs) [Paper J2].
- To present the placement and design of a Multi-Input Single Output (MISO) controller used for supplementary POD control in the VSC-MTDC network, based on MLQG control strategy [Paper C2].
- To propose a control system and hierarchy for a hybrid MTDC network that feeds into a zero-inertia AC grid with no available generation [Paper C1].

- To present a comparison between two distinct approaches for voltage and frequency control at the receiving end network, and to demonstrate the effectiveness of one approach in improving the quality of supply in case of contingencies [Paper C1].

## List of publications

The following articles were published during the PhD studies:

### JCR journal papers:

- [J1] O. Kotb, M. Ghandhari, R. Eriksson, V. K. Sood, "On small signal stability of an AC/DC power system with a hybrid MTDC network", *Electric Power Systems Research*, Vol. 136, pp. 79-88, July 2016
- [J2] O. Kotb, M. Ghandhari, R. Eriksson, R. Leelaruji, V. K. Sood, "Stability enhancement of an interconnected AC/DC power system through VSC-MTDC operating point adjustment", *Electric Power Systems Research*, vol. 151, pp 308-318, October 2017

### Peer-reviewed conference papers:

- [C1] O. Kotb, M. Ghandhari, R. Eriksson, V. K. Sood, "A study on the control of a hybrid MTDC supplying a passive load", IEEE International Conference on Power System Technology (POWERCON 2014), Chengdu, China, Oct. 2014.
- [C2] O. Kotb, M. Ghandhari, J. Renedo, L. Rouco, R. Eriksson, "On the design and placement of a supplementary damping controller in an embedded VSC-MTDC network", IEEE International Conference on Innovative Smart Grid Technologies (ISGT Europe 2017), Torino, Italy, Sep. 2017

## 1.6 Thesis outline

The outline of this thesis is given as:

- Chapter 2 presents the mathematical models of the power system components, such as generators, converters, and controllers. The chapter also presents the small signal analysis of the power system model.

- Chapter 3 presents the research work and results for the utilization of a hybrid MTDC network for stability enhancement through POD control.
- Chapter 4 presents the research work and results for the utilization of an embedded VSC-MTDC network for stability enhancement through operating point adjustment.
- Chapter 5 presents the research work and results for the utilization of MLQG-based POD controllers in embedded VSC-MTDC networks.
- Chapter 6 presents the research work and results for the utilization of a hybrid MTDC network to supply a zero-inertia AC system.
- Chapter 7 presents the conclusions of the thesis and some of the foreseen future work.



## Chapter 2

# AC/DC Power System Modeling

This chapter presents the mathematical models of the system components such as converters, generators, and their controllers. The chapter also presents the Differential Algebraic Equation (DAE) model of the combined AC/DC power system.

### 2.1 Foreword

The electric power system generally comprises three distinct stages: generation, transmission, together with the distribution and loads. The power is first generated by the generating units at a low to medium voltage level. The generated power is then passed through step up transformers which raise the voltage level to a high voltage that is suitable for sending the power over long distances through the transmission lines of the grid to the load centers. Next, step down transformers receive the power and lower the voltage to a voltage that is suitable for power distribution to various residential, commercial, and industrial loads. Hence, in order to produce a model that reflects the power system, various elements such as generators, transformers, transmission lines, and loads need to be appropriately modeled. Power systems are naturally described by DAEs, where the differential equations describe the dynamic elements of the system, such as generators, converters, and controllers, while the algebraic equations describe the power flow equations in the system. A generalized AC/DC system is shown in Fig. 2.1. This chapter presents the individual models of the power system components, as well as the DAEs used to describe the dynamic of the power system in this thesis.

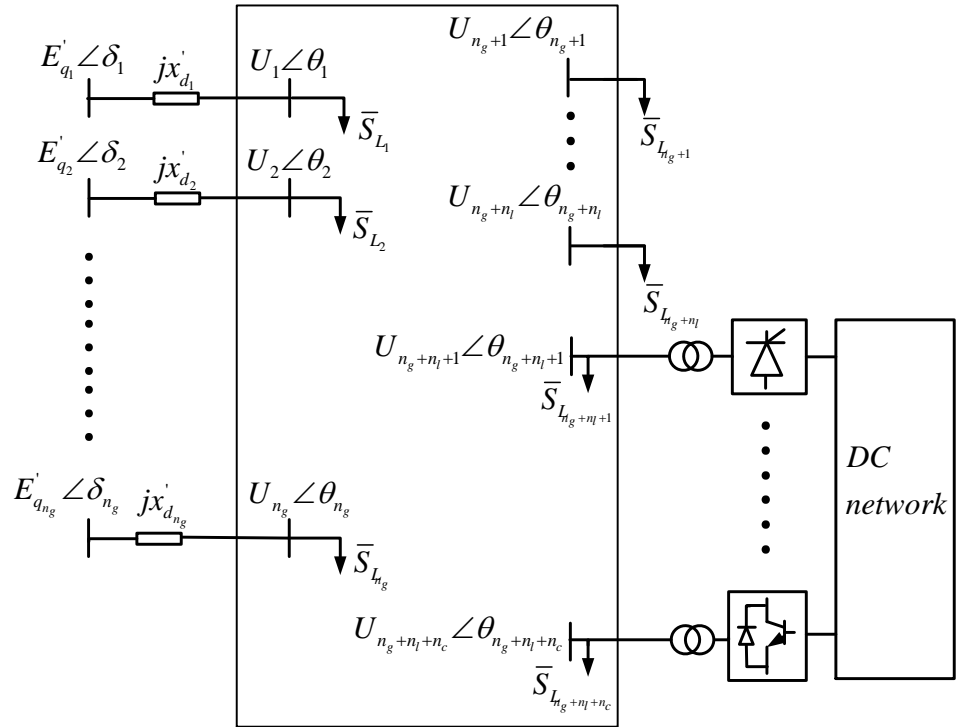


Figure 2.1: Generalized AC/DC power system.

## AC system model

### 2.2 Synchronous generator model

A synchronous generator can be modeled with different degrees of detail depending on the nature of power system study at hand. While the classical model only represents the generator's rotor angle and speed, the one-axis model also represent the generator's internal emf. The generator's one-axis mode is given as follows [87], for  $i = 1, \dots, n_g$ :

$$\dot{\delta}_i = \omega_i \quad (2.1)$$

$$\dot{\omega}_i = \frac{1}{M_i} \left( P_{mi} - \frac{U_i E'_{qi} \sin(\delta_i - \theta_i)}{x'_{di}} \right) \quad (2.2)$$

$$\dot{E}'_{qi} = \frac{1}{T'_{di}} \left( E_{fdi} - \frac{x_{di}}{x'_d} E'_{qi} + \frac{x_{di} - x'_{di}}{x'_{di}} U_i \cos(\delta_i - \theta_i) \right) \quad (2.3)$$

where  $n_g$  is the number of generators in the system.  $\delta_i$  is the generator rotor angle,  $\omega_i$  is the generator speed deviation from synchronous speed,  $M_i$  is the generator inertia constant,  $P_{mi}$  is the input mechanical power to the generator,  $U_i$  is the generator bus voltage,  $\theta_i$  is the generator bus angle,  $E'_{qi}$  is the internal emf of the generator,  $T'_{di}$  is the generator transient open circuit time constant,  $E_{fdi}$  is the field voltage,  $x_d$  and  $x'_d$  are the generator synchronous and transient equivalents reactances, respectively, including the generator transformer reactance.

A high gain of the Automatic Voltage Regulator (AVR) is used in the excitation system to improve the transient stability in the power system. Nevertheless, high exciter gains may result in a deterioration in small-signal stability of the power system. In order to avoid small-signal stability problems, Power System Stabilizers (PSSs) are used to enhance the damping in the system by providing a contribution to the voltage regulation [87]. A block diagram representation of the excitation system is shown in Fig. 2.2, where  $K_A$  is the exciter gain of the AVR,  $U_{ref}$  is the reference voltage of the AVR,  $T_e$  is the exciter time constant, and  $u_{damp}$  is the contribution of the PSS to the exciter voltage. According to the block diagram, the dynamic of the exciter is given by:

$$\dot{E}_{fdi} = \frac{1}{T_{ei}} \left( -E_{fdi} + K_{Ai} (U_{refi} + u_{dampi} - U_i) \right) \quad (2.4)$$

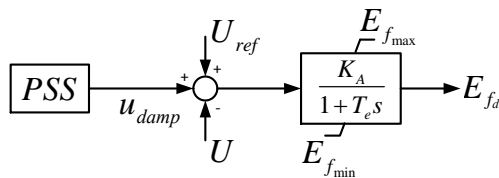


Figure 2.2: Static exciter with AVR.

A PSS model with a washout filter and lead-lag compensator is shown in Fig. 2.3. The washout filter is a high-pass filter that blocks contribution in case of a steady-state deviation of the input signal. The lead-lag block shifts the phase by setting  $T_1$ - $T_4$  at values so that a positive contribution to damping is obtained.

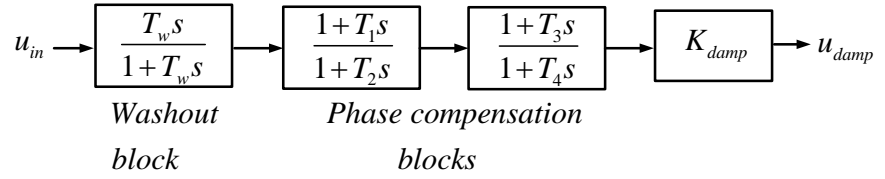


Figure 2.3: PSS controller structure.

The PSS model in Fig. 2.3 is redrawn to the equivalent block diagram in Fig. 2.4 for the purpose of writing the PSS's dynamic equations as a set of first order differential equations. The PSS dynamic is given as:

$$\dot{S}_{1i} = \frac{1}{T_{wi}} (u_{in} K_{damp} - S_{1i}) \quad (2.5)$$

$$\dot{S}_{2i} = \frac{1}{T_{2i}} (c_{2i} - S_{2i}) \quad (2.6)$$

$$\dot{S}_{3i} = \frac{1}{T_{4i}} (c_{4i} - S_{3i}) \quad (2.7)$$

where the intermediate states  $c_{1i}$ ,  $c_{2i}$ ,  $c_{3i}$  and  $c_{4i}$  are given as:

$$c_{1i} = u_{in} K_{damp} - S_{1i} \quad (2.8)$$

$$c_{2i} = c_{1i} \left(1 - \frac{T_{1i}}{T_{2i}}\right) \quad (2.9)$$

$$c_{3i} = c_{1i} \frac{T_{1i}}{T_{2i}} + S_{2i} \quad (2.10)$$

$$c_{4i} = c_{3i} \left(1 - \frac{T_{3i}}{T_{4i}}\right) \quad (2.11)$$

The PSS lead-lag parameters can be tuned via different methods to maximize the gain of least damped oscillatory mode in the system. The dynamic equations for PSS state variables are given as:

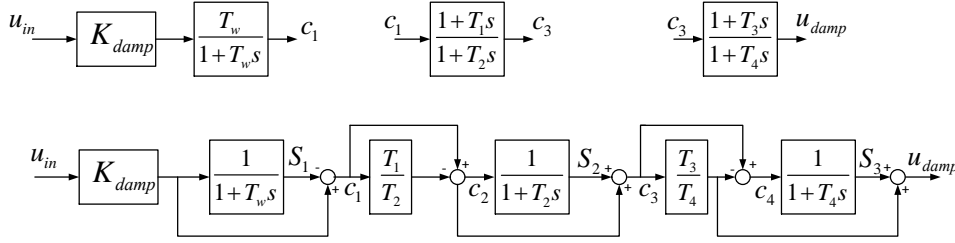


Figure 2.4: PSS controller equivalent model.

$$\dot{S}_{1i} = \frac{K_{damp}}{T_{wi}} \omega_i - \frac{1}{T_{wi}} S_{1i} \quad (2.12)$$

$$\dot{S}_{2i} = \frac{K_{damp}(T_{2i} - T_{1i})}{T_{2i}^2} S_{1i} \omega_i - \frac{T_{2i} - T_{1i}}{T_{2i}^2} S_{1i} - \frac{1}{T_{2i}} S_{2i} \quad (2.13)$$

$$\dot{S}_{3i} = K_{damp} \frac{T_{1i}}{T_{2i}} \frac{T_{4i} - T_{3i}}{T_{4i}^2} \omega_i - \frac{T_{1i}}{T_{2i}} \frac{T_{4i} - T_{3i}}{T_{4i}^2} S_{1i} + \frac{T_{4i} - T_{3i}}{T_{4i}^2} S_{2i} - \frac{1}{T_{4i}} S_{3i} \quad (2.14)$$

Hence, the vector of state variables of a generator ( $x_{ACi}$ ) is given by:

$$x_{ACi} = \left[ \delta_i \quad \omega_i \quad E'_{qi} \quad E_{fdi} \quad S_{1i} \quad S_{2i} \quad S_{3i} \right]^T \quad (2.15)$$

Finally, the vector of state variables of the system generators ( $x_{AC}$ ) in Fig. 2.1, is given as:

$$x_{AC} = \left[ x_{AC1} \quad \dots \quad x_{ACn_g} \right]^T \quad (2.16)$$

where  $n_g$  is the number of generators in the system.

## DC system model

### 2.3 LCC model

#### LCC circuit model

The LCC was represented by the response model [16, 65]. The response model is suitable for stability studies, as it represents the basic quantities involved in the

operation of the LCC, such as the DC current ( $I_{dc}$ ) and the firing angle ( $\alpha$ ). The LCC representation is shown in Fig. 2.5. The state equation for the DC current of

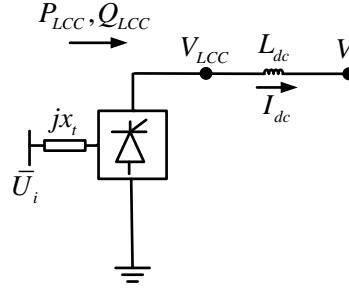


Figure 2.5: LCC converter

the LCC is given as follows:

$$\dot{I}_{dc} = \frac{1}{L_{dc}}(V_{LCC} - V_i) \quad (2.17)$$

where  $V_{LCC}$  is the LCC's output DC voltage and  $V_i$  is the DC network voltage at the LCC terminal.  $V_{LCC}$  is given as:

$$V_{LCC} = V_{dc10} \cos(\alpha) - c_{LCC} I_{dc} \quad (2.18)$$

where  $V_{dc10}$  is the no-load output voltage of the LCC, and  $c_{LCC}$  is the DC current constant of the LCC. The constants  $V_{dc10}$  and  $c_{LCC}$  are given by:

$$V_{dc10} = \frac{3N_b \sqrt{2}}{\pi} U_i \quad c_{LCC} = \frac{3x_t}{\pi} \quad (2.19)$$

where  $N_b$  is the number of bridges in the LCC,  $U_i$  is the magnitude of converter bus voltage, and  $x_t$  is the reactance of converter transformer.

Assuming the presence of  $n_{LCC}$  converters in the system, the vector of state variables of the LCC currents is given by:

$$x_{LCC} = [I_{dc1} \quad \dots \quad I_{dcn_{LCC}}]^T \quad (2.20)$$

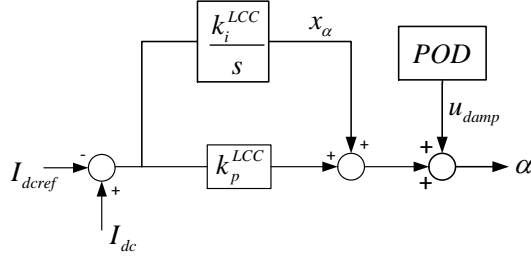


Figure 2.6: DC current control at the LCC

### LCC controller model

The case of DC current control is considered for the LCC, as the connected AC networks are assumed to be active ones that are capable of securely supporting the converter commutation [65]. The DC current is regulated by means of the firing angle ( $\alpha$ ) [16, 65]. Considering DC current control mode for the LCC, the current controller is shown in Fig. 2.6. The firing angle ( $\alpha$ ) of the LCC is used to regulate the DC current. Based on the configuration in the figure, the controller equations are given as:

$$\alpha = x_\alpha + k_p^{LCC}(I_{dc} - I_{dcref}) + u_{damp} \quad (2.21)$$

$$\dot{x}_\alpha = k_i^{LCC}(I_{dc} - I_{dcref}) \quad (2.22)$$

where  $k_p^{LCC}$  and  $k_i^{LCC}$  are the proportional and integral gains of the current controller, respectively, and  $x_\alpha$  is the state variable of the controller. The POD controller shown in Fig. 2.6 can be used for the purpose of damping the power oscillations at the connected AC system in case of disturbances. The contribution given by the POD controller is represented by  $u_{damp}$ .

## 2.4 VSC model

### VSC circuit model

The VSC model is shown in Fig. 2.7, where  $V_i$  is the DC voltage at the VSC terminal,  $C_{dc}$  is the capacitor installed across the DC side of VSC,  $x_l$  is the reactance



Figure 2.7: VSC converter represented by average model

of converter transformer,  $U_i$  is the AC voltage of the converter bus, and  $E_c$  is the controllable voltage of the VSC. The AC voltage at the converter bus is given by  $\bar{U}_i = U e^{j\theta_i}$ . Based on the average model representation, the AC voltage generated by the VSC is represented as a voltage source with controllable magnitude ( $E_c$ ) and phase angle ( $\gamma_c$ ). The AC voltage generated by the VSC is given as follows:

$$\bar{E}_c = E_c e^{j\gamma_c} = E_c \cos(\gamma_c) + j E_c \sin(\gamma_c) = E_d + j E_q \quad (2.23)$$

where  $E_d$  and  $E_q$  are the controlled components of the VSC voltage. Based on the controlled components, the VSC voltage magnitude and angle are given as follows:

$$E_c = \sqrt{E_d^2 + E_q^2} \quad (2.24)$$

$$\gamma_c = \tan^{-1} \left( \frac{E_q}{E_d} \right) \quad (2.25)$$

Assuming negligible power losses in the converter, the active and reactive power exchanged between the VSC and the connected AC system can be given as follows:

$$P_c = \frac{U_i E_c}{x_t} \sin(\theta_i - \gamma_c) = \frac{U_i}{x_t} (E_d \sin \theta_i - E_q \cos \theta_i) \quad (2.26)$$

$$Q_c = \frac{U^2}{x_t} - \frac{U_i E_c}{x_t} \cos(\theta_i - \gamma_c) = \frac{U_i^2}{x_t} - \frac{U_i}{x_t} (E_d \cos \theta_i + E_q \sin \theta_i) \quad (2.27)$$

Having assumed negligible losses in the VSC, it is now possible to write the state equation of the DC voltage at the VSC as follows:

$$\dot{V}_i = \frac{1}{C_{dc}} \left( \frac{P_c}{V_i} - I_i \right) \quad (2.28)$$

### VSC controller model

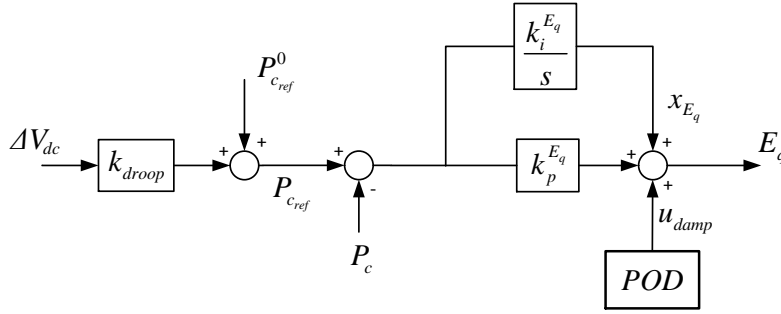


Figure 2.8: DC voltage droop control.

The block diagram of DC voltage/active power controller is shown in Fig. 2.8, where  $P_{c_{ref}}^0$  is the active power setpoint at the converter station,  $P_c$  is the active power output of the converter, while  $k_{droop}$  is the DC voltage droop constant, which is introduced to provide a contribution to DC voltage control by the converter.  $k_i^{E_q}$  and  $k_p^{E_q}$  are the integral and proportional gains of the controller, respectively, while  $x_{E_q}$  is the state variable of the controller. The PI controller handles the error between reference point and feedback value and ensures a zero-steady state error. The controller structure can be used to explain the operation of both droop control and master-slave control as follows:

- In case of master-slave control, the value of DC voltage droop  $k_{droop}$  is equal to zero. In this case, the DC voltage control duty is assigned to one converter only, while the remaining converters are operated in active power control mode. The PI control in the inner loop controller is implemented by introducing the control error ( $P_{c_{ref}} - P_c$ ) to the proportional and integral parts of the controller. Hence, the output of the integrator is modelled as the state variable of the controller, which is added to the output of the proportional part of the controller. The controller equations in case of master-slave DC voltage control are given by:

$$E_q = k_p^{E_q} (V_{dcref} - V_{dc}) + x_{E_q} + u_{damp} \quad (2.29)$$

$$\dot{x}_{E_q} = k_i^{E_q} (V_{dcref} - V_{dc}) \quad (2.30)$$

- In case of droop control, the DC voltage control function is distributed over multiple converters in the MTDC network [45]. Based on Fig. 2.8, the controller equations are given as:

$$E_q = k_p^{E_q} (P_{cref} - P_c) + x_{E_q} + u_{damp} \quad (2.31)$$

$$\dot{x}_{E_q} = k_i^{E_q} (P_{cref} - P_c) \quad (2.32)$$

where  $P_{cref} = P_{cref}^0 + k_{droop} V_{dc}$ .

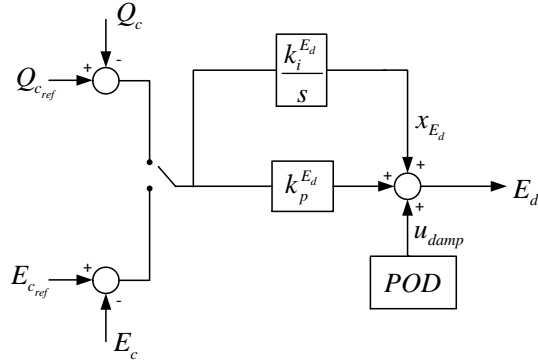


Figure 2.9: Reactive power/AC voltage controller.

On the other hand, based on the controller structure in Fig. 2.9 and assuming reactive power control, the controller equations are given as:

$$E_d = k_p^{E_d} (Q_{cref} - Q_c) + x_{E_d} + u_{damp} \quad (2.33)$$

$$\dot{x}_{E_d} = k_i^{E_d} (Q_{cref} - Q_c) \quad (2.34)$$

where  $k_p^{E_d}$  and  $k_i^{E_d}$  are the proportional and integral gains of the reactive power controller, respectively, and  $x_{E_d}$  is the state variable of the controller. It is worth noting that the coupling between active power with  $E_q$ , as well as the reactive power with  $E_d$  is conducted by the Phase Locked Loop (PLL) setting selection, such that the  $q$  and  $d$  voltage components are responsible for the independent control of active and reactive power, respectively. However the modeling of PLL dynamics is beyond the scope of this work.

Based on the given LCC and VSC controller models, the vector of states for converter controllers is given as:

$$x_{control} = \left[ x_{\alpha_1} \quad \dots \quad x_{\alpha_{n_{LCC}}} \quad x_{E_{d_1}} \quad \dots \quad x_{E_{d_{n_{VSC}}}} \quad x_{E_{q_1}} \quad \dots \quad x_{E_{q_{n_{VSC}}}} \right]^T \quad (2.35)$$

where  $n_{LCC}$  and  $n_{VSC}$  are the numbers of LCC and VSC in the MTDC network, respectively, with  $n_{LCC} + n_{VSC} = n_c$  with  $n_c$  being the total number of converters in the system.

## 2.5 DC line model

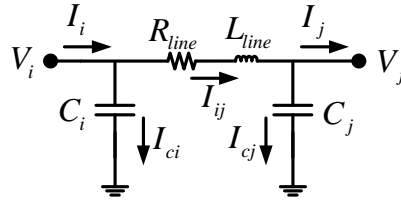


Figure 2.10: DC line model

The DC line is represented by its  $\pi$  equivalent model, as shown in Fig. 2.10. Based on the figure, the state equation of DC line current can be given as follows:

$$\dot{I}_{ij} = \frac{1}{L_{line}} (V_i - I_{ij} R_{line} - V_j) \quad (2.36)$$

where  $L_{line}$  and  $R_{line}$  are the line inductance and line resistance, respectively.  $V_i$  and  $V_j$  are the DC voltage at the two ends of the line. The state equations for DC voltages at the line ends are given as follows:

$$\dot{V}_i = \frac{1}{C_i} (I_i - I_{ij}) \quad (2.37)$$

$$\dot{V}_j = \frac{1}{C_j} (I_{ij} - I_j) \quad (2.38)$$

where  $C_i = C_j = \frac{C_{line}}{2}$ , and  $C_{line}$  is the line capacitance. Hence, the vector of DC state variables is given as:

$$x_{DC} = \left[ I_1 \quad \dots \quad I_{n_{lines}} \quad x_{LCC} \quad V_1 \quad \dots \quad V_{n_c} \right]^T \quad (2.39)$$

where  $n_{lines}$  and  $n_c$  are the number of DC lines and and converter nodes in the MTDC network, respectively.

## AC/DC system algebraic equations

### 2.6 Static load model

A variety of load models can be found in the literature, with the static load model being commonly used in stability studies [88] to represent the voltage dependency of loads. In this model, the active  $P_{L_i}$  and reactive  $Q_{L_i}$  load power at bus  $i$  are given as:

$$P_{L_i} = P_{L_{0_i}} \left( \frac{U_i}{U_0} \right)^{m_p} \quad (2.40)$$

$$Q_{L_i} = Q_{L_{0_i}} \left( \frac{U_i}{U_0} \right)^{m_q} \quad (2.41)$$

where  $P_{L_{0_i}}$  and  $Q_{L_{0_i}}$  are the nominal active and reactive powers of the load at the nominal voltage,  $U_i$  is the actual bus voltage, while  $U_0$  is the nominal bus voltage,  $m_p$  and  $m_q$  represent the exponential load model, where  $m_p = m_q = 0$  for constant power loads,  $m_p = m_q = 1$  for constant current load, and  $m_p = m_q = 2$  for constant impedance load [16, 60].

### 2.7 Algebraic mismatch equations

The algebraic variables at each AC system bus consist of the bus voltage magnitude ( $U$ ) and angle ( $\theta$ ). The vector of algebraic variables at bus  $i$  is given as:

$$y_i = \left[ U_i \quad \theta_i \right]^T \quad (2.42)$$

Hence, the vector of algebraic variables of the buses in Fig. 2.1 is given by:

$$y = \left[ U_1 \quad \dots \quad U_N \quad \theta_1 \quad \dots \quad \theta_N \right]^T \quad (2.43)$$

where  $N$  is the total number of buses in the system. As the AC system in Fig. 2.1 is assumed lossless, the bus admittance matrix ( $Y_{bus}$ ) is given by:

$$Y_{bus} = \begin{bmatrix} \bar{y}_{11} & \dots & \bar{y}_{1N} \\ \cdot & \dots & \\ \cdot & \dots & \\ \cdot & \dots & \\ \bar{y}_{N1} & \dots & \bar{y}_{NN} \end{bmatrix} \quad (2.44)$$

where  $Y_{bus} = G_{bus} + jB_{bus}$ . As the AC system is assumed lossless, hence  $G_{bus} = 0$  and  $Y_{bus} = jB_{bus}$ .

The algebraic equations are based on the active and reactive power mismatch equations at the AC system buses. The power mismatch equations are given as:

- Generator bus: ( $i = 1, \dots, n_g$ )

$$0 = P_{Gi} + P_{Li} + \sum_{j=1}^N B_{ij} U_i U_j \sin(\theta_i - \theta_j) \quad (2.45)$$

$$0 = Q_{Gi} + Q_{Li} - \sum_{j=1}^N B_{ij} U_i U_j \cos(\theta_i - \theta_j) \quad (2.46)$$

where  $P_{Gi} = \frac{U_i E'_{qi}}{x_{di}} \sin(\theta_i - \delta_i)$  and  $Q_{Gi} = \frac{U_i^2}{x_{di}} - \frac{U_i E'_{qi}}{x_{di}} \cos(\theta_i - \delta_i)$  are the active and reactive power of the generator, respectively.

- Load bus: based on the exponential load model given in the previous section, the power mismatch equations are given as: ( $i = n_g + 1, \dots, n_g + n_l$ )

$$0 = P_{Li} + \sum_{j=1}^N B_{ij} U_i U_j \sin(\theta_i - \theta_j) \quad (2.47)$$

$$0 = Q_{Li} - \sum_{j=1}^N B_{ij} (U_i U_j \cos(\theta_i - \theta_j)) \quad (2.48)$$

- LCC buses: the LCC was represented as a constant load power for the purpose of AC load flow. That is, the LCC converter buses were treated as PQ buses. The power mismatch equations are given as: ( $i = n_g + n_l + 1, \dots, n_g + n_l + n_{LCC}$ )

$$0 = P_{LCCi} + P_{Li} + \sum_{j=1}^N B_{ij} U_i U_j \sin(\theta_i - \theta_j) \quad (2.49)$$

$$0 = Q_{LCCi} + Q_{Li} - \sum_{j=1}^N B_{ij} (U_i U_j \cos(\theta_i - \theta_j)) \quad (2.50)$$

where  $P_{LCCi}$  and  $Q_{LCCi}$  are the active and reactive power of the LCC, respectively. The reactive power at the LCC was calculated as a percentage of its active power:  $Q_{LCCi} = k_{Q_{LCCi}} P_{LCCi}$  [16], where  $k_{Q_{LCCi}}$  is the amount of reactive power consumption in proportion to the active power. A typical range for  $k_{Q_{LCCi}}$  is from 40% to 50% [33].

- VSC buses: the VSC was also represented as a constant load power for the purpose of AC load flow. That is, the VSC converter buses were treated as PQ buses. The power mismatch equations at VSC buses are given as: ( $i = n_g + n_l + n_{LCC} + 1, \dots, N$ )

$$0 = P_{VSCi} + P_{Li} + \sum_{j=1}^N B_{ij} U_i U_j \sin(\theta_i - \theta_j) \quad (2.51)$$

$$0 = Q_{VSCi} + Q_{Li} - \sum_{j=1}^N B_{ij} (U_i U_j \cos(\theta_i - \theta_j)) \quad (2.52)$$

where  $P_{VSCi} = \frac{U_i E_c}{x_i} \sin(\theta_i - \gamma_c)$  and  $Q_{VSCi} = \frac{U_i^2}{x_i} - \frac{U_i E_c}{x_i} \cos(\theta_i - \gamma_c)$  are the active and reactive power of the VSC, respectively.

## 2.8 Combined AC/DC DAE power system model

As previously given, based on equations (2.1)-(2.4), (2.12)-(2.14), (2.17), (2.22), (2.28), (2.30), (2.32), (2.34), (2.36)-(2.38), and (2.45)-(2.52), the generalized power system in Fig. 2.1 can be described as:

$$\dot{x} = f(x,y) \quad (2.53)$$

$$0 = g(x,y) \quad (2.54)$$

where  $x = \begin{bmatrix} x_{AC} & x_{DC} & x_{control} \end{bmatrix}^T$  is the vector of dynamic state variables, that is subdivided into three vectors containing the states of the system generators ( $x_{AC}$ ), the states of the DC network ( $x_{DC}$ ), and the states of the converter controllers ( $x_{control}$ ). On the other hand,  $y = \begin{bmatrix} U_1 & \dots & U_N & \theta_1 & \dots & \theta_N \end{bmatrix}^T$  is the vector of algebraic variables in the system.



## Chapter 3

# POD Control through a Hybrid MTDC Network

### 3.1 Foreword

The study of power system stability includes a multitude of methods for the analysis of the system. The choice of the category of stability study is dependent both on the type of disturbance, as well as the size of the system. The main categories of the methods used for power system stability studies are given as follows [16, 22, 23]:

- **Small Signal Stability Analysis (SSSA) method:** the SSSA is concerned with small perturbations taking place around the power system's operating point. A small-signal model of the power system might be produced either through the linearization of the original nonlinear system model, or through system identification. Based on the small-signal model, the stability of the system is evaluated, and modal analysis can be conducted to identify the participating elements to the oscillatory modes. The results of SSSA are used to identify oscillatory modes with a low damping, which are likely to cause system instability in case of disturbances. The SSSA is also used for tuning Power System Stabilizers (PSSs) and Power Oscillation Damping (POD) controllers [22, 23].
- **Transient Energy Function (TEF) method:** this method gives an estimate of the stability region in case of faults, and is used for transient stability studies. The method is based on Lyapunov's second method. Despite having the advantage of providing a stability index, the TEF method suffers from

high complexity in case of using detailed models of the system components (such as high order generator models) [24].

- **Time-domain simulation method:** this method is used for both dynamic and transient stability studies. The method can also be used to corroborate the stability evaluation obtained from SSSA. The major advantage offered by this method is the ability to use detailed models of the power system components; however the method does not provide an insight into the system's stability margin. Moreover, the simulation becomes increasingly time-consuming as the size of the system gets larger [16, 24].
- **Single Machine Equivalent (SIME) method:** this method reduces the power system generators into two groups of machines: critical and non-critical machines. Then, the transient stability of both groups is evaluated through the Equal Area Criterion (EAC). Hence, the SIME method is capable of identifying the stability margin in the form of Critical Clearing Time (CCT), as well as the critical machines. Although the SIME method does not suffer from the complexity of TEF method, it does not present a sensitivity analysis of the system's parameters on the transient stability [24, 25].

In this chapter, the SSSA of the combined AC/DC power system is presented. Next, the small signal analysis is applied to a test power system with a hybrid MTDC network. The results of SSSA of the system are corroborated through time-domain simulations.

## 3.2 Small signal analysis of power system model

### Modal analysis

As previously given in Chapter 2, the dynamics of the multi-machine AC/DC power system can be described by:

$$\dot{x} = f(x, y, u) \quad (3.1)$$

$$0 = g(x, y, u) \quad (3.2)$$

where  $x$  is the vector of state variables of order  $n_x \times 1$ ,  $y$  is the vector of algebraic variables of order  $n_y \times 1$ , and  $u$  is the vector of input variables of order  $n_u \times 1$ . The system is assumed to operate at the equilibrium point  $(x_0, y_0, u_0)$ , which is the

initial operating condition of the system before a disturbance takes place. For small disturbances around the equilibrium point, the the system can be linearized around the equilibrium point  $((x_0, y_0, u_0))$  as follows:

$$\Delta \dot{x} = f_x \Delta x + f_y \Delta y + f_u \Delta u \quad (3.3)$$

$$0 = g_x \Delta x + g_y \Delta y + g_u \Delta u \quad (3.4)$$

where the Jacobian matrices are calculated at  $(x = x_0, y = y_0, u = u_0)$  as:

$$f_x = \left[ \frac{\partial f}{\partial x} \right] \quad f_y = \left[ \frac{\partial f}{\partial y} \right] \quad f_u = \left[ \frac{\partial f}{\partial u} \right] \quad (3.5)$$

$$g_x = \left[ \frac{\partial g}{\partial x} \right] \quad g_y = \left[ \frac{\partial g}{\partial y} \right] \quad g_u = \left[ \frac{\partial g}{\partial u} \right] \quad (3.6)$$

From (3.4),  $\Delta y$  can be written as:

$$\Delta y = -g_y^{-1}(g_x \Delta x + g_u \Delta u) \quad (3.7)$$

substituting (3.7) in (3.3), the dynamic of the linearized system is given as:

$$\begin{aligned} \Delta \dot{x} &= [f_x - f_y g_y^{-1} g_x] \Delta x + [f_u - f_y g_y^{-1} g_u] \Delta u \\ &= A \Delta x + B \Delta u \end{aligned} \quad (3.8)$$

where  $A$  is the system matrix of order  $n_x \times n_x$ , and  $B$  is the input matrix of order  $n_x \times n_u$ .

The output functions of interest are written in terms of state and algebraic variables as:

$$\mathcal{Y} = h(x, y, u) \quad (3.9)$$

where  $h$  is of order  $n_o \times 1$ . The output  $\mathcal{Y}$  is linearized around the equilibrium point as:

$$\Delta \mathcal{Y} = h_x \Delta x + h_y \Delta y + h_u \Delta u \quad (3.10)$$

substituting (3.7) in (3.10), the linearized output is given as:

$$\begin{aligned}\Delta \mathcal{Y} &= [h_x - h_y g_y^{-1} g_x] \Delta x + D \Delta u \\ &= C \Delta x + D \Delta u\end{aligned}\quad (3.11)$$

where  $C$  is the output matrix of order  $n_o \times n_x$ . Assuming  $D = 0$ , the linearized power system model is given as:

$$\begin{aligned}\Delta \dot{x} &= A \Delta x + B \Delta u \\ \Delta \mathcal{Y} &= C \Delta x\end{aligned}\quad (3.12)$$

Assuming  $\Delta u = 0$ , the unforced system is given by:

$$\Delta \dot{x} = A \Delta x \quad (3.13)$$

### Eigenvalues of linearized system model

The eigenvalues of system matrix  $A$  are defined as the  $n_x$  solutions of  $\lambda = \lambda_1, \dots, \lambda_{n_x}$  which satisfy:

$$\det(sI - A) = 0 \quad (3.14)$$

where  $I$  is the identity matrix. Each eigenvalue (real or complex) is associated with a mode of the system. The modes are found as:

$$\lambda_i = \sigma_i \pm j\omega_i \quad (3.15)$$

The eigenvalues carry information on the nature of existing modes in the system, with real eigenvalues corresponding to non-oscillatory modes, and complex eigenvalues corresponding to oscillatory modes resulting from local area oscillations between generators in the same zone, as well as inter-area oscillations between groups of generators in interconnected areas. Based on the oscillatory mode's value, the frequency ( $f_i$ ) and damping ( $\zeta_i$ ) of the mode can be found as:

$$\begin{aligned}f_i &= \frac{\omega_i}{2\pi} \\ \zeta_i &= \frac{-\sigma_i}{\sqrt{\sigma_i^2 + \omega_i^2}}\end{aligned}\quad (3.16)$$

A mode is defined as stable so long as it has a negative real part and it lies in the left half of the complex plane, as shown in Fig. 3.1. The damping of a mode also determines the decay rate of the oscillations.

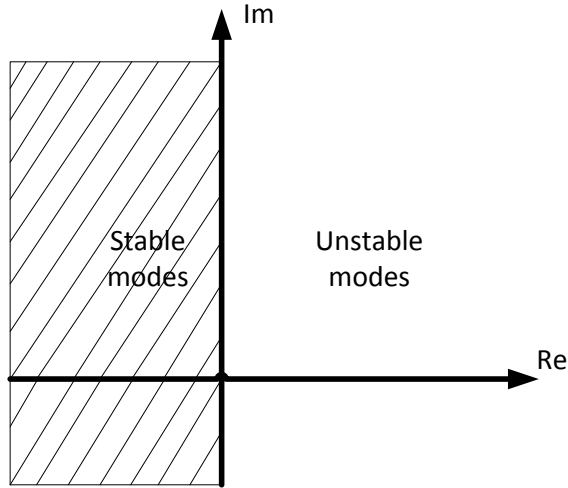


Figure 3.1: Locations of stable modes in complex plane.

### Eigenvectors

The right ( $V_i^r$ ) and left eigenvector ( $V_i^l$ ) of the matrix  $A$  corresponding to the eigenvalue  $\lambda_i$ , are defined as the non-zero vectors which satisfy the following:

$$\begin{aligned} AV_i^r &= \lambda_i V_i^r \\ V_i^l A &= \lambda_i V_i^l \end{aligned} \quad (3.17)$$

where  $V_i^r$  and  $V_i^l$  are of orders  $n_x \times 1$  and  $1 \times n_x$ , respectively. The normalized eigenvectors are given as:

$$V_i^l V_i^r = \begin{bmatrix} v_i^l & \dots & v_{i_{n_x}}^l \end{bmatrix} \begin{bmatrix} v_i^r & \dots & v_{i_{n_x}}^r \end{bmatrix}^T = 1 \quad (3.18)$$

Next, the right and left modal matrices can be defined as:

$$\begin{aligned} V^R &= \begin{bmatrix} V_1^r & V_2^r & \dots & V_{n_x}^r \end{bmatrix} \\ V^L &= \begin{bmatrix} (V_1^l)^T & (V_2^l)^T & \dots & (V_{n_x}^l)^T \end{bmatrix} \end{aligned} \quad (3.19)$$

### Participation factors

In order to measure the participation of state variables in a certain mode  $i$ , the participation matrix analysis is conducted. The right eigenvector  $V_i^r$  measures the activity of a state variable in the mode  $i$ , however the elements in the right eigenvector are dependent on the dimensions and scaling of the state. In order to produce a dimensionless gauge of states in a certain mode, the participation factor is defined as:

$$p_{ki} = v_{ik}^l v_{ki}^r = v_{ki}^r v_{ik}^l \quad (3.20)$$

As  $v_{ki}^r$  measures the activity of the state variable  $x_k$  in mode  $i$ , and  $v_{ik}^l$  measures the weight of this activity to the mode, the product  $p_{ki}$  measures the net participation. In small-signal analysis, the matrix  $P$ , which contains all participation factors, is defined as:

$$P = \begin{bmatrix} p_{11} & \dots & p_{n_x n_x} \\ \cdot & & \cdot \\ \cdot & & \cdot \\ \cdot & & \cdot \\ p_{n_x 1} & \dots & p_{n_x n_x} \end{bmatrix} \quad (3.21)$$

### Modal controllability and observability

The system matrix  $A$  in (3.12) normally takes a form of non-diagonal matrix, hence the dynamic of each state is a linear combination of other state variables. The analysis of parameters affecting the dynamic of each state variable is therefore a difficult task. In order to decouple the states from each other, the system in (3.13) is transformed by creating a new state vector as follows:

$$\xi = V^L \Delta x = (V^R)^{-1} \Delta x \quad (3.22)$$

substituting (3.22) in (3.13), the following system is obtained:

$$\begin{aligned} V^R \dot{\xi} &= A V^R \xi \\ \dot{\xi} &= (V^R)^{-1} A V^R \xi \\ &= \Lambda \xi \end{aligned} \quad (3.23)$$

where  $\Lambda$  is a diagonal matrix of order  $n_x \times n_x$  that has diagonal elements of the system's eigenvalues. Hence, the new system in (3.23) represents  $n_x$  uncoupled first-order differential equations given by:

$$\dot{\xi}_i = \lambda_i \xi_i \quad (3.24)$$

for  $i = 1, \dots, n_x$ .

Applying the transformation in (3.22) to (3.12), the following system is obtained:

$$\dot{\xi} = \Lambda \xi + V^L B \Delta u \quad (3.25)$$

$$\Delta \mathcal{Y} = C V^R \xi \quad (3.26)$$

Writing (3.25) in the form of  $n_x$  uncoupled equations is given as:

$$\dot{\xi}_i = \lambda_i \xi_i + \sum_{j=1}^{n_u} V_i^l B_j \Delta u_j = \lambda_i \xi_i + \sum_{j=1}^{n_u} c_{ij} \Delta u_j \quad (3.27)$$

for  $i = 1, \dots, n_x$ , where  $n_u$  is the number of inputs in the linearized system,  $c_{ij} = V_i^l B_j$ ,  $V_i^l$  is the  $i^{\text{th}}$  row of  $V^L$ ,  $B_j$  is the  $j^{\text{th}}$  column of  $B$ , and  $\Delta u_j$  is the  $j^{\text{th}}$  element of  $\Delta u$ . In case  $c_{ij} = 0$ , then the input  $\Delta u_j$  has no effect on the  $i^{\text{th}}$  mode. Therefore the  $i^{\text{th}}$  mode is controllable if and only if there is any  $c_{ij} \neq 0$ . The matrix  $V^L B$  of order  $n_x \times n_u$  is termed the mode controllability matrix, whose element in the  $j^{\text{th}}$  row and  $i^{\text{th}}$  column is  $c_{ij}$ . By inspecting the mode controllability matrix, the controllable modes can be identified.

Similarly, the output equation in (3.26) can be written as:

$$\Delta \mathcal{Y} = \sum_{i=1}^{n_x} C_j V_i^r \xi_i = \sum_{j=1}^{n_x} o_{ji} \xi_i \quad (3.28)$$

for  $j = 1, \dots, n_o$ , where  $n_o$  is the number of outputs in the linearized system,  $o_{ji} = C_j V_i^r$ ,  $C_j$  is the  $j^{\text{th}}$  row of  $C$  and  $V_i^r$  is the  $i^{\text{th}}$  column of  $V^R$ . The mode can only be observed in the  $j^{\text{th}}$  output variable if and only if there is any  $o_{ji} \neq 0$ . The matrix  $CV^R$  of order  $n_o \times n_x$  is termed the mode observability matrix, whose element in the  $j^{\text{th}}$  row and  $i^{\text{th}}$  column is  $o_{ij}$ . By inspecting the mode observability matrix, the observable modes can be identified.

### Residues

Taking the Laplace transform of (3.25) and (3.26) gives the following:

$$\begin{aligned} \xi(s) &= (sI - \Lambda)^{-1} V^L B \Delta u(s) \\ \Delta \mathcal{Y}(s) &= CV^R (sI - \Lambda)^{-1} V^L B \Delta u(s) \end{aligned} \quad (3.29)$$

where  $s$  is the Laplace operator. In case of a SISO system, the transfer function of (3.12) can be expressed as:

$$G(s) = \frac{\Delta \mathcal{Y}(s)}{\Delta U(s)} = \sum_{i=1}^{n_x} \frac{R_i}{s - \lambda_i} \quad (3.30)$$

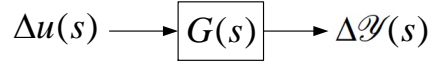
where  $R_i$  is the residue of  $G(s)$  at mode  $i$  ( $\lambda_i$ ), which is expressed as:

$$R_i = CV_i^r V_i^l B \quad (3.31)$$

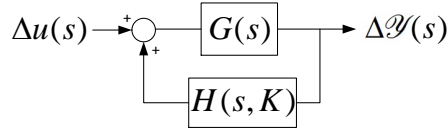
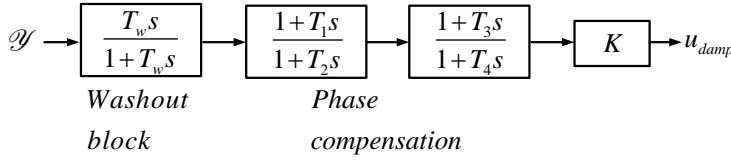
$R_i$  is of order  $n_o \times n_u$ . For a Single Input Single Output (SISO) linearized system ( $n_o = n_u = 1$ ),  $R_i$  is a scalar and equal to the product of controllability and observability of mode  $i$ .

### POD controller design

Assuming a SISO linearized system, the open loop system is shown in Fig. 3.2. On the other hand, the closed loop system is formed by adding the POD controller  $H(s, K)$ , as shown in Fig. 3.3.

Figure 3.2: Open loop system for the residue of the mode  $\lambda_i$ .

The controller structure of  $H(s, K)$  is shown in Fig. 3.4. The washout block stops contributions from steady state input deviations. On the other hand, the phase compensation blocks are lead-lag functions that shift the phase by tuning the values of  $T_1$ ,  $T_2$ ,  $T_3$  and  $T_4$ , so that a positive contribution to damping is obtained [27, 32], as shown in Fig. 3.5.  $K$  is the gain which determines the magnitude of damping provided by the POD controller.

Figure 3.3: Closed loop system for the residue of the mode  $\lambda_i$ .Figure 3.4: Controller configuration for  $H(s, K)$ .

The input signal to the controller is selected as to provide a positive contribution to the damping of the selected mode. The contribution is applied by adding the output of the POD controller to the primary controller output. The design equations for the lead-lag block are given as:

$$R_i = CV_i^r V_i^l B \quad \phi = 180 - \arg(R_i) \quad \alpha = \frac{1 + \sin(\phi)}{1 - \sin(\phi)} \quad (3.32)$$

Next, the values of parameters  $T_1$  and  $T_2$  are found as:

$$T = \frac{1}{\omega\sqrt{\alpha}} \quad T_1 = \alpha T \quad T_2 = T \quad (3.33)$$

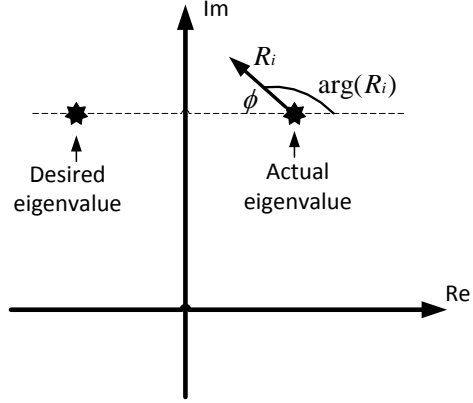


Figure 3.5: Displacement of mode using the feedback controller  $H(s, K)$ .

in case  $60 < \phi < 120$ :  $T_3 = T_1$ ,  $T_4 = T_2$ , otherwise  $T_3 = T_4$ , where  $\phi$  is the argument of the mode and  $\omega$  is the frequency of the mode,.

### 3.3 Hybrid MTDC network control

As a hybrid MTDC system involves both LCC and VSC converters, the primary control mode for each converter depends on the connected AC system connected to the converter [13, 14]. In case of active AC systems connected to both LCCs and VSCs, the DC voltage control can be assigned to a VSC converter, while the other VSCs operate in active and reactive power control mode. On the other hand, the LCC operate in active power control mode. In case of a passive AC grid connected to the VSC, the converter is operated to control both frequency and AC voltage. Should the AC grids connected to all the VSCs be passive, then the DC voltage control is assigned to the LCC. The converter control modes for the hybrid MTDC system are shown in Table 3.1. It is worth noting that the case of LCC connection to a passive AC grid was not considered, due to the impracticality of the LCC operation at a passive AC system that lacks an active voltage to support the converter commutation. Hence in a hybrid MTDC network, a LCC can only be utilized to connect to an active AC grid [13]- [15].

Similar to the point-to-point LCC-HVDC and VSC-HVDC links, the converters in a hybrid MTDC network can be used to effectuate POD control in the connected

Table 3.1: Primary control modes for LCCs and VSCs in a hybrid MTDC network.

	Active AC grid	Passive AC grid
LCC	Active power control	-
VSC	Active power, reactive power/AC voltage control	Frequency and AC voltage control

AC systems. Both LCC and VSC converters are capable of incorporating supplementary POD controllers in conjunction with their primary controllers, as previously shown in sections 2.3 and 2.4.

### 3.4 Test power system

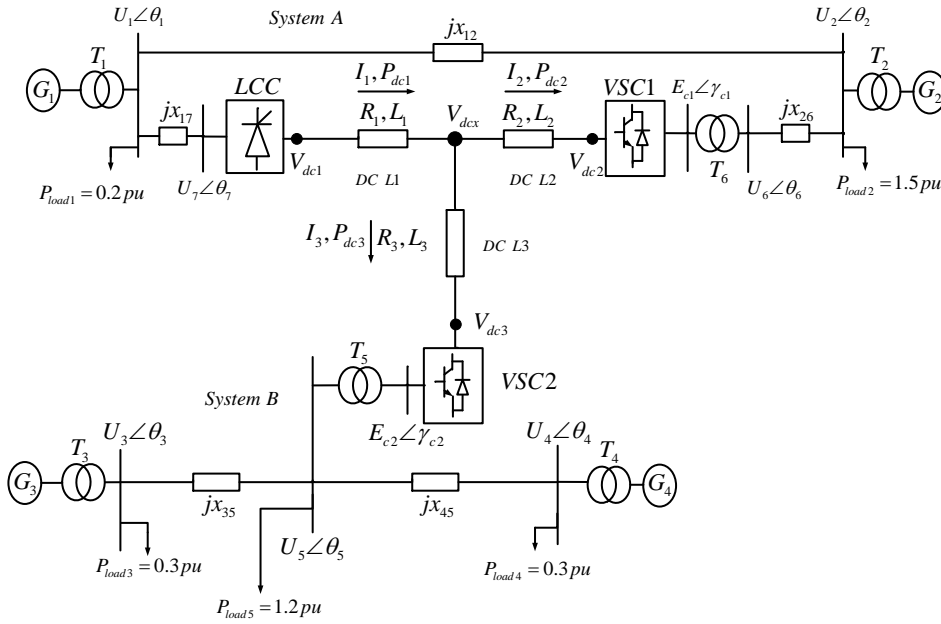


Figure 3.6: AC/DC power system with hybrid MTDC network

The test system is shown in Fig. 3.6. The system is described using DAEs as:

$$\begin{aligned} \dot{x} &= f(x, y, u) \\ 0 &= g(x, y, u) \end{aligned} \quad (3.34)$$

According to the components' models in Chapter 2, the state variables of the test system are given as:

$$x = \begin{bmatrix} x_{AC} & x_{DC} & x_{control} \end{bmatrix} \quad (3.35)$$

where  $x_{AC}$  is the vector of state variables for the AC system,  $x_{DC}$  is the vector of state variables for the DC system, while  $x_{control}$  is the vector of control state variables. The vectors are given as:

- AC system vector  $x_{AC}$  ( $i = 1, 2, 3, 4$ )

$$x_{AC_i} = \begin{bmatrix} \delta_i & \omega_i & E'_{qi} & E_{fdi} & S_{1i} & S_{2i} & S_{3i} \end{bmatrix} \quad (3.36)$$

$$x_{AC} = \begin{bmatrix} x_{AC_1} & x_{AC_2} & x_{AC_3} & x_{AC_4} \end{bmatrix}^T \quad (3.37)$$

- DC system vector  $x_{DC}$

As DC L1, connected between the LCC and the star point ( $V_{dcx}$ ), is a short line, the line is modeled as a resistance ( $R_1$ ) in series with an inductance ( $L_1$ ), while the capacitance of the line is neglected. Thus, the LCC current ( $I_{dc1}$ ) becomes equal to the line current ( $I_1$ ) in DC L1.  $x_{DC}$  is given by:

$$x_{DC} = \begin{bmatrix} I_1 & I_2 & I_3 & V_{dc2} & V_{dc3} & V_{dcx} \end{bmatrix}^T \quad (3.38)$$

- Control states vector  $x_{control}$

$$x_{control} = \begin{bmatrix} x_\alpha & x_{E_{d1}} & x_{E_{d2}} & x_{E_{q1}} & x_{E_{q2}} \end{bmatrix}^T \quad (3.39)$$

where  $x_\alpha$  is the state variable of DC current controller at the LCC,  $x_{E_{d1}}$  is the state variable of reactive power controller at VSC1,  $x_{E_{q1}}$  is the state variable for DC voltage controller at VSC1,  $x_{E_{d2}}$  is the state variable for the reactive power controller at VSC2, and  $x_{E_{q2}}$  is the state variable for the active power controller at VSC2.

On the other hand, the algebraic variables at each AC system bus consist of the bus voltage magnitude ( $U$ ) and angle ( $\theta$ ), as described in Section 2.7. The vector of algebraic variables is given as: ( $i = 1, 2, 3, 4, 5, 6, 7$ )

$$y_i = \begin{bmatrix} U_i & \theta_i \end{bmatrix} \quad (3.40)$$

$$y = \begin{bmatrix} U_1 & \dots & U_7 & \theta_1 & \dots & \theta_7 \end{bmatrix}^T \quad (3.41)$$

The total number of state variables in the combined AC/DC system is 39, while the total number of algebraic variables is 14. The equilibrium point of the DAE system in (3.34) is obtained through a two-step process explained as follows:

- First, an AC/DC load flow is conducted based on the unified method [46]. The converter power losses are neglected, with the DC power specified at each converter DC bus, except the DC slack bus (whose voltage is  $V_{dc2}$ ) where VSC1 is operated in DC voltage control mode. Both AC and DC power mismatch equations are solved simultaneously. The AC/DC load flow gives the initial values of the state variables in (3.38) and (3.39), as well as the algebraic variables in (3.41).
- Second, the obtained values of state and algebraic variables are used to calculate the initial values of the state variables in (3.36) (by substituting in their respective state equations). Hence, the equilibrium point  $(x_0, y_0, u_0)$  is obtained and used for the purpose of small-signal analysis of the power system.

### 3.5 SSSA results

The oscillatory modes in the combined AC/DC system are shown in Table 3.2. It could be observed that all eigenvalues have no positive real parts, indicating a stable operating point of the system. In the context of SSSA, a mode was considered to be adequately damped if its damping ratio is greater than or equal to 5% [27]. It could be noticed that the modes dominating the transient response of the system are  $\lambda_{1,2}$  and  $\lambda_{8,9}$ .

Table 3.2: Oscillatory modes in the combined AC/DC system.

$\lambda$	Mode	f (Hz)	$\zeta$
$\lambda_{1,2}$	$-0.2208 \pm j6.3045$	1.0034	0.0350
$\lambda_{4,5}$	$-3.5578 \pm j6.9908$	1.1126	0.4536
$\lambda_{6,7}$	$-1.9294 \pm j7.0349$	1.1196	0.2645
$\lambda_{8,9}$	$-0.7233 \pm j9.1620$	1.4582	0.0787
$\lambda_{11,12}$	$-4.6988 \pm j8.7973$	1.4001	0.4711
$\lambda_{13,14}$	$-3.1049 \pm j10.9244$	1.7387	0.2734
$\lambda_{19,20}$	$-4.8293 \pm j12.4481$	1.9812	0.3617
$\lambda_{25,26}$	$-3.6704 \pm j8.1006$	1.2893	0.4127
$\lambda_{31,32}$	$-2.9015 \pm j7.4491$	1.1856	0.3629

### Analysis of mode $\lambda_{1,2}$

In order to identify the contribution of the system's dynamic elements in the modes, the participation matrix analysis was conducted. The participation factors ( $p_i$ ) of the system states in the mode  $\lambda_{1,2}$  are shown in Table 3.3. The table shows that  $\lambda_{1,2}$  belongs to system A, with generator 2 being the largest contributor to the mode. The mode also shows a contribution from the control states of VSC1 in the form of participation factors of  $E_{d1}$ ,  $E_{q1}$ , and  $V_{dc2}$ . The contribution of these control states is affected by their respective controller gains, which also affects the contribution from  $V_{dc2}$ . The contributions of generators 3 and 4 to the mode are equal to zero, due to the interconnection of systems A and B through the MTDC network.

### Analysis of mode $\lambda_{8,9}$

The variation of damping of the mode  $\lambda_{8,9}$  against a range of the proportional gain for the DC voltage controller ( $K_p^{E_{q2}}$ ) is shown in Fig. 3.7. The increase of gain causes the mode  $\lambda_{8,9}$  to become unstable at a critical value of  $K_{p-critical}^{E_{q2}} = 2.35$ , hence the operating value of the gain should be kept below this critical value. The variation of  $K_{p-critical}^{E_{q2}}$  with the gains of PSS3 and PSS4 is shown in Fig. 3.8. The figure shows a reduction in the value of critical gain as the gains of PSS3 and PSS4 are increased. This comes as  $\lambda_{8,9}$  represents a control interaction between the DC voltage controller and the PSSs, which is found through the results of the participation matrix analysis in Table 3.5. The table shows that the contributors to

Table 3.3: Participation factors of the system states in  $\lambda_{1,2}$ .

	$P_i$
$\Delta\delta_1$	0.1032
$\Delta\delta_2$	0.5038
$\Delta\omega_1$	0.1032
$\Delta\omega_2$	0.5038
$\Delta E'_{q1}$	0.0031
$\Delta E_{q2}$	0.0085
$\Delta E_{fd1}$	0.0031
$\Delta E_{fd2}$	0.0085
$\Delta S_{11}$	0.0002
$\Delta S_{21}$	0.0001
$\Delta S_{31}$	0.0001
$\Delta S_{12}$	0.0005
$\Delta S_{22}$	0.0002
$\Delta S_{32}$	0.0002
$\Delta V_{dc2}$	0.0117
$\Delta E_{p1}$	0.0189
$\Delta E_{q1}$	0.0133

the mode are the state variables of the DC voltage controller  $x_{E_{q2}}$ , PSS1, and PSS2. Therefore the gains of PSS3 and PSS4 should not be increased (above the set-value of 0.3) in order to avoid the reduction of the critical gain value shown in Fig. 3.7.

Table 3.4: Variation of  $\lambda_{8,9}$ .

	$K_p^{E_{q2}} = 0.2$	$K_p^{E_{q2}} = 0.3$	$K_p^{E_{q2}} = 0.5$
$\lambda_{8,9}$	$-0.7233 \pm j9.1620$	$-0.5206 \pm j9.4673$	$-0.3679 \pm j9.8070$
$\zeta_{8,9}$	0.0787	0.0549	0.0374

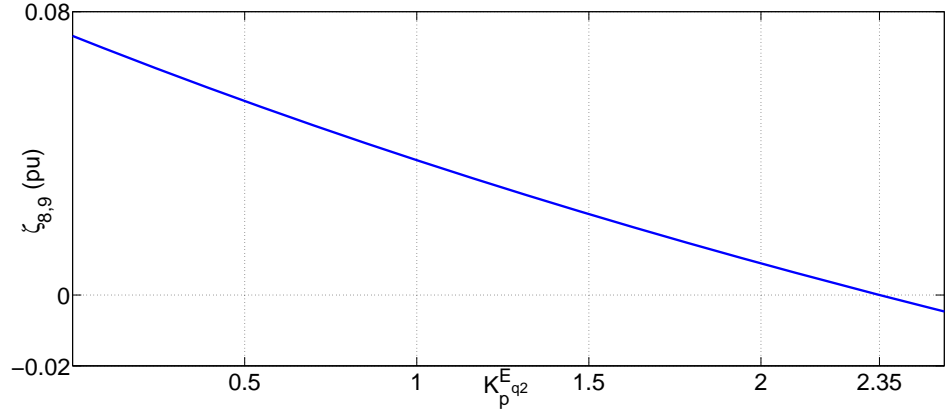


Figure 3.7: Effect of changing  $K_{p-critical}^{E_{q2}}$  on the damping of mode  $\lambda_{8,9}$ .

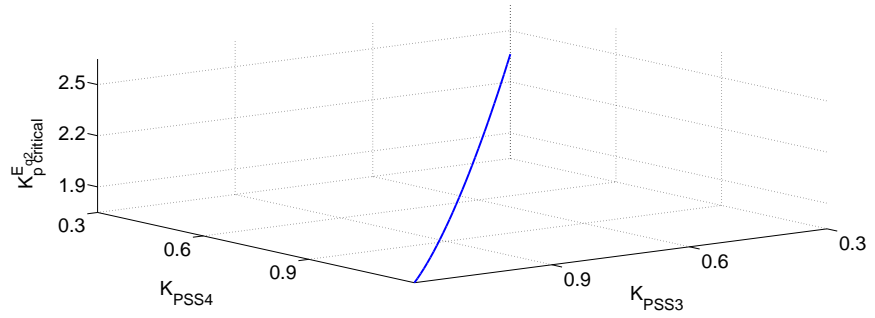


Figure 3.8: Effect of PSS gain variation on  $K_{p-critical}^{E_{q2}}$ .

### Impact of POD controller placement

In order to improve the damping in system A, a comparison of POD controller placement at the LCC and VSC1 is provided. The controller was tuned based on the residue method. the generator speed was used as the input signal for the controller. The resulting improvements in the damping of  $\lambda_{1,2}$  are shown in Table 3.6. The table shows a higher improvement in the mode damping in case of POD controller placement at VSC1 as compared to its placement at the LCC.

The modal controllability and observability of the mode  $\lambda_{1,2}$  were calculated as shown in Table 3.7. In case of controller placement at the LCC, the input is taken as the generator speed at  $G_1$ , while the output of the controller makes a contribution to

Table 3.5: Participation factors of controller states in  $\lambda_{8,9}$ .

	$P_i$
$\Delta S_{11}$	0.0107
$\Delta S_{21}$	0.0107
$\Delta S_{31}$	0.0107
$\Delta S_{12}$	0.0235
$\Delta S_{22}$	0.0235
$\Delta S_{32}$	0.0235
$\Delta V_{dc2}$	0.0127
$\Delta E_{p2}$	0.1160
$\Delta E_{q2}$	0.1160

the firing angle ( $\alpha$ ) at the LCC. On the other hand, in case of controller placement at VSC1, the input to the controller is the generator speed at  $G_2$ , while the output of the controller makes a contribution to the voltage component ( $E_{q1}$ ). Table 3.7 shows that the values of modal controllability and observability of  $\lambda_{1,2}$  are higher for the input and output signals of the POD controller at VSC1, as compared to the POD controller at the LCC. The higher values of modal controllability and observability indicate a larger magnitude of the mode residue at VSC1 as compared to the LCC, indicating an improved performance of the POD controller at VSC1, as compared to the controller placement at the LCC.

Table 3.6: Variation of  $\lambda_{1,2}$  with POD controller.

	No POD	POD at LCC	POD at VSC
$\lambda_{1,2}$	$-0.2208 \pm j6.3045$	$-0.5436 \pm j6.5592$	$-1.0047 \pm j6.6723$
$\zeta_{1,2}$	0.0306	0.0826	0.1489

Table 3.7: Modal controllability and observability of  $\lambda_{1,2}$  at LCC and VSC1.

	POD at LCC	POD at VSC1
Controllability	$2.516 \times 10^{-6}$	$3.802 \times 10^{-6}$
Observability	$6.7 \times 10^{-3}$	0.0323

### 3.6 Time-domain simulation results

The effect of increasing the proportional gain at the active power controller of VSC2 is investigated. The controller configuration is shown in Fig. 2.8 in Section 2.4. It has been found that in order to guarantee a damping that is greater than 5% for  $\lambda_{8,9}$ , the value of  $K_p^{Eq2}$  should be kept below 0.2. A disturbance of 10% decrease in PL5 was applied for 0.5 s at 10 s of simulation time. The effect of changing the controller gain is shown in Fig. 3.9. The figure shows that the increase of proportional gain results in the prolongation of the period of power oscillations over L35. The variation of  $\lambda_{8,9}$  with the change of proportional gain is also shown in Table 3.4. The value of the gain was selected at 0.2 in order to obtain an adequate value of damping for  $\lambda_{8,9}$ .

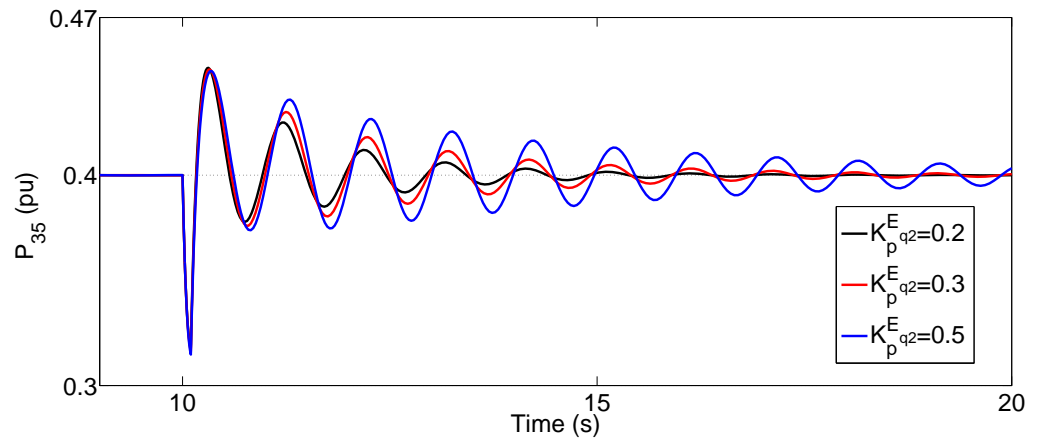


Figure 3.9: Effect of changing  $K_p^{Eq2}$ .

A three-phase fault was applied at 10 s of simulation time. The power over line L12 following fault clearing is shown in Fig. 3.10. It shows that the POD controller is capable of damping the power oscillations that followed the fault clearing. On the other hand, the power oscillations persist on the line for over 20 s after fault clearing in the absence of the POD controller. The impact of PSS gain variation is also shown in Fig. 3.10. It could be noticed that the increase of gain at PSS1 and PSS2 led to a reduction in the damping performance of the system. This is due to the faster action of the POD controller at VSC1 as compared to the damping provided

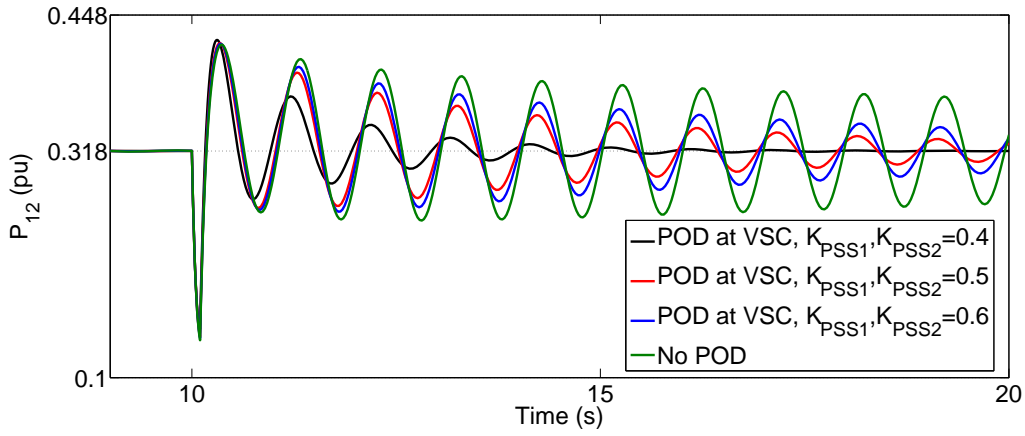


Figure 3.10: Power on L12 following fault clearing.

by PSS1 and PSS2. Thus, it could be concluded that the PSS gain at generators 1 and 2 should not be increased (above the set value of 0.4), in order to avoid the reduction in the damping provided by the POD controller.



## **Chapter 4**

# **Operating Point Adjustment Control through a VSC-MTDC Network**

### **4.1 Foreword**

The availability of multiple controllable elements in the power system has spurred research into system control through operating point adjustment. In this vein, the system's operating point can be adjusted by means of varying a set of controllable parameters, whose change results in the displacement of the system's operating point to a new one. The adjustment of the controllable parameters is usually conducted with the purpose of enhancing system stability against the backdrop of other freely changing parameters, whose variation may result in a deterioration of system stability, such as loads [29, 30]. As earlier power system operations lacked the means for global, system-wide data acquisition and measurements, the principle of operating point adjustment faced a practical difficulty in testing and implementation. Nevertheless, various strategies for operating point adjustment were developed based on the modal analysis of the power system [29]. The strategies considered elements of the power system to locate the controllable parameters, such as generators and capacitor banks. In case of generators, both AVR setpoint and redispatchable power were studied as the controllable parameters. On the other hand, variable reactive power compensation was considered as the controllable parameter in case of capacitor banks. The criterion, against which the operating point is adjusted, is based on the margin to oscillatory instability caused by Hopf

Bifurcation (HB), as detailed in the following sections of this chapter.

With the advent of Phasor Measurement Units (PMUs) that are capable of providing real time measurement of power system states, there has been an increasing interest in the utilization of modal analysis as a tool for real-time operation of power systems. Traditionally, PSS and POD controllers have been used to enhance the system stability by modulating the active power to induce a positive contribution to the damping in the system, in what is known as modulation control. Modulation control is effectuated in case of the occurrence of a disturbance to maintain the stability and security of the system. On the other hand, operating point adjustment control aims to alter the power system's operating point to avert the instability condition in the system. The modal analysis is used as a tool for evaluating the system's stability margin, which determines if a decision to adjust the operating point is made [57]. In a coordinated control scheme, a potential solution is to utilize the modulation control as a first line response against disturbances, while operating point adjustment controls can be used as a secondary choice to alter the system's operating point in the post-disturbance environment, with the purpose of reaching a more secure small-signal condition of the system [57].

## 4.2 Calculation of sensitivity to HB

Given the DAE system model:

$$\begin{bmatrix} \dot{x} \\ 0 \end{bmatrix} = \begin{bmatrix} f(x, y, \eta) \\ g(x, y, \eta) \end{bmatrix} = F(z, \eta) \quad (4.1)$$

where  $x \in R^{n_x}$ ,  $y \in R^{n_y}$  and  $\eta \in R^m$  are the vectors of state variables, algebraic variables, and parameters, respectively.  $f$  represents the differential equations of the system, while  $g$  represents the algebraic equations of the system,  $F = \begin{bmatrix} f^T & g^T \end{bmatrix}^T$ , while  $z = \begin{bmatrix} x & y \end{bmatrix}^T$ . The derivation of sensitivity given in this section largely follows [47]- [50]. The system parameters vector  $\eta = \begin{bmatrix} \mu & p \end{bmatrix}$  consists of uncontrollable parameters ( $\mu$ ) and controllable parameters ( $p$ ). The equilibrium point of the system is given by  $(z_0, \eta_0)$ , where  $z_0 = \begin{bmatrix} x_0 & y_0 \end{bmatrix}^T$  and  $\eta_0 = \begin{bmatrix} \mu_0 & p_0 \end{bmatrix}^T$  are the vectors of combined state and algebraic variables, and parameters at equilibrium, respectively. The eigenvalues are found from the linearized system matrix as follows:

$$A = f_x - f_y g_y^{-1} g_x \quad (4.2)$$

As the computation of  $A$  in (4.2) requires the inversion of  $g_y$ , the sparsity of  $g_y$  is destroyed. In order to preserve the sparsity of  $g_y$ , the eigenvalues are calculated using the "generalized" system matrix  $F_z$ , which is given as:

$$F_z = \begin{bmatrix} f_x & f_y \\ g_x & g_y \end{bmatrix} \quad (4.3)$$

The eigenvectors for the generalized system matrix are given by:

$$\begin{bmatrix} \Lambda e_1 \\ 0 \end{bmatrix} = \begin{bmatrix} f_x & f_y \\ g_x & g_y \end{bmatrix} \begin{bmatrix} e_1 \\ e_2 \end{bmatrix} = F_z \begin{bmatrix} e_1 \\ e_2 \end{bmatrix} = F_z e \quad (4.4)$$

where  $F_z$  is the Jacobian of  $F$  with respect to  $z$ ,  $e$  is the right eigenvector of  $F_z$ , and  $\Lambda$  is the vector of generalized eigenvalues.  $\mu_0$  represents the values of uncontrollable parameters at the original equilibrium point. HB takes place upon the variation of uncontrollable parameters above  $\mu_0$ , when a pair of complex eigenvalues reaches the imaginary axis and have a zero real part, as shown in Fig. 4.1. Beyond this point, the system is no longer small signal stable. At this point,  $\eta^* = [\mu^* \ p^*]^T$  are the values of parameters at the HB point.

In order to avoid small-signal instability, the stability margin  $M$ , defined as  $M = \mu^* - \mu_0$ , can be increased by adjusting the controllable parameters ( $p$ ) in response to the variation in  $\mu$ . The adjustment in  $p$  is conducted according to the first order sensitivity of  $M$  with respect to  $p$ . This process is explained as follows:

- At the point of HB,  $F_z$  is evaluated from the power flow solution, followed by the calculation of other dynamic variables to find the equilibrium point at the HB point  $(z_0^*, \eta^*)$ .
- The matrix  $u_\eta$  is found from the inverse of  $F_z$  to represent the system parameters at the equilibrium point  $(z_0^*, \eta^*)$ , where  $u_\eta : R^m \rightarrow R^{n_z}$ . The matrix  $u_\eta$  is found as, where  $F_\eta$  is the Jacobian of  $F$  with respect to  $\eta$ :

$$F_z u_\eta = -F_\eta \quad (4.5)$$

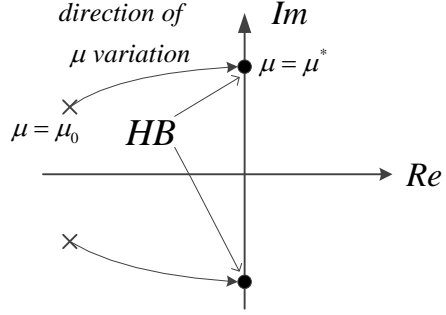


Figure 4.1: HB occurrence as shown in complex plane.

- The sensitivity of  $M$  with respect to  $p$  is a normal projection to  $\eta^*$ . The normal vector to  $\eta^*$  is calculated using the sensitivities of the eigenvalues real parts to  $p$  as:

$$N = Re\{d(F_{zz}^*u_\eta^* + F_{z\eta}^*)e\} \quad (4.6)$$

where  $F_{zz}$  is the Hessian (second partial derivative) of  $F_z$  with respect to  $z$ ,  $F_{z\eta}$  is the Hessian of  $F_z$  with respect to  $z$  and  $\eta$ ,  $d$  and  $e$  are the normalized extended left and right eigenvectors of  $F_z$  that correspond to the purely imaginary eigenvalue, with  $de = 1$  and  $|d| = 1$ .

- Considering the sensitivity vector:

$$N = \begin{bmatrix} n_\mu & n_{p_1} & n_{p_2} & \dots & n_{p_{m-1}} \end{bmatrix} \quad (4.7)$$

The sensitivity of the stability margin to the controllable parameters is given by:

$$N_{p|p_0} = -\frac{1}{n_\mu} \begin{bmatrix} n_{p_1} & n_{p_2} & \dots & n_{p_{m-1}} \end{bmatrix} \quad (4.8)$$

### 4.3 Setpoint adjustment in case of load changes

The control objective is to adjust the controller setpoints at the VSC-MTDC network converters in order to increase the HB stability margin of the power system. Therefore, the controllable parameters ( $p$ ) consist of the active and reactive power setpoints at VSC1, VSC2, and VSC3. The increase in stability margin results in an increased distance between the power system's operating point and HB, and consequently the minimum damping in the system is increased. The optimization formulation therefore aims to maximize the damping of the least damped mode in the system. The operating point of the system that achieves a maximum damping of the least damped mode is defined in terms of the following optimization problem:

$$\max_{P_{ref_i}, Q_{ref_i}} \zeta_{min}(x, y, \eta) \quad (4.9)$$

$$s.t. \quad g(x, y, \eta) = 0 \quad (4.10)$$

$$f(x, y, \eta) = 0 \quad (4.11)$$

$$P^{min}, Q^{min} \leq P_{ref_i}, Q_{ref_i} \leq P^{max}, Q^{max} \quad (4.12)$$

where

$$\zeta_{min} = \min_{j \in \{1, 2, \dots, n_x\}} \zeta_j \quad (4.13)$$

$$\eta = [\mu, P_{ref_i}, Q_{ref_i}] \quad (4.14)$$

where  $\zeta_{min}$  is the damping of least damped oscillatory mode obtained from (4.4). Thus, the adjustment of controller setpoints aims to maximize  $\zeta_{min}$ .  $P_{ref_i}$  and  $Q_{ref_i}$  are the active and reactive power setpoints at the  $i^{th}$  converter, respectively,  $n_{P_{ref_i}}$  and  $n_{Q_{ref_i}}$  are the sensitivities of stability margin to active and reactive power setpoints, respectively. The steady state of the system is ensured by the equality constraints in (4.10) and (4.11), while the converter power limits are ensured by the inequality constraint in (4.12), respectively. The inequality constraint in (4.12) guarantees that the output power of VSCs does not exceed its power rating, specified in MVA.

The optimization process is described by the flow chart in Fig. 4.2, where  $P_{ref_i}$  and  $Q_{ref_i}$  are the active and reactive powers setpoints at converter  $i$ , where  $i = 1, \dots, n_2$ .  $P_{ref_i}^0$  and  $Q_{ref_i}^0$  are the initial values of active and reactive power setpoints

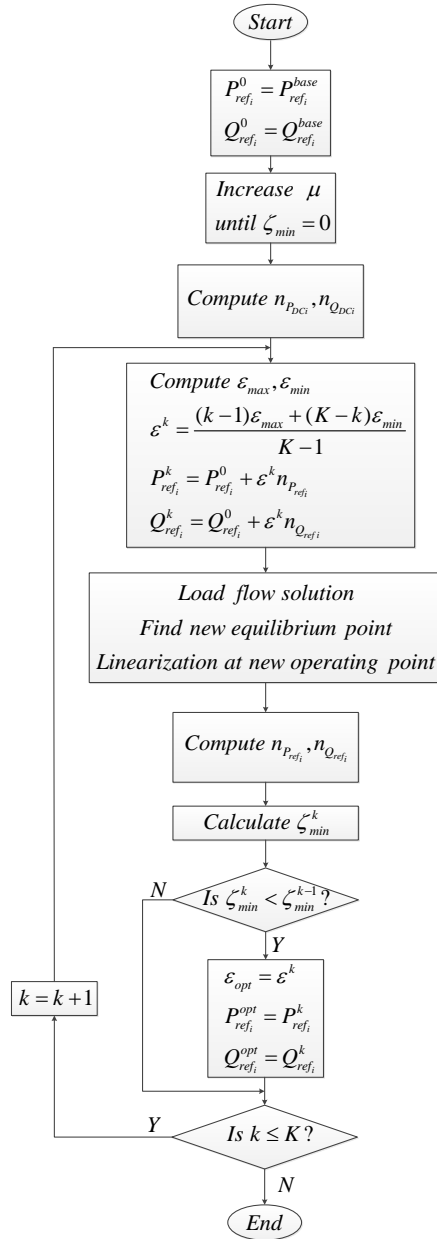


Figure 4.2: Flow chart for the calculation of optimized controller setpoints.

at converter  $i$ ,  $\varepsilon_{max}$  and  $\varepsilon_{min}$  are the maximum and minimum values of step size used to adjust the active and reactive power setpoints,  $K$  is the total number of points in the interval  $[\varepsilon_{min}, \varepsilon_{max}]$ , while  $k$  is the iteration number. The initial operating point of the power system is determined based on the AC/DC load flow. The selected uncontrollable parameter  $\mu$  (representing load increase) is varied until a HB is reached, when a zero damping is obtained for an eigenvalue. The sensitivity of the stability margin for the active and reactive power setpoints of the VSC controllers are calculated at the HB point. A line search [66] is then conducted to determine the optimum values of the active and reactive power setpoints. During the line search process, the generators' output powers are determined based on their governor droop constants [67]. Thus, the total change in generated power is distributed over all the generators, so as to represent the generation redispatch upon the setpoint adjustment at the VSCs. The new generators' output powers are then used in the linearization.

The adjustment of active and reactive power setpoints is formulated as follows:

$$P_{ref_i}(\varepsilon_{opt}) = P_{ref_i}^0 + \varepsilon_{opt} n P_{ref_i} \quad (4.15)$$

$$P_{ref_i}^{opt} = \begin{cases} P_{ref_i}^{min} & \text{if } P_{ref_i} < P_{ref_i}^{min} \\ P_{ref_i} & \text{if } P_{ref_i}^{min} \leq P_{ref_i} \leq P_{ref_i}^{max} \\ P_{ref_i}^{max} & \text{if } P_{ref_i} > P_{ref_i}^{max} \end{cases} \quad (4.16)$$

$$Q_{ref_i}(\varepsilon_{opt}) = Q_{ref_i}^0 + \varepsilon_{opt} n Q_{ref_i} \quad (4.17)$$

$$Q_{ref_i}^{opt} = \begin{cases} Q_{ref_i}^{min} & \text{if } Q_{ref_i} < Q_{ref_i}^{min} \\ Q_{ref_i} & \text{if } Q_{ref_i}^{min} \leq Q_{ref_i} \leq Q_{ref_i}^{max} \\ Q_{ref_i}^{max} & \text{if } Q_{ref_i} > Q_{ref_i}^{max} \end{cases} \quad (4.18)$$

where  $P_{ref_i}^0$  and  $Q_{ref_i}^0$  are the original values of setpoints for active and reactive power, respectively,  $\varepsilon_{opt}$  is the optimum step size. On the other hand, the minimum and maximum values of active power setpoint are  $P_{ref_i}^{min}$  and  $P_{ref_i}^{max}$ , respectively, while the minimum values of reactive power setpoint are  $Q_{ref_i}^{min}$  and  $Q_{ref_i}^{max}$ , respectively.

#### 4.4 Setpoint adjustment in case of faults

The setpoint adjustment in case of a fault is intended to enhance the transient stability through the reduction of inter-area power flow over AC interconnections, by diverting the power flow to the DC interconnections. A generalized transmission

scenario for both AC and DC interconnections between two areas is shown in Fig. 4.3. The tie lines selected for power flow reduction are those with large angle differences at their end buses, and are to be determined by the involved TSOs. As the MTDC network converters are capable of quickly changing their output powers, the power transferred over the MTDC network can be increased to reduce the power flow over the AC tie lines. The reduction in power flow over the AC tie lines is calculated using the Power Transfer Distribution Factors (PTDFs) [51] in case of a new post-fault power flow scenario that is defined a priori [51,52], by means of the adjusted VSCs output powers. The PTDFs are calculated based on the variation of bus voltage angles resulting from a changed power flow scenario.

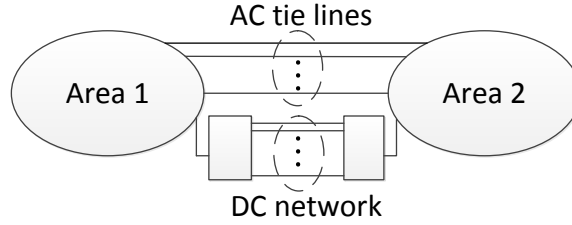


Figure 4.3: Inter-area AC and DC interconnections.

The PTDFs are calculated with the assumption of reduced power over the tie lines in order to minimize the power flow in the new power flow scenario. The PTDFs' calculation is derived from the power mismatch equations as follows [53]:

$$g_P(\theta, U) = 0 \quad (4.19)$$

$$g_Q(\theta, U) = 0 \quad (4.20)$$

where  $g_P$  and  $g_Q$  represent the active and reactive power power mismatch equations for the system, respectively, while  $\theta$  and  $U$  are the bus voltage angle and magnitude, respectively. In case of a small change around the operating point, the linearized equations of active and reactive power variations are given as:

$$\begin{bmatrix} \Delta P \\ \Delta Q \end{bmatrix} = \begin{bmatrix} \frac{\partial g_P(\theta, U)}{\partial \theta} & \frac{\partial g_P(\theta, U)}{\partial U} \\ \frac{\partial g_Q(\theta, U)}{\partial \theta} & \frac{\partial g_Q(\theta, U)}{\partial U} \end{bmatrix} \begin{bmatrix} \Delta \theta \\ \Delta U \end{bmatrix} = J \begin{bmatrix} \Delta \theta \\ \Delta U \end{bmatrix} \quad (4.21)$$

where  $J = \begin{bmatrix} \frac{\partial g_P(\theta, U)}{\partial \theta} & \frac{\partial g_P(\theta, U)}{\partial U} \\ \frac{\partial g_Q(\theta, U)}{\partial \theta} & \frac{\partial g_Q(\theta, U)}{\partial U} \end{bmatrix}$  is the Jacobian matrix with partial derivatives of

(4.19) and (4.20). The changes in bus voltage and angle can therefore be obtained as:

$$\begin{bmatrix} \Delta\theta \\ \Delta U \end{bmatrix} = \begin{bmatrix} \frac{\partial g_P(\theta,U)}{\partial\theta} & \frac{\partial g_P(\theta,U)}{\partial U} \\ \frac{\partial g_Q(\theta,U)}{\partial\theta} & \frac{\partial g_Q(\theta,U)}{\partial U} \end{bmatrix}^{-1} \begin{bmatrix} \Delta P \\ \Delta Q \end{bmatrix} = \begin{bmatrix} J'_{11} & J'_{12} \\ J'_{21} & J'_{22} \end{bmatrix} \begin{bmatrix} \Delta P \\ \Delta Q \end{bmatrix} = \begin{bmatrix} J'_{11}\Delta P + J'_{12}\Delta Q \\ J'_{21}\Delta P + J'_{22}\Delta Q \end{bmatrix}$$

The PTDF in the line between buses  $i$  and  $j$  is calculated as:

$$PTDF_{ij} = \Delta P_{ij} = \psi_{ij} = \frac{\Delta\theta_i - \Delta\theta_j}{x_{ij}} \quad (4.22)$$

where  $x_{ij}$  is the reactance of the line between buses  $i$  and  $j$ . Under the assumption of fixed network configuration (i.e. without line tripping), the adjustment of active power setpoints in MTDC network converters is calculated based on the reduced power flow over the AC tie lines, in such a way to keep the total amount of inter-area power transfer (over both the AC and DC ties) fixed at the pre-fault level. Assuming a total number of  $n_2$  converters in the system, with  $\Omega_{dc}$  converters injecting active power into the receiving area (i.e. operating in inverter mode), such that  $\Omega_{dc} \in n_2$ , the adjustment of active power aims to minimize the 2-norm of PTDFs relevant to the tie lines as follows:

$$\min_{P_{refi}} \sum_{i \in \Omega_{dc}} \psi_{k-l}^2 \quad (4.23)$$

$$s.t. \quad f(x, y, \eta) = 0 \quad (4.24)$$

$$g(x, y, \eta) = 0 \quad (4.25)$$

$$P_{refi} \leq P_{refi}^{max} \quad (4.26)$$

where  $\psi_{k-l}$  represent the PTDFs of the tie lines interconnecting the two areas of the power system,  $P_{refi}$  represent the adjusted setpoints of the MTDC converters, and  $P_{refi}^{max}$  is the converter's maximum value of active power setpoint set by the converter's rating.

## 4.5 Test power system

Table 4.1: VSC control modes in the MTDC network.

VSC1	DC voltage control	Reactive power control
VSC2	Active power control	Reactive power control
VSC3	Active power control	Reactive power control

The study system consists of two IEEE 14-bus sections interconnected by a long AC tie line, together with an embedded VSC-MTDC network, as shown in Fig. 4.4. The converter buses are connected to buses 9 in section A, and buses 18 and 22 in section B, respectively. The generators in each section are represented by one-axis model with IEEE Type-I exciter and TGOV1 governor. The AC system data are given in [17]. The total number of state variables in the combined AC/DC system is 93, which are categorized as:

$$x = \begin{bmatrix} x_{AC} & x_{DC} & x_{control} \end{bmatrix} \quad (4.27)$$

where the lengths of vectors  $x_{AC}$ ,  $x_{DC}$ , and  $x_{control}$  are 80, 7, and 6, respectively. On the other hand, the total number of algebraic variables ( $y$ ) is 62. The control modes for VSC1, VSC2, and VSC3 are given in Table 4.1.

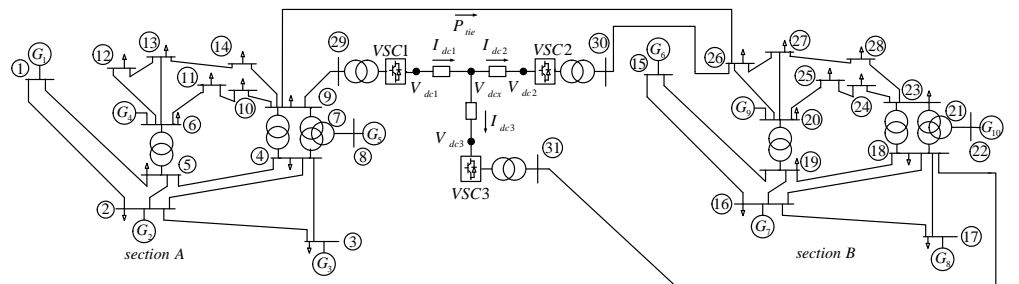


Figure 4.4: Test system with embedded VSC-MTDC.

## 4.6 Time-domain simulation results

### Load change results

A disturbance of 25% increase (14 MW) in load power at bus 23 is applied for 0.1 s. The variation of power flow over the tie line is shown in Fig. 4.5. The figure shows poorly damped inter-area power oscillations in case of fixed setpoints at the MTDC converters. On the other hand, the setpoint adjustment was capable of damping the power oscillations by reducing the power flow over the tie line. Instead, the increase in load power is supplied through VSC2 and VSC3. The figure also shows the variation of power flow over the tie line in case of droop control applied to DC voltage regulation in the MTDC network. The figure also shows a difference in power in case of different DC voltage control strategies, as in case of droop control the injected power is affected by the DC voltage changes that take place at the converter stations where active power setpoint adjustment is conducted.

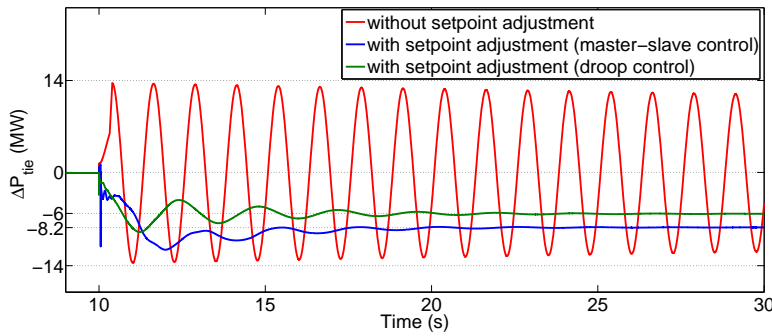


Figure 4.5: Variation of power flow over the tie line following a 25% load power increase at bus 23 applied for 0.1 s.

The inter-area oscillations are also shown through the phase portraits between the Single Machine Equivalent (SIME) rotor angle ( $\delta_{SIME}$ ) and speed ( $\omega_{SIME}$ ) [4, 8], where  $\delta_{SIME}$  and  $\omega_{SIME}$  are defined between the groups of generators in sections A and B, respectively. The phase portraits show the variations in  $\delta_{SIME}$  and  $\omega_{SIME}$ , with the origin being the equilibrium point representing the original operating point of the system. The phase portrait in Fig. 4.6 shows persisting oscillations in  $\delta_{SIME}$  following the disturbance in case of fixed setpoints at the MTDC converters. On the other hand, Fig. 4.7 shows a departure from the original operating point to the new operating point in case of setpoint adjustment, with adequate damping of the oscillations in  $\delta_{SIME}$  as a result of the adjustment in the operating point of the

system.

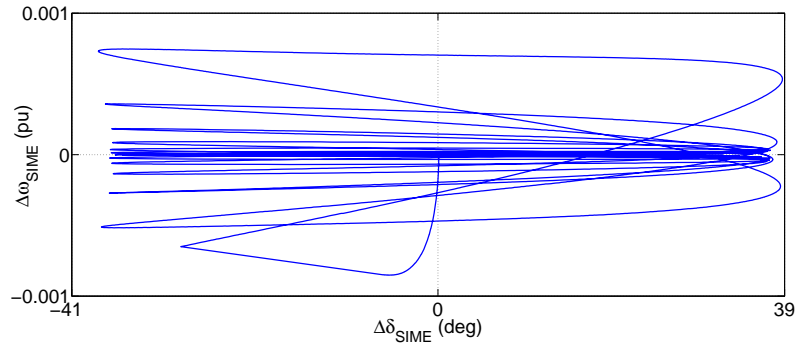


Figure 4.6:  $\delta_{SIME}$ - $\omega_{SIME}$  phase portrait without operating point adjustment.

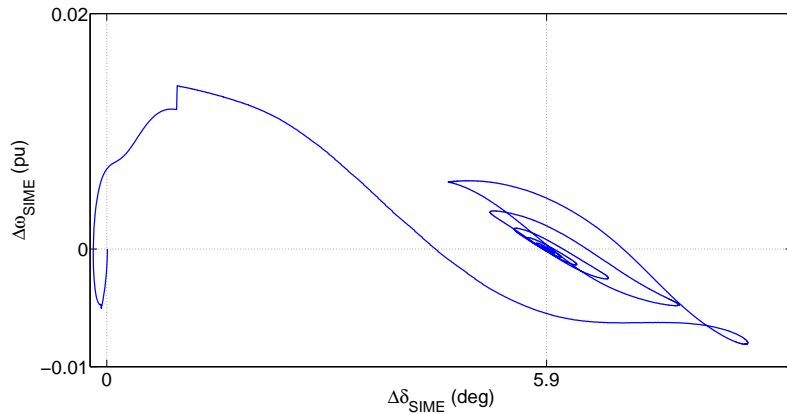


Figure 4.7:  $\delta_{SIME}$ - $\omega_{SIME}$  phase portrait with operating point adjustment.

A comparison between the performances of POD and operating point adjustment is shown in Fig. 4.8. The figure shows the basic difference between both techniques. The POD control is focused on increasing the damping ratio at the same operating point through the deployment of supplementary controllers (such as PSSs and POD controllers). On the other hand, the operating point adjustment control transfers the system to a new operating point in order to mitigate the poorly damped oscillations at the original one. In this context, the POD control can be set to operate as the first line of action against disturbances, as its operation is fully automated and incorporated within the main control framework (i.e. does not depend on operator

action). On the other hand, the operating point adjustment control can be used as a secondary control mechanism, since its initiation and decision making is largely dependent on the system operator. Although the work covered here did not include the coordination between POD control and operating point adjustment, a discussion on this coordination was given in [70].

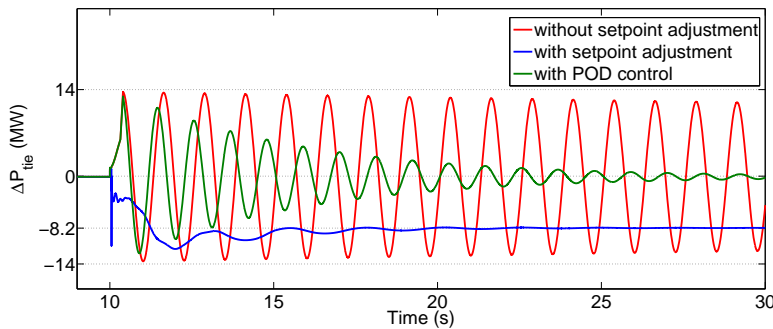


Figure 4.8: POD control as compared to operating point adjustment.

**Short circuit fault results**

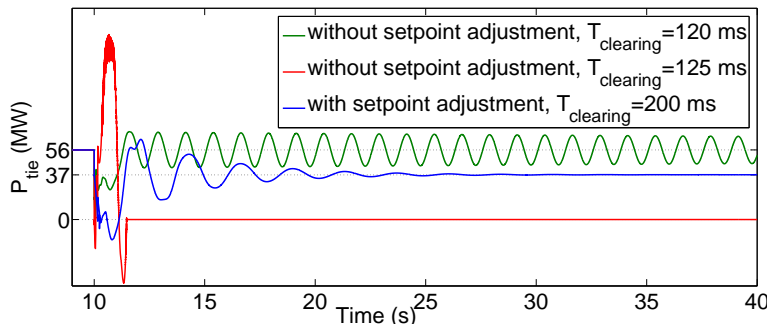


Figure 4.9: Power flow over the tie line following short circuit at bus 7.

In this section, the impact of a short circuit fault at bus 7 is evaluated. The stability improvement is evaluated by studying the impact of setpoint adjustment on the fault Critical Clearing Time (CCT). The power flow over the AC tie line is shown in Fig. 4.9, the figure shows prolonged power oscillations over the line in case of a clearing time of 120 ms, which corresponds to the value of CCT. In case of

a clearing time that is greater than the CCT, the tie line is tripped as a result of non-oscillatory angle instability taking place in the system and forcing the separation of its sections. On the other hand, the figure shows that setpoint adjustment is capable of increasing the CCT from 120 ms to 200 ms, while maintaining the power flow over the tie line at a lower value. The resulting enhancement in damping is due to the power flow rerouting through the MTDC network from section A to section B and the subsequent decrease in power flow over the tie line. It is worth noting that the setpoint adjustment is assumed to take place simultaneously with fault clearing, thereby allowing to use the fault clearing time as a communication latency that is needed for delivering the control signals to the converter stations. The VSCs were assumed capable of withstanding the low voltages in the AC network during the fault, as stipulated in the European Network for Transmission System Operators for Electricity (ENTSO-E) grid code for Fault Ride Through (FRT) [69].

## **Chapter 5**

# **Design of a MISO POD Controller in a VSC-MTDC Network**

### **5.1 Foreword**

As the size and complexity of power systems continue to increase due to system interconnections and increasing share of renewable energy sources, inter-area and cross-border flows of bulk power are becoming a commonplace in system operation [74, 75]. Although power system interconnections are a benefit to the system from an economic and reliability points of view, the result is an increased stress level in system operation [76]. As an increased stress level means that the system is operated closer to its stability limits, this can easily give rise to stability problems that threaten the secure operation of the system. Inter-area oscillations has been one of the major stability problem in large interconnected power systems [74]- [76], as it has led to multiple incidents of blackouts that affected large parts of the interconnected power systems [74].

Along with local area oscillations, inter-area oscillations have traditionally been damped using PSSs, which receive local signals (such as generator speed), and contribute with a supplementary input to the generator's AVR to include the required phase compensation. Nevertheless, the observability of inter-area modes in local signals is low, as compared to global signals [75]. Therefore the ability of PSSs to damp inter-area oscillations is limited. Moreover, PSSs are typically tuned based on a single operating scenario, and hence they are less effective in handling changes in

operating conditions such as load changes, or variations in network topology [75]. For this reason, an inter-area oscillation can be inadequately damped by a PSS, and can give rise to instability in the interconnected system.

As a result of the increasing use of Wide Area Measurement Systems (WAMS) in power systems, there has been a growing interest in utilizing remote signals to damp inter-area oscillations. The acquisition of WAMS-signals is based on Phasor Measurement Units (PMUs). PMUs measure and sample the voltage and current waveforms at system buses, and use synchronization signals from the Global Positioning System (GPS) [77, 78]. The synchronized time sampling enables the creation of a real-time picture of the system at the control centers. WAMS based control was enabled using the measurement signals provided by the PMUs, as shown in Fig. 5.1. The Phasor Data Concentrator (PDC) filters the data gathered through PMUs and dispatches the required signals for monitoring and control applications.

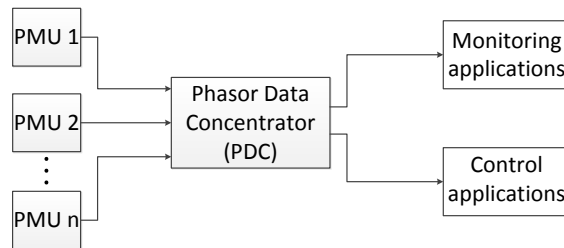


Figure 5.1: General structure of WAMS control.

The damping of power system oscillations using FACTS devices has also been investigated, with remote signals once again showing a superior performance in the damping of inter-area oscillations, as compared to local signals. Different POD controller designs were reported in literature, including the conventional lead-lag design [81, 82], as well as  $H_2/H_\infty$  designs, which were used to ensure the robustness of the controller under various operating conditions. Despite its efficacy in dealing with changing operating conditions, the  $H_\infty$  controller design has a difficulty in selecting the weighting functions, which is due to the involvement of multiple generators in the targeted inter-area modes [83]. The tuning of weighting functions becomes harder as the system size is larger, as the weights added affect multiple modes other than those originally targeted by the controller. On the other hand, Linear Quadratic Gaussian (LQG) control was also used for POD controller design [58, 80]. The LQG control approach relies on reaching a tradeoff between error minimization due to deviations of the targeted states, and a minimum

control effort, which are both defined through the quadratic cost function. Despite its advantages, the weighting functions in LQG control problems are once again complex to derive, as the weights do not directly target the inter-area modes. Thus, the weights are determined based on a participation factor analysis. As the system size gets larger and multiple inter-area modes are targeted, the design process becomes increasingly complex [80, 84].

As the LQG cost function can be expressed in terms of any variable on the condition of being a linear combination of dynamic states, a modal formulation of the cost function has been proposed in [58]. The advantage of this modal formulation is that it renders each element of the weighting function directly responsible for an oscillatory mode, thus it enables to target the inter-area oscillations only without affecting the remaining local modes. The resulting controller design is of Multiple Input Single Output (MISO) structure. This chapter utilizes the Modal LQG (MLQG) strategy for the design of a POD controller in an embedded VSC-MTDC network. The controller placement is determined based on the eigenvalue sensitivity of the least-damped targeted inter-area mode [59, 60]. The controller placement using eigenvalue sensitivity aims to find the POD's controller location where its damping performance is maximum, as explained in the next section.

## 5.2 Derivation of eigenvalue sensitivity

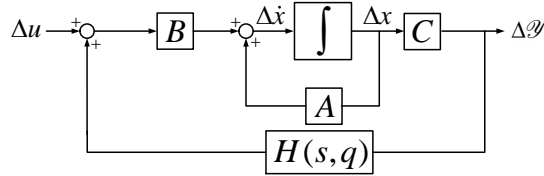


Figure 5.2: State space block diagram of linearized power system model.

The approaches used for eigenvalue sensitivity calculation are generally divided into explicit [54], implicit [55], and hybrid [56] methods. Depending on the power system model being used, the sensitivity is calculated in terms of state and/or algebraic variables. In the explicit form, the state variable derivatives are written exclusively in terms of state variables. In the implicit form, both state and algebraic variables are used in writing the sensitivity expression. On the other hand, the hybrid form utilizes the linearized model of the power system to derive the sensitivity expression. The linearized state space power system model used in this section is

shown in Fig. 5.2. This section summarizes the derivation of the linearized state space model as well as the calculation of eigenvalue sensitivity.

The derivation of system linearization is performed as described in section 3.2. Hence the linearized state-space model is given as:

$$\Delta \dot{x} = A\Delta x + B\Delta u \quad (5.1)$$

$$\Delta \mathcal{Y} = C\Delta x \quad (5.2)$$

where  $\Delta \mathcal{Y}$  is the vector of outputs,  $A$  is the system matrix,  $B$  is the input matrix,  $C$  is the output matrix. The supplementary controller is represented by  $H(s, q)$  in Fig. 5.2, whose input is determined by  $\Delta \mathcal{Y}$  and whose output makes a contribution that is added to  $\Delta u$ .

The sensitivity of the closed loop eigenvalue  $\lambda_i$  with respect to the parameter  $q$  of the controller is given by:

$$\frac{\partial \lambda_i}{\partial q} = R_i \frac{\partial H(s, q)}{\partial q} \Big|_{s=\lambda_i} \quad (5.3)$$

where  $R_i$  is the residue of the transfer function given by  $\frac{\Delta y}{\Delta u}$ . The residue is obtained as:

$$R_i = w_i^T B \frac{1}{(1 - H(\lambda_i, q))^2} C v_i \quad (5.4)$$

where  $v_i$  and  $w_i$  are the right and left eigenvectors corresponding to the mode  $\lambda_i$ , respectively. The eigenvalue sensitivity is therefore split into these two components, which correspond to the location of the controller and a generalized parameter  $q$  in the controller's transfer function  $H(s, q)$ . The use of  $q$  is limited to the calculation of sensitivity, so it does not express the real number of parameters in the actual controller. In case of controller absence, the value of transfer function  $H(\lambda_i, q)$  is null. The arising eigenvalue sensitivity in this case is used to evaluate the optimal location for supplementary controller placement, with the optimum location being where the magnitude of the sensitivity is maximum (assuming equal observability factors for the signals). In this case, the expression for eigenvalue sensitivity becomes [59, 60]:

$$\frac{\partial \lambda_i}{\partial q} = w_i^T B C v_i \quad (5.5)$$

## 5.3 MLQG control design

### Derivation of control law

This section describes the MLQG control design process. The derivation for all variables given hereby excludes  $\Delta$  as the design is understood to be based on the linear model. The linearized state space system model with process noise  $\chi$  and measurement noise  $v$  is given as [58, 61]:

$$\dot{x} = Ax + Bu + \Gamma\chi \quad (5.6)$$

$$\mathcal{Y} = Cx + v \quad (5.7)$$

The process and measurement noises are assumed as uncorrelated zero mean Gaussian stochastic processes. The control problem for LQG in modal form is to develop a feedback control law that minimizes the estimated value ( $E\{\}$ ) of the following cost function:

$$J_k = \lim_{T \rightarrow \infty} E \left\{ \int_0^T \left( x^T (M^T Q_m M) x + u^T Q_c u \right) dt \right\} \quad (5.8)$$

where  $Q_m$  and  $Q_c$  are the weighting matrices of modal variables and controller outputs, respectively, while  $M$  is a real mapping matrix that relates the system modal variables  $z$  and state variables  $x$  such that:

$$z(t) = Mx(t) \quad (5.9)$$

where  $M$  is obtained through a real Schur decomposition [68] that guarantees real values for the elements of  $M$ . The modal variables in  $z(t)$  relate to the system modes directly, such that each mode is dealt with in the form of  $e^{\lambda_i t}$ , where  $i = 1, \dots, n$ , with  $n$  being the order of the system. The benefit of using the modal variables to formulate the cost function in (5.8), is to avoid the complexities associated with conventional LQG controller design that are due to the involvement of multiple generators into targeted modes [61]. The cost function aims to minimize the error while keeping a minimum control effort, as determined by the relative weights of the elements in  $Q_m$  and  $Q_c$  matrices. The weighting matrices are usually formed as

diagonal matrices. The diagonal elements of  $Q_c$  are selected so as to penalize the controller outputs with a high values, while the diagonal elements of  $Q_m$  are selected so as to penalize the modal variables when deviating from steady state values. As each diagonal element in  $Q_m$  is associated with a system mode, the particular modes of interest are given non-zero weights in  $Q_m$ , while the other modes' weights are set to zero. The Linear Quadratic Regulator (LQR) controller gain  $K$  is obtained from the solution of Algebraic Riccati Equation (ARE) based on the cost function in (5.8). The feedback control law is given as:

$$u(t) = -Kx(t) \quad (5.10)$$

where  $K = Q_c^{-1}B^T X$  is the constant state feedback matrix.  $X = X^T \geq 0$  is a positive semi-definite matrix that is the solution of the ARE given by:

$$A^T X + XA - XBQ_c^{-1}B^T X + Q_m = 0 \quad (5.11)$$

Hence, the closed loop dynamic with feedback control is given by:

$$\dot{x} = Ax - BKx + \Gamma\chi \quad (5.12)$$

However, the control law in (5.12) assumes that the system states are measurable, which is not a realistic assumption in power systems. Thus, an estimate  $\hat{x}$  of the states is used in the feedback control as follows:

$$u(t) = -K\hat{x}(t) \quad (5.13)$$

where  $\hat{x}(t)$  is the estimate of the states computed using Kalman filter, as shown in Fig. 5.3. Hence, the dynamic equation for state estimate is given as:

$$\dot{\hat{x}}(t) = A\hat{x} + Bu + L(\mathcal{Y} - C\hat{x}) + Lv \quad (5.14)$$

where  $L$  is the estimation error feedback matrix. The choice of  $L$  is made such

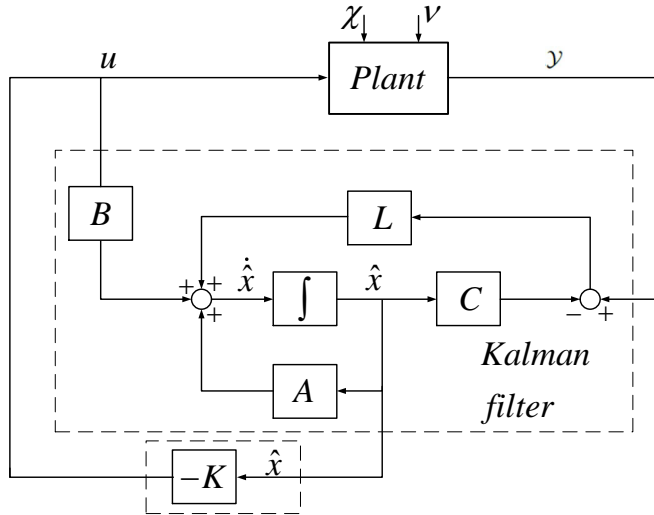


Figure 5.3: MLQG controller structure.

as to minimize  $E\{[x - \hat{x}]^T [x - \hat{x}]\}$ . This is accomplished by solving the ARE corresponding to the following cost function, where  $W$  and  $V$  are the spectral density matrices of process and measurement noises, respectively:

$$J_L = \lim_{T \rightarrow \infty} E \left\{ \int_0^T (x^T W x + u^T V u) dt \right\} \quad (5.15)$$

Thus, the closed loop dynamics of the LQG controller are described by:

$$\frac{d}{dt} \begin{bmatrix} x \\ \hat{x} \end{bmatrix} = \begin{bmatrix} A & -BK \\ LC & A - LC - BK \end{bmatrix} \begin{bmatrix} x \\ \hat{x} \end{bmatrix} + \begin{bmatrix} \Gamma \chi \\ Lv \end{bmatrix} \quad (5.16)$$

The transfer function of the controller from the output ( $\mathcal{Y}$ ) to the input ( $u$ ) is given by:

$$K_{LQG}(s) = \begin{bmatrix} A_c & B_c \\ C_c & D_c \end{bmatrix} = \begin{bmatrix} A - BK - LC & L \\ -K & 0 \end{bmatrix} \quad (5.17)$$

### POD controller structure

The modulation of active power for the purpose of oscillation damping is achieved by adding the supplementary controller output to the active power setpoint, as shown in Fig. 5.5. In this figure, the input to POD controller is  $\Delta P_{line}$  (which corresponds to  $\Delta \mathcal{P}$  in Fig. 5.2), while the output of the POD controller is taken as  $E_q$  (which corresponds to  $\Delta u$  in Fig. 5.2). The main active power controller is represented by the PI (Proportional Integral) block. On the other hand,  $E_q$  is the converter voltage component that is used to regulate the active power. The details of main controller model and operation are given in [62, 63].

The conventional POD controller structure consists of a lead-lag filter, where the parameters are determined by the residue method [64] as given in Chapter 3. It was assumed that one POD controller only is used at VSC1. In this case, the local input signal is taken as the line power. As a result of the SISO structure of the controller, the lead-lag parameters can be tuned based on one mode only, which is taken as the least damped mode. A combination of multiple SISO damping controllers would be equally unable to target the intended modes only, as the application of a single controller adjusts the dampings and directions of the other modes. On the other hand, the MISO structure of the controller in case of MLQG-based POD enable multiple inputs to the POD controller, as shown in Fig. 5.6. Thus, multiple oscillatory modes can be targeted simultaneously. In this case, the number of input signals to the POD controller is equal to the number of modes being targeted. The WAMS input signals to the controller are provided by the Phasor Measurement Units (PMUs) deployed in the system. For simplification, it was assumed that PMUs are adequately placed to obtain the required line powers. The time delays associated with remote signals' transmission were modelled using Padé approximation [79, 80], as shown in Fig. 5.4.

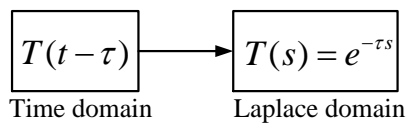


Figure 5.4: Time delay representation.

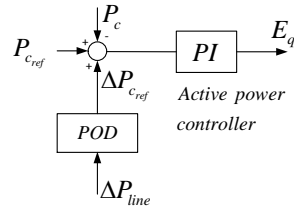


Figure 5.5: Incorporation of conventional POD controller.

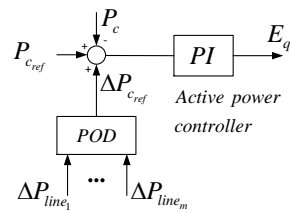


Figure 5.6: Incorporation of MLQG-based POD controller.

## 5.4 Test power system

The test power system used in the study is shown in Fig. 5.7. The control of DC voltage in the VSC-MTDC network is assigned to VSC2, while VSC1 and VSC3 operate in active power control mode. The generators are represented by one-axis model [18] with Automatic Voltage Regulator (AVR). The generators  $G_1$  and  $G_3$  are also equipped with PSSs. The system loads are represented as constant impedance loads. On the other hand, the converters are represented by the average model [27], which represents each VSC as a voltage source with controllable magnitude and phase angle. The test system data is given in [60].

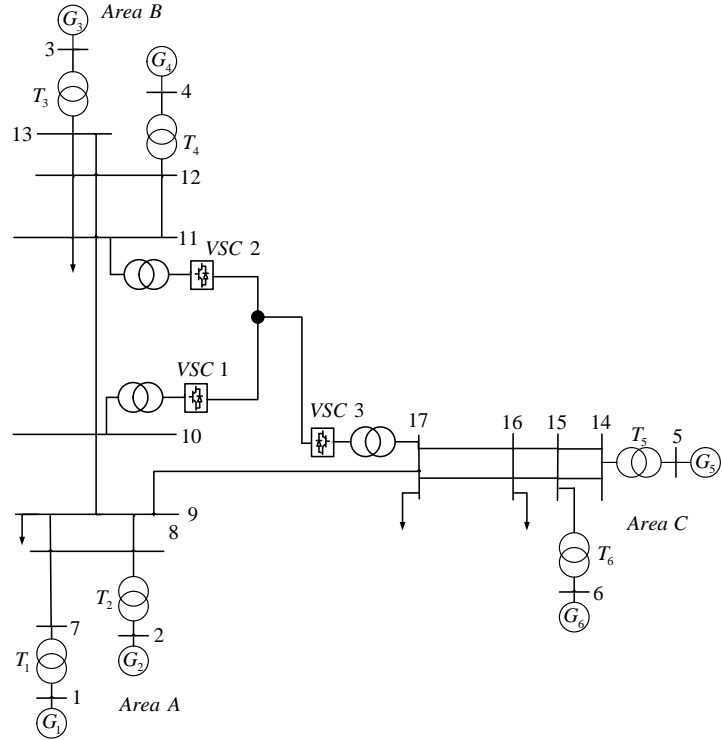


Figure 5.7: Three-area test power system.

## 5.5 Results

### Small signal stability results

Table 5.1: Inter-area modes in the test power system.

	Mode	$f$ (Hz)	$\zeta$
$\lambda_{4,5}$	$-0.1308 \pm j4.7180$	0.7509	0.0306
$\lambda_{14,15}$	$-0.1634 \pm j4.5021$	0.7165	0.0363
$\lambda_{19,20}$	$-0.2441 \pm j5.0713$	0.8071	0.0481

The oscillatory inter-area modes of the system with a damping ratio below 5% are shown in Table 5.1. It could be noticed that  $\lambda_{4,5}$  is the least damped mode, the mode shape of  $\lambda_{4,5}$  is shown in Fig. 5.8. The figure shows that the mode represents an oscillation between the generators of area B against those of areas A and C, respectively.

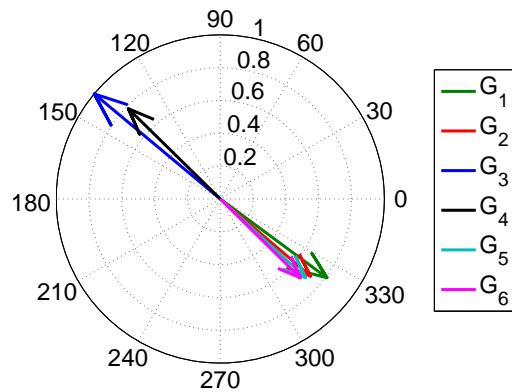


Figure 5.8: Mode shape of  $\lambda_{4,5}$ .

Table 5.2: Inter-area mode sensitivities corresponding to potential controller locations.

	Mode:	$\lambda_{4,5}$	$\lambda_{14,15}$	$\lambda_{19,20}$
VSC1		0.9731	0.8506	0.7031
VSC2		0.7071	0.7413	0.6882
VSC3		0.6513	0.5028	0.6613

The magnitudes of inter-area mode sensitivities corresponding to the possible controller placements at VSC1, VSC2, and VSC3 are shown in Table 5.2. The table shows that sensitivity to the least damped inter-area mode is highest at VSC1. Therefore, it turns out that the controller placement at VSC1 would yield the optimal damping performance. For the purpose of sensitivity calculations given in Table 5.2, the input signal to the controller was taken as  $P_{10-11}$ , which is the active power flow over the tie line between buses 10 and 11.

The impact of conventional and MLQG-based POD controllers placement on small signal stability of the system is shown in Fig. 5.9. The figure shows the ability of the controller to displace the inter-area mode further to the left of the complex plane, as compared to the performance of the conventional PSS-based POD. Upon MLQG-based controller deployment, the damping of  $\lambda_{4,5}$ ,  $\lambda_{14,15}$ , and  $\lambda_{19,20}$  rose to 9.32%, 10.31%, and 8.3%, respectively, based on the controller input signals given in the next section. On the other hand, the conventional POD controller was tuned according to the residue of  $\lambda_{4,5}$  only, since the lead-lag block parameters can be tuned to one mode only. Consequently, it could be noticed that the conventional POD controller was not capable of raising the damping of  $\lambda_{19,20}$  above the target value of 5% indicated by the dotted line in Fig. 5.9.

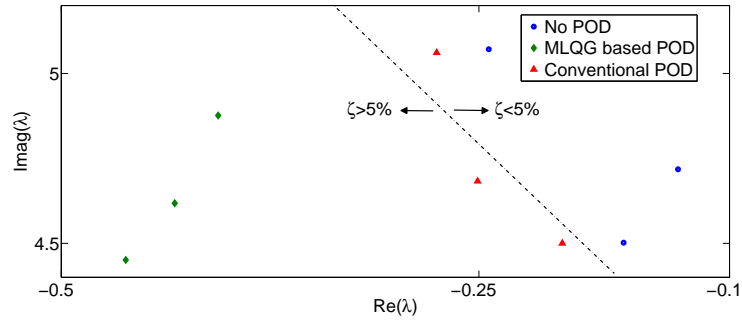


Figure 5.9: Variation of inter-area modes due to POD controller placement.

### Selection of MLQG controller input signals

A study of the modal observability of potential input signals to the MLQG-based POD controller was conducted, with the purpose of determining the signals with highest observability for the targeted modes of interest. The input signals considered in the study were limited to the active power flows in lines. As the controller targets multiple modes, the number of controller inputs is equal to the number of modes of interest. The values of normalized modal observability factors for the inter-area modes of interest are shown in Table. 5.3, where the base value is taken as the maximum value of observability for each controller input signal. It is assumed that Phasor Measurement Units (PMUs) are appropriately placed such that they are capable of readily providing the required input signals to the controller, with a time delay represented by a 2<sup>nd</sup> order Padé approximation. Based on the results in Table

5.3, it turns out that the modes  $\lambda_{4,5}$ ,  $\lambda_{14,15}$ , and  $\lambda_{19,20}$  can be most observed in the active powers of lines  $L_{12-13}$ ,  $L_{5-14}$ , and  $L_{11-12}$ , respectively.

Table 5.3: Inter-area modes' observability factors for controller input signals.

	$P_{12-13}$	$P_{5-14}$	$P_{11-12}$
$\lambda_{4,5}$	1	0.4027	0.6974
$\lambda_{14,15}$	0.3282	1	0.3402
$\lambda_{19,20}$	0.6813	0.3661	1

### Controller performance in case of load change

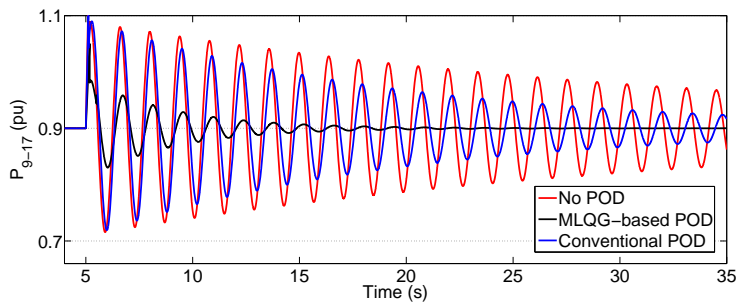


Figure 5.10: Power flow over  $L_{9-17}$  following temporary load increase at bus 9.

Table 5.4: Settling times for power flow over  $L_{9-17}$ .

	Settling time (s)
No POD	> 30
Conventional POD	20
MLQG-based POD	12

The performance of the POD control was tested in case of a 10% temporary load increase for 0.1 s at bus 9. The variation of active power over the tie line  $L_{9-17}$

is shown in Fig. 5.10. The figure shows an extended period of oscillations in case of absence of the POD control at VSC1. The conventional POD control was able to reduce the period of oscillations following the disturbance, however the damping provided by the controller was not optimal as the parameters were not tuned to the inter-area mode between areas A and C. On the other hand, the performance of the MLQG-based POD controller shows to be superior to the conventional one, due to the use of multiple inputs in controller operation. The settling times for the respective cases in Fig. 5.10 are shown in Table. 5.4. The settling time was defined as the time passed for the line power to be bounded within  $\pm 2\%$  of its steady state value.

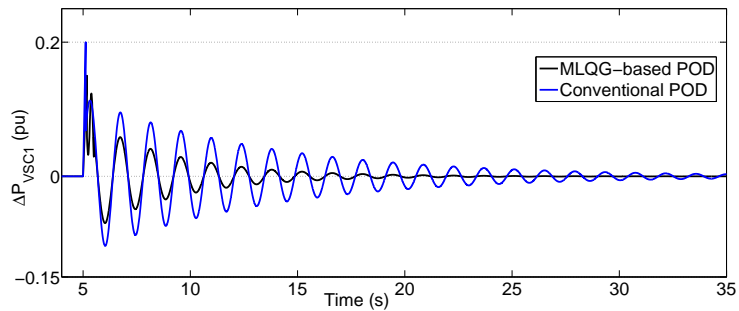


Figure 5.11: Variation in output power at VSC1 due to POD control.

A comparison of POD control effort in case of conventional and MLQG is given in Fig. 5.11. The figure shows the variation in output power of VSC1 due to POD controller contribution. In case of MLQG control, the variation in power is limited to  $\pm 0.1 pu$  thanks to the application of weighting matrix  $Q_c$  which limits the controller output effort.

### Controller performance in case of short circuit fault

A three-phase short circuit fault was applied for 100 ms at bus 10. The power flow over the tie line  $L_{10-11}$  is shown in Fig. 5.12. The figure shows a period of prolonged power oscillations over the tie line in the absence of POD control. Although the conventional POD controller was able to reduce the period of power oscillations, however the suboptimal tuning of the controller cannot achieve a swift damping of the oscillations following the fault clearing. On the other hand, the MLQG-based controller is capable of targeting all the inter-area modes involved,

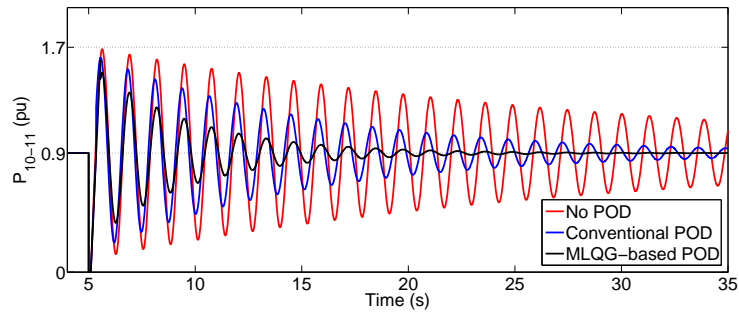


Figure 5.12: Power flow over  $L_{10-11}$  following three-phase fault at bus 10.

and therefore it was able to provide an optimal damping of the power oscillations that followed the fault clearing.



## **Chapter 6**

# **Supply of a Zero-inertia System through Hybrid MTDC Network**

This chapter discusses the control and operation of a hybrid MTDC system that supplies a passive network with no local generation. As the EMTP-RV simulation environment was used in this chapter, the content will accordingly be oriented towards the model implementation of the test system in that simulation software.

### **6.1 Foreword**

Hybrid HVDC systems with both LCCs and VSCs have been contemplated since 1994 [13], the typical range of applications for hybrid HVDC systems include power supply to island networks, as well as transmission links that only require a unidirectional flow of power. The main motivation behind hybrid HVDC systems was to combined the benefits of LCC's low cost and the VSC's independent control of the active and reactive power. Subsequently, hybrid MTDCs with more than two terminals were first contemplated in [15]. Hybrid MTDCs are also contemplated for power supply to islands, but have also been considered for power grid integration of renewable energy sources [71], when the receiving end network is a strong one. This chapter presents an electromagnetic simulation study of a hybrid MTDC network supplying a passive network that has no local generation. The transmission scenario presented in the chapter resembles that in case of a power supply to an island with no local generation, and hence there is no inertia at the network supplied by the converters. The control strategies of LCC and VSC converters are presented and discussed. Two control scenarios for VSCs supplying the passive networks are

proposed and compared, along with additional control schemes developed to handle converter tripping contingencies. This chapter deals with the specific case of using the hybrid MTDC in supplying an AC system with no local generation, which is one of the hybrid MTDC system's most advantageous applications, as there will be no need to reverse the power flow over the DC lines.

## 6.2 Converter models in EMTP-RV

As an electromagnetic transient simulation program is fundamentally different from an RMS simulation one, this section sheds some light on the modeling of LCC and VSC converters used in EMTP-RV. In an electromagnetic simulation, the switching of a converter's power devices is actually implemented, instead of using an average model of the converter (as previously explained in chapter 3 of this thesis). As the converter switching is represented, a brief explanation of the control and switching circuits for both the LCC and VSC is given in this section.

### LCC model

The LCC's operation is based on thyristors, which are essentially ON-controlled power devices (i.e. their turn-on is controlled via firing pulses, but their turn-off takes place due to line commutation). The block diagram representation of the LCC's control and switching circuits is shown in Fig. 6.1, where  $\alpha$  is the firing angle command of the LCC's thyristors.

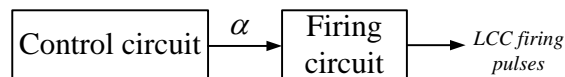


Figure 6.1: LCC representation in EMTP-RV.

### VSC model

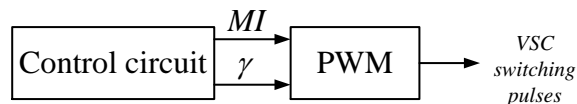


Figure 6.2: VSC representation in EMTP-RV.

In detailed model of the VSC, the control circuit produces two main quantities that are used in generating the output voltage of the VSC, namely the modulation index ( $MI$ ) and VSC voltage phase angle ( $\gamma$ ). The modulation index regulates the magnitude of the VSC’s output voltage, while the angle  $\gamma$  regulates the amount of power exchanged between the VSC and the connected AC system. A block diagram representation of the VSC and its control circuit is shown in Fig. 6.2.

### 6.3 Test system

The test system studied in this chapter is shown in Fig. 6.3. Both LCC1 and LCC2 are assumed to be connected to strong AC grids. On the other hand, VSC1 and VSC2 supply the passive load through identical transmission lines of equal length. The next section elaborates on the control modes selected for LCC and VSC converters.

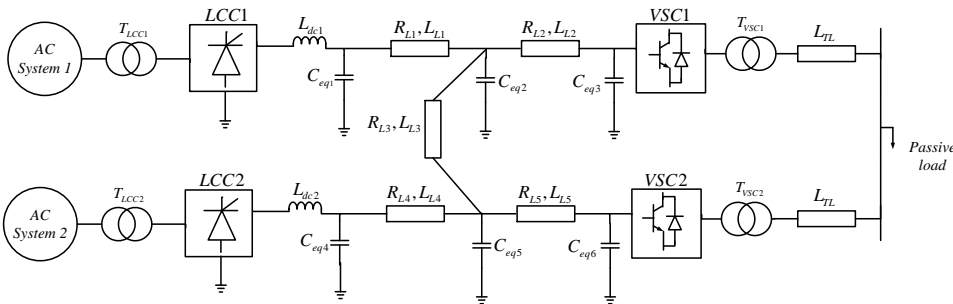


Figure 6.3: Test power system with hybrid MTDC network.

### 6.4 Hybrid MTDC network control system

The control system in the hybrid MTDC network deals with both LCC and VSC converters. The LCC controllers are shown in Fig. 6.4 and Fig. 6.5, respectively.

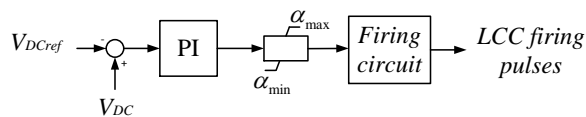


Figure 6.4: DC voltage control at LCC.

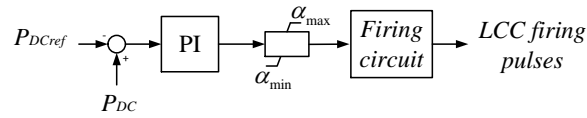


Figure 6.5: Active power control at LCC.

On the other hand, the control strategy used at the VSC can be one of the following:

- Direct control: in this strategy, the AC voltage magnitude and angle are directly regulated through PI controllers, as shown in Fig. 6.6. In this case, the control is directly implemented in three-phase ( $abc$ ) frame without the need for coordinate transformation. Although this control is not preferred in case of VSC connection to an active AC network, however it is sufficient in case of VSC connection to a passive network, since the converter acts as the sole voltage source for the connected load [71, 72].

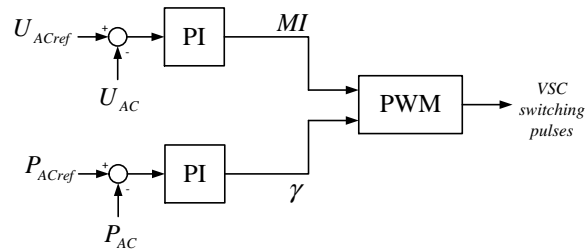


Figure 6.6: Direct control strategy at the VSC.

- Vector control: in this strategy, a coordinate transformation from the three-phase  $abc$  reference frame to two-axis  $dq$  reference frame is conducted, consequently the two-axis currents ( $i_d$  and  $i_q$ ) are regulated in  $dq$  reference frame. The advantage of this strategy is that it's capable of achieving an independent control of d-axis and q-axis currents, and therefore an independent control of active and reactive power can be achieved by coupling each of them to one current component [71, 72]. The block diagram for vector control strategy is shown in Fig. 6.7. The figure shows the inner control loops for d-component ( $i_d$ ) and q-component ( $i_q$ ) currents. On the other hand, the outer loop controllers are selected according to the operating mode of the VSC. The figure shows the methodology of implementing the vector control of the

VSC in EMTP-RV. The  $d$  and  $q$  components of system voltage are given by  $V_{sd}$  and  $V_{sq}$ , while the converter voltage  $d$  and  $q$  components are given by  $V_{cd}$  and  $V_{cq}$ , respectively.

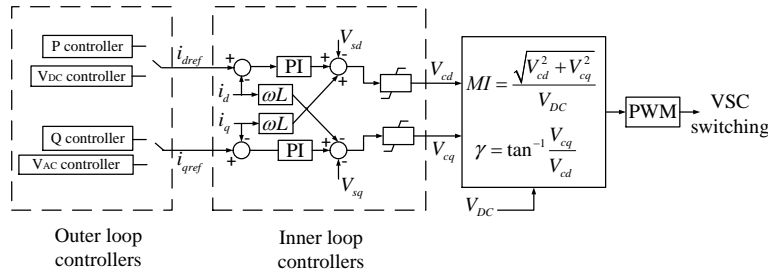


Figure 6.7: Vector control strategy at the VSC.

Based on vector control strategy, the possible control modes are summarized in Table 6.1.

Table 6.1: Possible VSC control modes.

	$d$ -component	$q$ -component
Scenario 1	DC voltage control	Reactive power control
Scenario 2	Active power control	Reactive power control
Scenario 3	Active power control	AC voltage control

As for the test system considered in this thesis, two control scenarios were developed and tested. These control scenarios are given and described as follows:

### Control scenario A

In this scenario, both VSC1 and VSC2 were operated in AC voltage control mode implemented through direct control scheme, with Phase Locked Loop (PLL) synchronizing the output voltages of converters. On the other hand, LCC1 and LCC2 were operated in DC voltage and active power control modes, respectively as given in Fig. 6.4 and 6.5, respectively. The control modes of the converters in control scenario A are shown in Table. 6.2.

Table 6.2: Control scenarios A and B for LCCs and VSCs.

	Control scenario A	Control scenario B
LCC1	DC voltage control	
LCC2	Active power control	
VSC1	AC voltage control	AC voltage control
VSC2	AC voltage control	Active power control

### Control scenario B

In this scenario, VSC1 was operated in AC voltage control mode implemented through direct control, while VSC2 was operated in active power and AC voltage control mode based on vector control methodology. LCC1 and LCC2 were also operated in DC voltage and active power control modes, respectively. The control modes of the converters in control scenario B are also shown in Table. 6.2.

## 6.5 Converter tripping contingency control schemes

In order to handle a converter tripping condition, event-triggered control schemes were developed with the purpose of avoiding the system collapse in case of a converter outage. The control schemes adjust the control modes of the remaining converters in order to retrieve the control functions that were lost due to the fault. This section presents the LCC and VSC tripping contingency control schemes.

### LCC tripping contingency control scheme

The flow chart for the control scheme that handles the LCC tripping is shown in Fig. 6.8. The scheme operation is based on local DC voltage measurements to detect the tripping condition. A threshold value of 0.95 pu is used to detect a potential tripping of LCC1, as shown in Fig. 6.9. Next, the rate of change of DC voltage is used to differentiate the tripping condition from momentary dips in the value of DC voltage. The threshold value of  $\frac{dV_{DC}}{dt}$  was determined based on the conducted simulations. The scheme also employs an intentional time delay of 80 ms before adjusting the control mode of LCC2 in order to ensure that the loss of DC voltage control function is a permanent, not a temporary one. Upon the detection of the DC voltage controlling station tripping, the control mode at LCC2 is switched to DC voltage control.

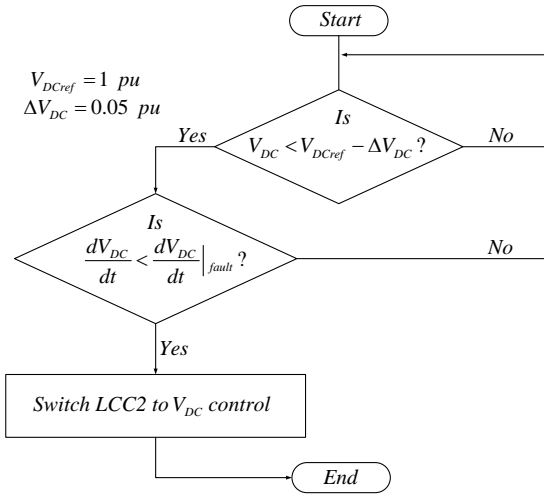


Figure 6.8: Flow chart for control scheme handling the tripping of LCC1.

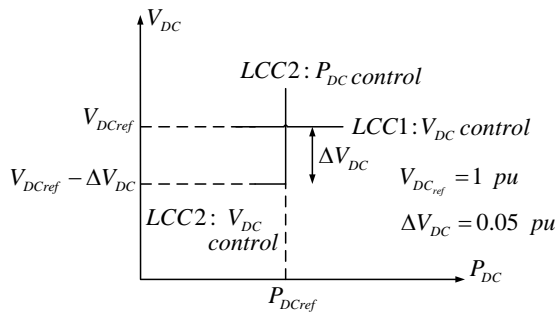


Figure 6.9: LCC1 tripping scheme operation.

**VSC tripping contingency control scheme**

The flow chart for VSC tripping control scheme is shown in Fig. 6.10. The scheme is intended to complement the operation of control scenario B, as it operates in case of VSC1 tripping and the loss of AC voltage control in the passive network. The scheme operates based on the detection of a disturbance in system frequency that results upon the tripping of VSC1. The scheme operation is shown in Fig. 6.11. The scheme operates upon detecting an increase in average system frequency, along with a high rate of change of power input to the DC side of VSC2 that occurs upon the tripping of VSC1. The threshold value for  $\frac{dP_{DC}}{dt}$  was determined through the

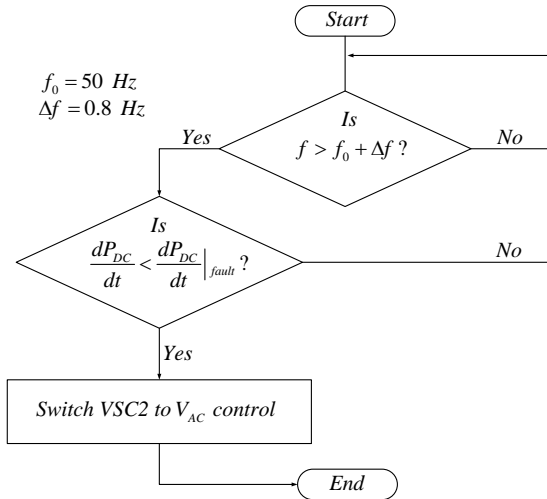


Figure 6.10: Flow chart for control scheme handling the tripping of VSC1.

conducted simulations. The condition on the rate of change of DC power at VSC2 is necessary to ensure that the scheme does not operate in case of a DC fault, which can also cause a disturbance in the system frequency.

In case of scheme operation, the control mode at VSC2 is switched to AC voltage control under direct control, as explained in the previous section.

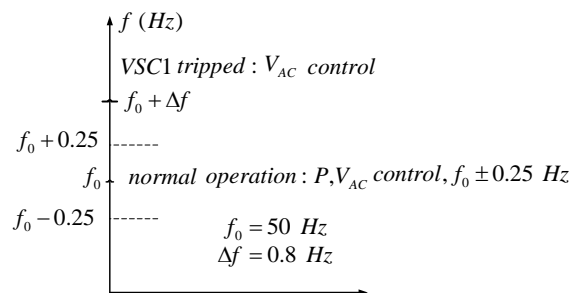


Figure 6.11: Operation of control scheme handling the tripping of VSC1.

It is worth noting that in case of control strategy A applied at the VSC control, there is no need to operate the VSC tripping contingency scheme. This comes as a result of both VSC1 and VSC2 operating in AC voltage control mode, therefore in case of VSC1 tripping, the AC voltage control function is not lost.

## 6.6 Results

### LCC1 tripping

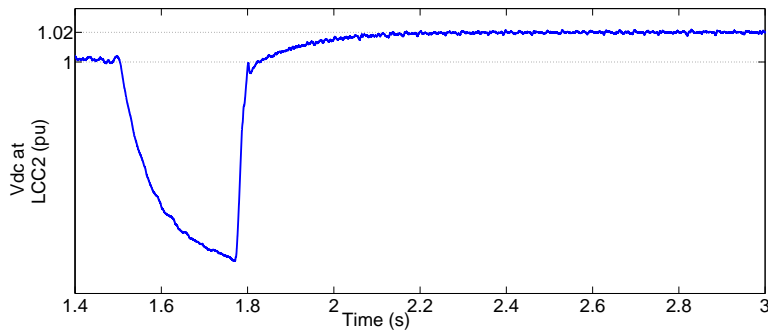


Figure 6.12: DC voltage at LCC2 upon the tripping of LCC1.

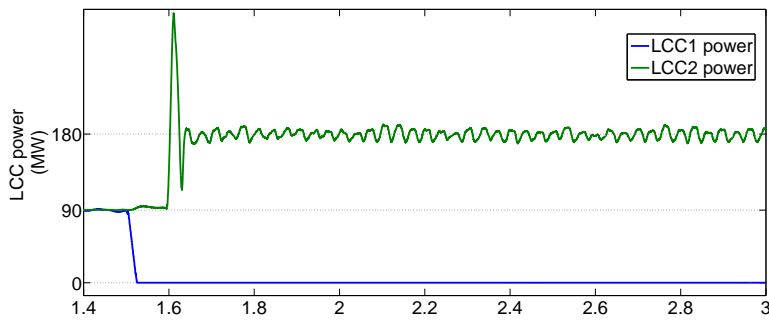


Figure 6.13: LCCs' active power outputs upon LCC1 tripping contingency.

The contingency of LCC1 tripping was implemented at 1.5 s of simulation time to test the operation of the LCC tripping scheme in case of the loss of DC voltage control. The result is shown in Fig. 6.12. The figure shows a drop in DC voltage as the DC voltage control at LCC1 is lost, subsequently the DC fault scheme operates to switch LCC2 to DC voltage control mode. On the other hand, the active power output of LCCs and load power are shown in Fig. 6.13 and 6.14, respectively. The figures show that the LCC tripping scheme was capable of restoring the load power to the pre-contingency level within 0.7 s of the LCC tripping.

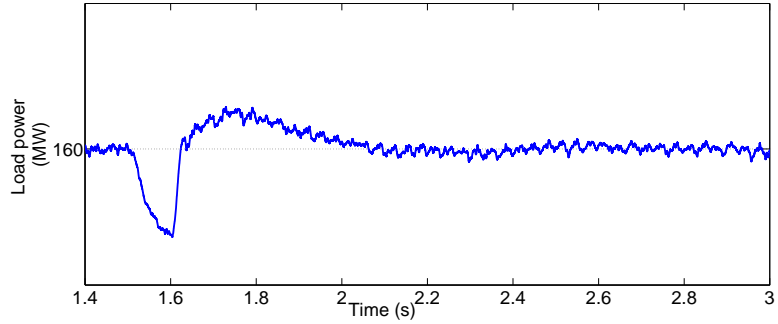


Figure 6.14: Load power upon LCC1 tripping contingency.

### VSC1 tripping

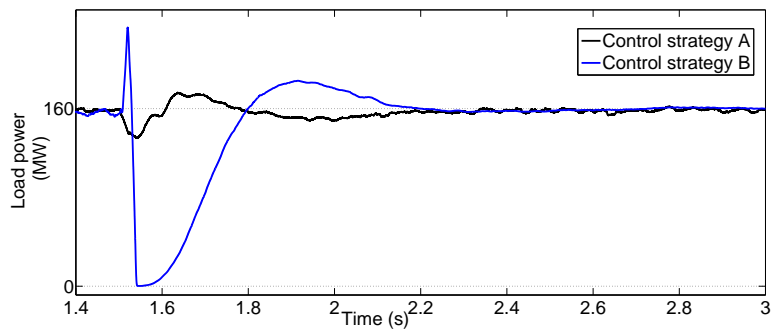


Figure 6.15: Load power upon VSC1 tripping contingency.

The contingency of VSC1 tripping was applied at 1.5 s of simulation time. The load power is shown in Fig. 6.15. The figure shows a faster restoration of load power in case of control strategy A, as a result of redundant AC voltage control at both VSC1 and VSC2 converters. On the other hand, the system frequency is shown in Fig. 6.16. Once again, the figure shows a smaller frequency excursion in case of control strategy A, as there has been no adjustment of controller objective for VSC2. It is worth noting that the frequency excursion in system frequency at control strategy B is due to the momentary disconnection of controller at VSC2, as the new controller is brought into service to regulate the AC voltage.

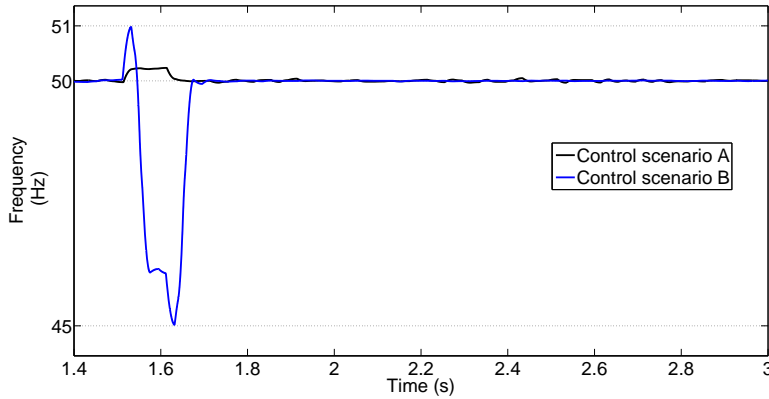


Figure 6.16: System frequency upon VSC1 tripping contingency.

### DC line fault

A DC line fault was applied at 1.5 s of simulation time. The fault was applied at the midpoint of the line connecting LCC2 with VSC2 (i.e. at the meeting point of L3, L4, and L5). The DC voltage behavior in case of various fault clearing times are shown in Fig. 6.17. The figure shows that the post-fault magnitude of DC overvoltage gets reduced as the clearing time gets shorter. On the other hand, the figure also shows the difference between the post-fault DC voltage value in case of LCC1 tripping. It's worth noting that the LCC tripping contingency scheme operation was not triggered by the DC fault condition. It is also worth noting that the DC fault clearing times did not consider the DC cable ability to withstand the flow of fault current. That is, it was assumed that the DC cables can safely withstand the flow of fault current for the entire fault duration.

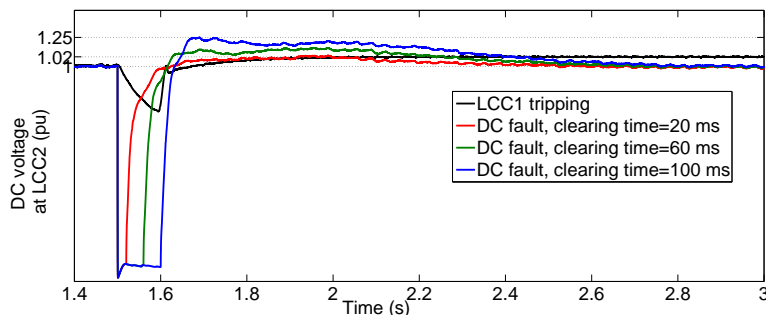


Figure 6.17: DC voltage upon DC fault clearing.



## Chapter 7

# Conclusion and Future Work

### 7.1 Conclusion

This thesis has discussed multiple issues related to the control of MTDC networks interconnecting AC power grids. The networks considered included both hybrid MTDC and VSC-MTDC networks. The modeling platform, presented in chapter 2, was furnished in a modular way that can be applied to various test systems. The general conclusion that can be drawn from the small-signal analysis study of AC/DC power systems is that controller interactions can significantly affect the stability of the combined AC/DC system. Hence, the coordination of various damping controllers is necessary to ensure that the simultaneous operation of multiple controllers is geared towards an enhancement of the overall stability in the system. In this vein, small-signal analysis was proven as a yardstick that can be used for studying the control interactions of various damping controllers.

The control strategy presented in Chapter 4 aims to enhance the combined AC/DC power system stability via operating point adjustment. The operating point is adjusted by means of varying the VSC controller setpoints. The variation of controller setpoints is made in proportion to the sensitivity of a stability to HB in case of load changes. On the other hand, the variation of setpoints is made according to optimized Power Transfer Distribution Factors (PTDFs). In this vein, the operating point adjustment strategy can be used as a tool for system operator to forestall the occurrence of disturbance that threatens the system stability, in case a low damping condition is detected in the system. Operating point adjustment is envisioned to form a part of Modal Analysis for Grid Operations (MANGO), which aims to utilize the modal analysis not just for monitoring, but also as a tool for

real-time control of the power system.

In Chapter 5, the design and placement of a MISO damping controller in an embedded VSC-MTDC network was presented. The controller placement is based on eigenvalue sensitivity analysis. On the other hand, the controller is based on MLQG linear control strategy, and uses WAMS signals for simultaneous targeting of multiple inter-area modes. The work was focused on the selection of an optimal location for the placement of a single damping controller within the VSC-MTDC network.

In Chapter 6, the control and operation of a hybrid MTDC network supplying a passive zero-inertia AC system were investigated. The supply of the passive AC system with redundant AC voltage control at the VSCs proved capable of handling a converter tripping contingency with a lesser impact on the quality of supply provided to the passive system. On the other hand, event-triggered converter tripping control schemes were successfully tested against both LCC and VSC tripping conditions.

## 7.2 Future Work

The MTDC network topology considered in this thesis was limited to the star-configured network. The MTDC network topology can be modified to consider other meshed network topologies. In this vein, it is also important to consider the DC fault condition and its effect on the connected AC systems.

In Chapter 4, the operating point adjustment strategy was presented for the purpose of stability enhancement in the AC/DC power system. In case of load changes, it was assumed that the delay in adjusting the VSC controllers' setpoints is negligible, while in case of faults, it was assumed that the time delay before the variation of setpoints is embedded in the fault clearing time. In a future research, the coordination between damping controllers (a.k.a modulation control) and operating point adjustment is to be investigated. As the damping controllers are capable of acting as a first line of action against disturbances to improve post-disturbance oscillation damping, operating point adjustment can be envisioned to act secondarily based on the system operator's decision to transfer the system to a new equilibrium point. The mechanism of coordination is to be investigated, together with considering the practicalities related to real-time implementation (such as communication latencies, and the presence of multiple TSOs).

In Chapter 5, a MISO POD controller design was presented based on the MLQG control strategy using WAMS signals. It was assumed that master-slave strategy is adopted for DC voltage control. In a future research, the DC voltage control

strategy is to be changed to droop control to observe the potential impact on the POD performance of the controller. Moreover, the formulation of the cost function for the MLQG controller is to be investigated to reach a coordination between the primary control objective of regulating the DC voltage, and the supplementary control objective of damping the power oscillations.

In Chapter 6, the supply of a passive AC system through VSCs was presented. In a future research, the number of VSCs supplying the passive system can be increased to study the coordination among different converters concerning AC voltage and frequency control in the passive grid. The research question to be addressed has to do mainly with maintaining the voltage and frequency within preset bounds to guarantee the quality and security of supply in a multi-infeed VSC-supplied AC grid. In this context, the study of potential control modes of the VSCs is to be investigated, especially concerning redundant AC voltage control at multiple converters. The research is also to include the dynamics of the Phase Locked Loop (PLL). As this kind of supply, which is entirely dependent on VSCs, is relatively a novel one, both dynamic and electromagnetic simulations are needed to comprehend the system operation.



# Bibliography

- [1] P. Bujis, D. Bekaert, D. Van Hertem, and R. Belmans, "Needed investment in the power system to bring wind energy to shore in Belgium", IEEE PowerTech 2009, Bucharest, Romania, 2009
- [2] European Climate Foundation, "Decarbonization roadmaps for the EU-27", ECF, Technical Report, 2010
- [3] Greenpeace, "Battle of the grids-how Europe can go 100% renewable and phase out dirty energy", Greenpeace, Technical Report, 2011
- [4] A. Ulbig, T.S. Borsche and G. Andersson, "Impact of low rotational inertia on power system stability and operation", Proceedings of the 19th IFAC World Congress, vol. 19, pp. 7290-7297, December, 2014
- [5] R. Rudervall, J. P. Charpentier, R. Sharma, "High Voltage Direct Current (HVDC) transmission systems technology review paper", Energy Week 2000, Washington DC, 2011
- [6] S. Cole, R. Belmans, "Transmission of bulk power: the history and applications of voltage-source converter high voltage direct current systems", IEEE Industrial Electronics magazine, p.6, September 2009
- [7] D. Tiku, "DC power transmission-mercury arc to thyristor HVDC valves", IEEE power and energy magazine, pp. 76-96, March/April 2014
- [8] REN 21, "Renewables 2012 global status report", 2017. [Online]. Available: [www.ren21.net](http://www.ren21.net)
- [9] N. Flourentzou, V. G. Agelidis, G. D. Demetriades, "VSC-based HVDC power transmission systems: an overview", IEEE Transactions on Power Electronics, Vol. 24, No. 3, 2009

- [10] D. Van Hertem, M. Ghandhari, "Multi-terminal VSC HVDC for the European supergrid: Obstacles", *Renewable and Sustainable Energy Reviews*, Vol. 14, No. 9, 2013
- [11] Grid Systems-HVDC, ABB, "It's time to connect", Technical Description of HVDC Light Technology, [www.abb.com/hvdc](http://www.abb.com/hvdc), 2008
- [12] A. M. Abbas, P. Lehn, "PWM based VSC-HVDC power transmission systems- A review", in *Proceedings 2009 IEEE PES General Meeting*, 2009
- [13] Z. Zhao, M. R. Iravani, "Application of a GTO voltage source converter in a hybrid HVDC link", *IEEE Transactions on Power Delivery*, Vol. 9, No. 1, 1994
- [14] Bjarne Andersen, "Hybrid HVDC system for power delivery to island networks", *IEEE Transactions on Power Delivery*, Vol. 19, No. 4, 2004
- [15] N. Nosaka, Y. Tsubota, K. Matsukawa, K. Sakamoto, H. Nakamura, M. Takasaki, H. Kawazoe, "Simulation studies on a control and protection scheme for hybrid multi-terminal HVDC systems", *IEEE Power Engineering Society Winter Meeting*, 1999
- [16] P. Kundur, *Power System Stability and Control*, McGraw Hill, New York, 1994
- [17] J. M. Morales, A. J. Conejo, H. Madsen, P. Pinson, M. Zugno, *Integrating renewables in electricity markets: operational problems*, Vol. 205, Springer US, Boston, MA, 2015
- [18] D. S. Kirschen, G. Strbac, *Fundamentals of Power System Economics*, Chichester, West Sussex, England, Hoboken, NJ: Wiley, first ed., May 2004
- [19] IEA, *Lessons from Liberalized Electricity Markets*, Paris: Organization for Economic Cooperation and Development, 2005
- [20] H. Bahar and J. Sauvage, "Cross-border trade in electricity and the development of renewables-based electric power", *OECD trade and environment working papers*, Organization for Economic Cooperation and Development, Paris, 2013

- [21] N. Hingorani and L. Gyugyi, *Understanding FACTS: Concepts and Technology of Flexible AC Transmission Systems*. New York: Wiley-IEEE Press, 1st edition, 1999
- [22] P. Kundur, J. Paserba, V. Ajjarapu, G. Andersson, A. Bose, C. Canizares, N. Hatziaargyriou, D. Hill, A. Stankovic, C. Taylor, T. Van Cutsem, and V. Vittal, "Definition and classification of power system stability IEEE/CIGRE joint task force on stability terms and definitions", *IEEE Transactions on Power Systems*, Vol. 19, No. 2, 2004
- [23] L. Rouco and I. Perez Arriaga, "Multi-area analysis of small signal stability in large electric power systems by SMA", *IEEE Transactions on Power Systems*, Vol. 8, No. 1, 1993
- [24] M. Ghandhari, G. Andersson, I. Hiskens, "Control Lyapunov functions for controllable series devices", *IEEE Transactions on Power Systems*, Vol. 16, No. 3, 2001
- [25] M. Ghandhari, G. Andersson, M. Pavella, and D. Ernst, "A control strategy for controllable series capacitor in electric power systems", *Automatica*, vol. 37, pp 1575-1583, 2001
- [26] J. Chen, T. T. Lie, and D. M. Vilathgamuwa, "Enhancement of power system damping using VSC-based series connected FACTS controllers", *IEE Proceedings - Generation, Transmission, and Distribution*, Vol. 150, No. 3, 2003
- [27] H. F. Latorre, M. Ghandhari, L. Söder, "Active and reactive power control of VSC-HVDC", *Electric Power Systems Research*, Vol 78, 2008
- [28] A. A. P. Lerm, C. Canizares, F. A. B. Lemos, "Multi-parameter bifurcation analysis of power systems", *North American Power Symposium (NAPS)*, 1998
- [29] A. A. P. Lerm, A. S. Silva, "Avoiding Hopf bifurcation in power systems via setpoint tuning", *IEEE Transactions on Power Systems*, Vol. 19, No. 2, 2004
- [30] S. P. Azad, R. Iravani, J. E. Tate, "Dynamic stability enhancement of a DC-segmented AC power system via HVDC operating point adjustment", *IEEE Transactions on Power Delivery*, Vol. 30, No. 2, 2015

- [31] W. Wang, G. Wang, M. Andersson, "Development in UHVDC multi-terminal and VSC DC grid", 2016 International High Voltage Direct Current Conference (HVDC 2016), 2016
- [32] R. Sadikovic, P. Korba, G. Andersson, "Application of FACTS devices for damping of power system oscillations", IEEE PowerTech Russia, 2005
- [33] L. X. Bui, V. K. Sood, S. Laurin, "Dynamic interactions between HVDC systems connected to AC buses in close proximity", IEEE Transactions on Power Delivery, Vol. 6, No. 1, 1991
- [34] W. Pan, Y. Chang, H. Chen, "Hybrid multi-terminal HVDC system for large scale wind power", IEEE PES Power Systems Conference and Exposition, 2006
- [35] C. Li, P. Zhan, J. Wen, M. Yao, N. Li, W. Lee, "Offshore wind farms integration and frequency support control utilizing hybrid multi-terminal HVDC transmission", IEEE Transactions on Industry Applications, Vol. PP, No. 6, 2013
- [36] Z. Dongling, H. Minxiao, S. Xu, "Coordination control for offshore wind power sending through hybrid HVDC", IEEE Grenoble PowerTech, 2013
- [37] X. F. Yuan, S. Cheng, "Simulation study for a hybrid multi-terminal HVDC systems", Proceedings of the Eighth International Conference on Electrical Machines and Systems (ICEMS), 2005
- [38] T. K. Vrana, R. E. Torres-Olguin, B. Liu, T. M. Haileselassie, "The north sea supergrid-A technical perspective", 9th International Conference on AC and DC Power Transmission, 2010
- [39] C. Guo, C. Zhao, "Supply of an entirely passive AC network through a double-infeed HVDC system", IEEE Transactions on Power Electronics, Vol. 24, No. 11, 2010
- [40] D. Kim, H. Nam, Y. Moon "A practical approach to HVDC system control for damping subsynchronous oscillation using the novel eigenvalue analysis program", IEEE Transactions on Power Systems, Vol. 22, No. 4, 2007
- [41] C. Karawita, U. D. Annakage, "A hybrid network model for small signal stability analysis of power systems", IEEE Transactions on Power Systems, Vol. 25, No. 1, 2010

- [42] G. O. Kalcon, G. P. Adam, O. Anaya-Lara, S. Lo, K. Uhlen, "Small signal stability of multi-terminal VSC-based DC transmission systems", *IEEE Transactions on Power Systems*, Vol. 27, No. 4, 2012
- [43] N. R. Chaudhuri, R. Majumder, B. Chaudhuri, "Stability analysis of VSC-MTDC grids connected to multi-machine AC systems", *IEEE Transactions on Power Delivery*, Vol. 26, No. 4, 2011
- [44] M. H. Nguyen, T. K. Saha, M. Eghbal, "Investigation on the impact of hybrid multi-terminal HVDC system combining LCC and VSC technologies using system identification", *22nd Australian Universities Power Engineering Conference (AUPEC)*, 2012
- [45] J. Beerten, S. Cole, R. Belmans, "Modeling of multi-terminal VSC HVDC systems with distributed DC voltage control", *IEEE Transactions on Power Systems*, Vol. 29, No. 1, 2014
- [46] M. Baradar, M. Ghandhari, "A multi-option power flow approach for hybrid AC/DC grids incorporating multi-terminal VSC-HVDC", *IEEE Transactions on Power Systems*, Vol. 28, No. 3, 2013
- [47] S. Wang, Y. Yi, Q. Jiang, X. Chen, Y. Cao, "On-line control of Hopf bifurcation on power systems", *IEEE PES General Meeting*, 2008
- [48] A.P. Lerm, C. Canizares, F. A. B. Lemos, A. S. e Silva, "Multi-parameter bifurcation analysis of power systems", *North American Power Symposium (NAPS)*, 1998
- [49] A.P. Lerm, "Control of Hopf bifurcation in multi-area power systems via a secondary voltage regulation Scheme", *IEEE PES Summer meeting*, 2002
- [50] S. P. Azad, R. Iravani, J. E. Tate, "Dynamic stability enhancement of a DC-segmented AC power system via HVDC operating point adjustment", *IEEE Transactions on Power Delivery*, Vol. 30, No. 2, 2015
- [51] R. Eriksson, "Security analysis of interconnected AC/DC systems", *Australian Universities Power Engineering Conference (AUPEC)*, 2015
- [52] J. Beertern, R. Eriksson, D. Van Hertem, "A new approach to HVDC grid voltage control based on generalized State Feedback", *IEEE PES General Meeting*, 2014

- [53] A. Kumar, S. C. Srivastava, "AC power transfer distribution factors for allocating power transactions in a deregulated market", *IEEE Power Engineering Review*, Vol. 22, 2002
- [54] J.E. Van Ness, J. Boyle, F. Imad, "Sensitivities of large multi-loop control systems", *IEEE Transactions on Automatic Control*, Vol. 10, No. 7, 1965
- [55] T. Smed, "Feasible eigenvalue sensitivity for large power systems", *IEEE Transactions on Power Systems*, Vol. 8, No. 2, 1993
- [56] F. L. Pagola, I. J. Perez-Arriaga, G. C. Verghese, "On sensitivities, residues, and participations", *IEEE Transactions on Power Systems*, Vol. 5, No. 1, 1989
- [57] Z. Huang, N. Zhou, F. Tuffner, Y. Chen, D. Trudnowski, W. Mittelstadt, J. Hauer, J. Dagle, "Improving small signal stability through operating point adjustment", *IEEE PES General Meeting*, 2010
- [58] A. Almutairi, "Enhancement of power system stability using wide area measurement system based damping controller," Ph.D. dissertation, School of Electrical and Electronic Engineering, Univ. of Manchester, Manchester, UK, 2010.
- [59] L. Rouco, F. L. Pagola, "An eigenvalue sensitivity approach to location and controller design of controllable series capacitors for damping power system oscillations", *IEEE Transactions on Power Systems*, Vol. 12, No. 4, 1997
- [60] L. Rouco, F. L. Pagola, G. C. Verghese, I. J. Perez Arriaga, *Selective Modal Analysis: Power System Coherency and Model Reduction*, Vol. 94, Springer, 2013
- [61] R. Preece, J. Milanovic, A. M. Almutairi, O. Marjanovic, "Probabilistic evaluation of damping controller in networks with multiple VSC-HVDC lines", *IEEE Transactions on Power Systems*, Vol. 28, No. 1, 2013
- [62] O. Kotb, M. Ghandhari, R. Eriksson, V. K. Sood, "On small signal stability of an AC/DC power system with a hybrid MTDC network", *Electric Power Systems Research*, Vol. 136, 2016
- [63] H. Latorre, M. Ghandhari, L. Söder, "Control of a VSC-HVDC operating in parallel with AC transmission lines", *IEEE PES Latin America Transmission and Distribution Conference and Exposition*, 2006

- [64] J. Milanovic, S. K. Yee, "Roadmap for tuning power system controllers", Proceedings of 3<sup>rd</sup> IASTED International Conference of Power and Energy Systems, 2003
- [65] J. Arrillaga, *Flexible Power Transmission: The HVDC Options*, Hoboken, NJ: John Wiley & Sons, Wiley, 2007
- [66] Alessandro Astolfi, "Optimization: An Introduction", Imperial College London Online Course, [www.imperial.ac.uk/pls/portallive/docs/1/7288263.pdf](http://www.imperial.ac.uk/pls/portallive/docs/1/7288263.pdf), 2006
- [67] M. Lotfalian, R. Schlueter, D. Idizior, P. Rusche, S. Tedeschi, L. Shu, A. Yazdankhah, "Inertial, governor, and AGC/economic dispatch load flow simulations of loss of generation contingencies", IEEE Transactions on Power Apparatus and Systems, Vol. PAS-104, No. 11, 1986
- [68] G. H. Golub and C. F. V. Loan, *Matrix Computations*, Baltimore; The John Hopkins University Press, 1989
- [69] R. Teixeira Pinto, S. F. Rodrigues, P. Bauer, J. Pierik, "Grid code compliance of VSC-HVDC in offshore multi-terminal DC networks", 39<sup>th</sup> Annual Conference of IEEE Industrial Electronics Society (IECON 2013), 2013
- [70] Z. Huang, N. Zhou, F. Tuffner, Y. Chen, D. Trudnowski, W. Mittelstadt, J. Hauer, J. Dagle, "Improving small signal stability through operating point adjustment", IEEE PES General Meeting, 2010
- [71] W. Pan, Y. Chang, H. Chen, "Hybrid multi-terminal HVDC system for large scale wind power", IEEE Power Systems Conference and Exposition (PSCE), 2006
- [72] T. Haileselassie, "Control, dynamics and operation of multi-terminal VSC-HVDC transmission systems", Ph.D. dissertation, Department of Electric Power Engineering, Faculty of Information Technology, Mathematics and Electrical Engineering, NTNU, Trondheim, Norway, 2012
- [73] C. Guo, C. Zhao, "Supply of an entirely passive AC network through a double-infeed HVDC system", IEEE Transactions on Power Electronics, Vol. 24, No. 11, 2010
- [74] CIGRE Task Force (TF) 38.01.07, Analysis and control of power system oscillations, CIGRE Brochure 111, December 1996

- [75] A. F. Snyder, N. Hadjsaid, D. Georges, L. Mili, G. Phadke, O. Faucon, S. Vitet, "Inter-area oscillation damping with power system stabilizers and synchronized phasor measurements", Proceedings of the International Conference on Power System Technology (PowerCon), 1998
- [76] B. Chaudhuri, B. C. Pal, A. C. Zolotas, I. M. Jaimoukha, T. C. Green, "Mixed-sensitivity approach to  $H_\infty$  control of power system oscillations employing multiple FACTS devices", IEEE Transactions on Power Systems, Vol. 18, No. 3, 2003
- [77] A. G. Phadke, "Synchronized phasor measurements- A historical overview", Proceedings of IEEE/PES Asia Pacific Transmission and Distribution Conference and Exhibition, 2002
- [78] V. Centeno, "Adaptive out-of-step relaying using phasor measurement techniques", IEEE Transactions on Computer Applications in Power, Vol. 6, No. 4, 1993
- [79] J. H. Chow, J. J. Sanchez-Gasca, H. Ren, S. Wang, "Power system damping controller design using multiple input signals", IEEE Control Systems Magazine, 2000
- [80] D. Dotta, A. S. e. Silva, I. C. Decker, "Wide-area measurements-based two-level control design considering signal transmission delay", IEEE Transactions on Power Systems, Vo. 24, No. 1, 2009
- [81] M. E. Aboul-Ela, A. A. Sallam, J. D. McCalley, A. A. Fouad, "Damping controller design for power system oscillations using global signals", IEEE Transactions on Power Systems, Vol. 11, No. 2, 1996
- [82] I. Kamwa, R. Grondin, Y. Hebert, "Wide-area measurement based stabilizing control of large power systems-a decentralized/hierarchical approach", IEEE Transactions on Power Systems, Vol. 16, No. 1, 2001
- [83] Y. Zhang, A. Bose, "Design of wide-area damping controllers for inter-area oscillations", IEEE Transactions on Power Systems, Vol. 23, No. 3, 2008
- [84] B. Dalela, G. Radman, "A study of multivariable supplementary power system stabilizers", Proceedings of 37<sup>th</sup> North American Power Symposium, 2005
- [85] N. Hingorani, L. Gyugyi, *Understanding FACTS: Concepts and Technology of Flexible AC Transmission Systems*, Wiley-IEEE Press, 1999

- [86] D. Van Hertem, O. Gomis-Bellmunt, J. Liang, *HVDC Grids for offshore and supergrid of the future*, Wiley-IEEE Press, 2016
- [87] M. Pavella, P. G. Murthy, *Transient Stability of Power Systems, Theory and Practice*, John Wiley & Sons, 1994
- [88] IEEE Task Force on Load Representation for Dynamic Performance, "Load representation for dynamic performance analysis", *IEEE Transactions on Power Systems*, Vol. 10, 1995

## Curriculum Vitae

Omar Kotb was born in 1986 in Cairo, Egypt. He received his B.Sc in Electrical Power and Machines engineering at Cairo University in 2008. From 2008 to 2009, he worked at ABB as a Design Engineer for Medium Voltage Switchgear. He then started his M.A.Sc in 2009 at the University of Ontario Institute of Technology (UOIT) in Oshawa, ON, Canada, under the supervision of Prof. Vijay Sood. During his master's, he worked on the control and simulation of a hybrid High Voltage Direct Current (HVDC) link supplying a passive network in EMTP-RV software. He obtained his M.A.Sc in 2011. From 2011 to 2012, he worked again at ABB in the position of bidding and pre-sales engineer for High Voltage Substation. From 2012 to 2013, he worked as electrical engineering technology instructor at the American College of the Middle East (ACM) in Egaila, Kuwait.

In 2013, he was selected as a PhD candidate of the Erasmus Mundus Joint Doctorate in Sustainable Energy Technologies and Strategies (SETS) and awarded an Erasmus Mundus Fellowship. This joint PhD program is offered by Comillas Pontifical University, KTH Royal Institute of Technology, and Delft University of Technology.

At KTH, his home university, he started his research on multi-terminal HVDC network controls for stability enhancement under the supervision of Prof. Mehrdad Ghandhari, as principal supervisor, and Dr. Robert Eriksson, as co-supervisor. His research at KTH included the control of a hybrid multi-terminal HVDC network in case of supplying a passive AC grid, as well as in case of interconnecting asynchronous AC grids.

He also visited the Institute for Research in Technology (IIT) at Comillas Pontifical University during his PhD (January 2016-September 2016), where he worked on sensitivity-based placement of damping controllers with Prof. Luis Rouco.

His research interests include multi-terminal HVDC systems, FACTS, power system stability and control, and large-scale integration of renewable energy sources.

## List of publications

### **Papers published in journals with Journal Citation Report (JCR):**

- [J1] O. Kotb, M. Ghandhari, R. Eriksson, V. K. Sood, "On small signal stability of an AC/DC power system with a hybrid MTDC network", *Electric Power Systems Research*, Vol. 136, pp. 79-88, July 2016.
- [J2] O. Kotb, M. Ghandhari, R. Eriksson, R. Leelaruji, V. K. Sood, "Stability enhancement of an interconnected AC/DC power system through VSC-MTDC operating point adjustment", *Electric Power Systems Research*, Vol. 151, pp 308-318, October 2017.

### **Peer-reviewed Conference Papers:**

- [C1] O. Kotb, M. Ghandhari, R. Eriksson, V. K. Sood, "A study on the control of a hybrid MTDC supplying a passive load", IEEE International Conference on Power System Technology (POWERCON 2014), Chengdu, China, October 2014.
- [C2] O. Kotb, M. Ghandhari, J. Renedo, L. Rouco, R. Eriksson, "On the design and placement of a supplementary damping controller in an embedded VSC-MTDC network", IEEE International Conference on Innovative Smart Grid Technologies (ISGT Europe 2017), Torino, Italy, September 2017.

For KTH Royal Institute of Technology:  
DOCTORAL THESIS IN ELECTRICAL ENGINEERING  
TRITA-E ECS-AVL-2018:25  
[www.kth.se](http://www.kth.se)

ISBN 978-91-7729-726-0